Three-Dimensional Radiation-Hydrodynamic Simulation of Clumpy Outflow and Its Application to Supercritical Accretors around Black Holes

Hiroshi Kobayashi

Acknowledgments

I would like to show my greatest appreciation to my advisor, Dr. K. Ohsuga. He provided me this precious study opportunity as a Ph.D student If not for his guidance and persistent help, this thesis would have been impossible. I additionally owe my deepest gratitude to a collaborator, Dr. S. Mineshige. Intense and diverse discussion with him have considerably helped me in writing this thesis. I would like to express my gratitude to Dr. H. R. Takahashi who provided plenty of advice regarding code development, Dr. N. Kawashima who discussed about comparison with observation, Dr. Y. Asahina who discussed about analysis, and Dr. S. Takeuchi who provided his suggestions throughout the study. I want to thank Dr. K. Tomasaka and Dr. M. Tanaka for their useful comments and discussions as an academic advisor. I also thank Dr. N. Kashikawa, Dr. K. Hada, Dr. S. Kameno, Dr. T. Takiwaki, and Dr. R. Matsumoto who accepted the study and provided meaningful comments.

Abstract

In this thesis, clumpy outflows that originate from the supercritical accretion flow around a stellar mass black hole are studied using global three-dimensional (3-D) radiation-hydrodynamic (RHD) simulations. For the first time, the complete set of radiation hydrodynamics equations in 3-D geometry is solved. The radiation fields of the black hole are evaluated by adopting the M1-closure method to guarantee the conservation of total energy and momentum of the radiation and fluid. To reduce the computational time, only the outflow part is solved based on the assumed presence of an underlying quasi-steady disk with a mass accretion rate onto the black hole of $10^2 L_{\rm Edd}/c^2$, where $L_{\rm Edd}$ is the Eddington luminosity and c is the speed of light. Numerical calculation is initiated for axisymmetric 2-D simulation data with small perturbations in the azimuthal direction, and initial values at the bottom and inner boundaries of the computational domain were retained as future physical quantities. Within a few seconds of the simulation time, the radiatively driven outflow, which has an outflow rate of $\sim 10 L_{\rm Edd}/c^2$, fragments into several clumps above the photosphere, which is located at a few hundreds Schwarzschild radii ($r_{\rm S}$) from the central black hole. These clumps depict the shape of a torn sheet and rotate around the central black hole at a sub-Keplerian velocity. The typical clump size is 30 $r_{\rm S}$ or less in the radial direction; however, it is more elongated in the angular direction to a maximum of approximately hundreds of $r_{\rm S}$. The passage of such clumps across the line of sight of a distant observer would cause stochastic luminosity variations with variation timescales of several seconds for a stellar-mass black hole that depicts a mass range of ten to several tens of solar masses. This effect is in approximate agreement with the observational results that were obtained for several ultraluminous X-ray sources (ULXs). Our results, therefore provide strong support for the hypothesis that these ULXs are powered by supercritical accretion onto a stellar mass black hole. Additionally, we suggest that our clumpy outflow model many explain some observational

features of the ultra-fast outflows and the origin of broad line-emitting clouds in the active galactic nuclei.

Contents

Acknowledgments **iii**

Abstract **iv**

1 Introduction **1**

1.1 Accretion Flow onto Black Holes 1

1.1.1 Distinct Accretion Modes 1

1.1.2 Standard Disk Model 1

1.1.3 RIAF 5

1.1.4 Slim Disk 6

1.1.5 Simulation 8

1.2 Clumpy Outflow Model 13

1.2.1 Clumpy Outflow Simulated by T13 13

1.2.2 Super-Eddington Atmosphere Simulated by T14 17

1.2.3 Other Features 17

1.3 The Purpose of This Thesis 20

2 Our Model, Basic Equations, and Methods of Calculation **22**

2.1 Our Model 22

2.2 Basic Equations 23

2.2.1 Initial Setting 24

2.2.2 Boundary Conditions 26

2.2.3 Numerical Method 28

3 Properties of Clumpy Outflow **29**

3.1 Overall Structure 29

3.2 Auto-Correlation Analysis 35

3.3 Influence of Perturbation 38
3.4 Formation Mechanism of Clumpy Structure 39

4 Observational Implications **49**
4.1 Comparison with Observations of ULXs 49
4.1.1 Overview of ULXs 49
4.1.2 Time Variation 52
4.2 Comparison with Observations of Other Objects 55
4.2.1 Narrow-Line Seyfert 1 Galaxies 57
4.2.2 Black Hole X-Ray Binaries 59

5 Summary **66**

A Setting of Computational Domain **69**

B Resolution Dependence **72**

Chapter 1 Introduction

1.1 Accretion Flow onto Black Holes

Black hole accretion systems, which comprise black holes with a variety of masses and surrounding rotating gaseous disks, are one of the most powerful energy sources in the universe. Accordingly, many luminous compact objects, including X-ray binaries, active galactic nuclei (AGNs), gamma-ray bursts, etc., are believed to be powered by black hole accretion.

1.1.1 Distinct Accretion Modes

The observational history of black hole candidates is closely linked to the development of high-energy astrophysics notably X-ray and gamma-ray astronomy as high-energy emissions are the main product of black hole objects. As observational study has progressed, however, the multi-wavelength nature of radiation from black hole objects, in which multiple emission processes (components and or states) are involved with the observational appearance of such objects, has become widely recognized. We should also point out that the presence of several distinct spectral states has been recognized through X-ray observations starting in the early 1970's. From a theoretical point of view, accretion flow can be divided into three modes standard accretion disks, radiatively inefficient accretion flow (RIAF), and slim (or supercritical) disks according to the mass accretion rate onto the black hole, $\dot{M}_{\rm acc}$, or more precisely, the normalized accretion rate, $\dot{m}_{\rm acc} \equiv \dot{M}_{\rm acc}c^2/L_{\rm Edd}$ where c and $L_{\rm Edd}$ are the speed of light and Eddington luminosity, respectively (see Figure 1). The later mode is our primary concern here, but we first present an overview of all three distinct accretion modes.

1.1.2 Standard Disk Model

The standard accretion disk model was suggested by Shakura & Sunyaev [1973] (see also Novikov & Thorne [1973] for the relativistic version). In this model, the flow is assumed to be steady and axisymmetric, with the mass accretion rate remaining constant in the radial direction and hydrostatic equilibrium holding in the vertical

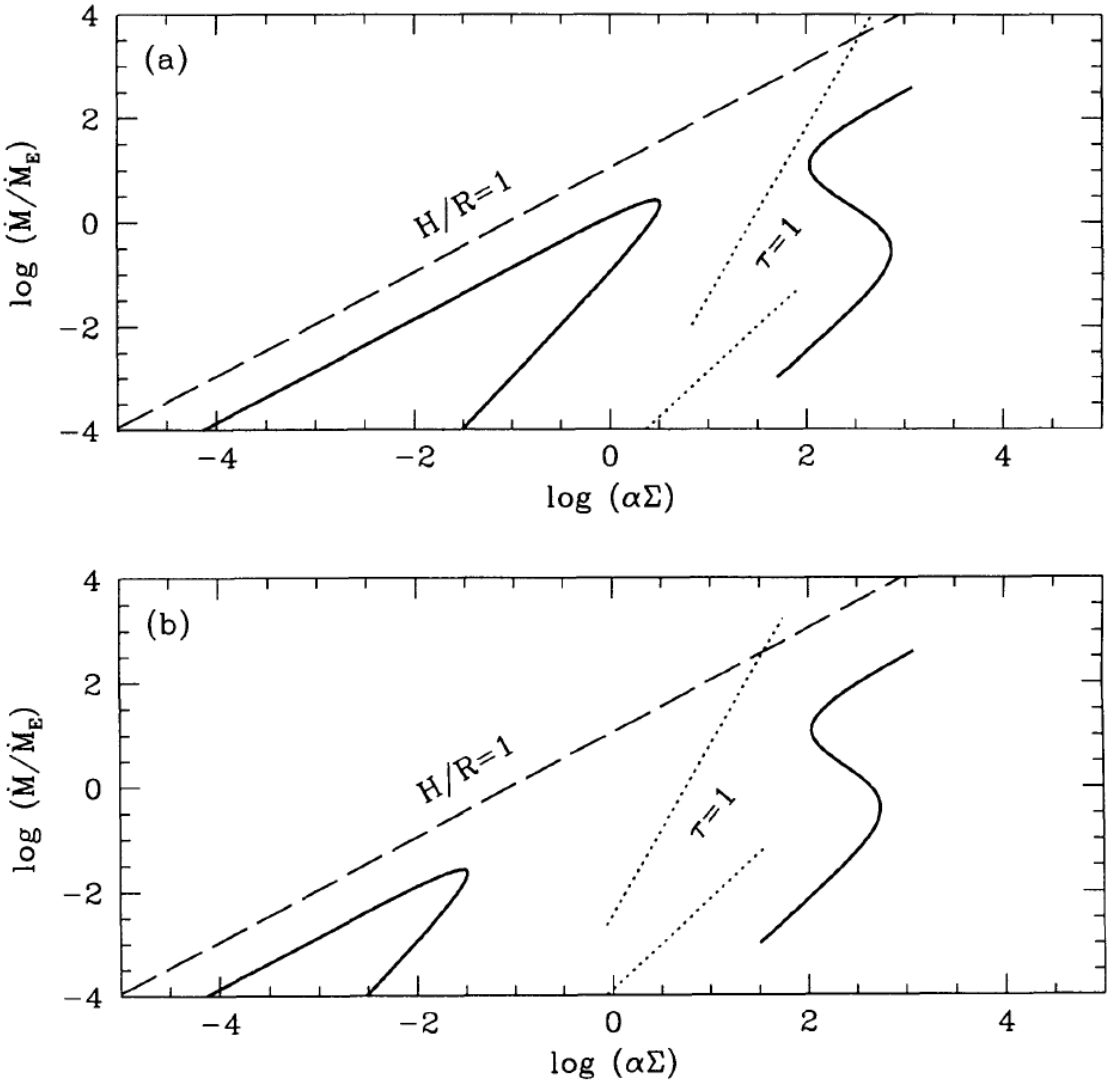

Figure 1: Thermal equilibrium curves of optically thick (solid S-shaped line to the right) and optically thin (solid line to the left) accretion disks for the viscosity parameters of $\alpha = 0.1$ (a) and 0.01 (b), respectively. The upper and lower stable branches of the optically thick S-shaped curve correspond to the slim and standard disk, respectively. The upper branch of the thin regime corresponds to the RIAF. Other branches indicate unstable disks. Locations corresponding to the aspect ratio $H/R = 1$ optical depth of $\tau = 1$ are also indicated in each panel(Abramowicz et al. [1995]).

direction. It is also assumed that the centrifugal force balances with the gravity and the viscous heating rate ($Q_{\rm vis}$) equals the radiative cooling rate ($Q_{\rm rad}$),

$$Q_{\rm vis} = Q_{\rm rad}. \tag{1}$$

The structure of the disk is then obtained by solving the vertically integrated hydrodynamic equations.

Under this model, the standard disk becomes geometrically thin and optically thick. Although the centrifugal force balances gravity, the gas in the disk slowly accretes toward the black hole via the transport of angular momentum by disk viscosity and, ultimately, the disk matter is swallowed by the black hole.

The gas in the disk is heated by the dissipation of energy, which causes it to emit photons. This means that the origin of the radiation from the disk is the gravitational energy of the accreting matter. About half of the gravitational energy of the matter is converted to rotational kinetic energy, while the other half is converted to radiation energy and released from the disk surface.

One of the most important processes in a black hole accretion system is the disk viscosity, which induces both angular momentum transport and disk heating. Although at the time of the formulation of the standard model in 1973 the basic physics of disk viscosity was not understood, the viscosity is now understood to be of magnetic origin, and the viscous stress tensor is assumed to be in proportional to the gas pressure when the standard disk is established. Using this phenomenological treatment of disk viscosity, the disk structure can be successfully described under the standard disk model. This simple model of disk viscosity is called the α-viscosity model. The disk structure of the standard disk model is determined by setting the black hole mass ($M_{\rm BH}$), the mass accretion rate, and the α-parameter. In the standard model, Equation (1) holds, resulting in the largest energy conversion efficiency ($L_{\rm d}/\dot{M}_{\rm acc}c^2$, where $L_{\rm d}$ is the disk luminosity and c is the speed of light) among the three accretion models. In case in which the central object is a black hole, the energy conversion efficiency is about $10 - 40$ %.

Here, we note that the standard disk model assumes either that outflows are not launched from the disk or that the reduction in the mass accretion rate via the ejection of matter is negligibly small, as the mass accretion rate does not depend on the distance from the black hole. However, this assumption does not always hold

because outflows are sometimes observed from disks in the form of jets or disk winds. Thus, multi-dimensional approaches are necessary to model more realistic structures.

From Equation (1), the radiative flux of the standard disk is given as,

$$F_{\rm SD} = \frac{3GM_{\rm BH}\dot{M}_{\rm acc}}{8\pi r^3}\left(1-\sqrt{\frac{r_{\rm in}}{r}}\right), \tag{2}$$

where G is the gravitational constant, r is the distance from the origin (center of the black hole), and $r_{\rm in}$ is the innermost radius of the disk. From this equation it is seen that, under the standard disk model, radiation is primarily emitted from the innermost part of the disk because $F_{\rm SD} \propto r^{-3}$. Integrating Equation (2) confirms that half of the gravitational energy is released as radiation:

$$\begin{aligned} L_{\rm d} &= \int_{r_{\rm in}}^{\infty} 2F_{\rm SD}2\pi r dr \\ &= \frac{GM_{\rm BH}\dot{M}_{\rm acc}}{2r_{\rm in}}. \end{aligned} \tag{3}$$

Because the standard disk is optically thick, the disk emission is considered to be blackbody radiation, $F_{\rm SD} = \sigma T_{\rm eff}^4$, where σ is the Stefan-Boltzmann constant and $T_{\rm eff}$ is the effective temperature. From this, the temperature profile of the standard disk is given by

$$T_{\rm eff}(r) = \left[\frac{3GM_{\rm BH}\dot{M}_{\rm acc}}{8\pi\sigma r^3}\left(1-\sqrt{\frac{r_{\rm in}}{r}}\right)\right]^{1/4}. \tag{4}$$

That is, the spectrum of the standard disk becomes that of a multi-color disk blackbody representing the superposition of blackbody radiation at various temperatures. As the region around the innermost part of the disk is the most luminous and hottest, the peak of the spectrum is determined by the temperature at $r \sim r_{\rm in}$.

It is also seen from Equation (4) that the effective temperature decreases as the black hole mass increases. For instance, in the case where $M_{\rm acc} \sim L_{\rm Edd}/c^2$ we find $T_{\rm eff}$ near the innermost part is $\sim 10^5$ K for a supermassive black hole of $\sim 10^{8-9}$ $M_\odot$ (where $M_\odot$ is the solar mass) and $\sim 10^7$ K for a $\sim 10-100M_\odot$ stellar mass black hole. Therefore, the standard disk around a supermassive black hole primarily emits UV photons, while strong X-rays are produced by stellar mass black holes. This tend is consistent with observations of quasars exhibiting strong UV radiation and X-ray binaries with thermal emissions in the X-ray band. Note that non-thermal components that probably originate from Comptonization, are also observed; the

standard disk model cannot explain these components, and an additional component (e.g., a disk corona) is required to fit the observed spectra.

The standard disk model is widely applied as it closely reproduces the thermal emissions of quasars and X-ray binaries. However, the model breaks down if the mass accretion rate is either much smaller or much larger than the critical rate, $L_{\rm Edd}/c^2$. Indeed, the spectra of low-luminosity AGNs and the low-hard states of X-ray binaries, for which the accretion rates are thought to be $\ll L_{\rm Edd}/c^2$, cannot be explained by the standard disk model. In the case of $\dot{M}_{\rm acc} \ll L_{\rm Edd}/c^2$ (or $> L_{\rm Edd}/c^2$), the RIAF (slim disk model) can be used to supplant the standard disk model.

1.1.3 RIAF

The solution of the RIAF model is obtained under the assumptions that the flow is steady and axisymmetric and that the mass accretion rate is constant in the radial direction. RIAF also employs the α-viscosity. Unlike the standard disk model, the effect of radial motion is not neglected. RIAF is geometrically thick and optically thin and has a rotational velocity smaller than the Keplerian velocity and a radial velocity proportional to the free-fall velocity. Whereas under the standard model matter in the disk follows a circular orbit, under RIAF the gas falls onto the black hole following a swirling trajectory with in a relatively short time.

One of the most significant differences between the RIAF and standard disk models is the flow of energy. Although the viscous heating rate balances the radiative cooling rate in a standard disk, under RIAF, the advective cooling rate ($Q_{\rm adv}$) dominates the radiative cooling and nearly equals the viscous heating rate,

$$Q_{\rm vis} \sim Q_{\rm adv} \gg Q_{\rm rad}. \tag{5}$$

Because the density under RIAF is too low to emit photons effectively, the energy dissipated by the viscosity is not converted into radiation energy. Instead, the gas is swallowed by the black hole without releasing thermal energy, leading to a very small, $L_{\rm d}/\dot{M}_{\rm acc}c^2$. As both the accretion rate and energy conversion efficiency are small, RIAF produces a very dark flow. Thus, the model is optically thin and does not emit blackbody radiation.

As mentioned above, the energy loss via radiation is very small, making RIAF hotter than the standard disk model. Therefore, despite its low luminosity an RIAF

disk tends to emit hard X-ray photons. In addition, whereas the disk luminosity of the standard disk is proportional to $\dot{M}_{\rm acc}$, that of the RIAF disk is proportional to $\dot{M}_{\rm acc}^2$. These RIAF features can be deduced from a self-similar solution in Narayan & Yi [1994]. A more realistic solution that passes through the transonic point is numerically obtained by setting suitable boundary conditions.

One of the more prominent RIAF candidates is Sgr A*. Narayan et al. [1995] demonstrated that the spectrum of Sgr A* can be well explained by the RIAF model(see also Manmoto et al. [1997]). In their paper, the flow was treated as a two-temperature plasma via separation of the ion and electron temperatures via weak Coulomb interaction. The radio emission of Sgr A* is produced by self-absorbed synchrotron emission, with Compton upscattering and free-free emission playing important roles in the IR and X-ray bands (see Figure 2). RIAF disks are thought to be present in objects whose spectra are similar to that of Sgr A*, e.g., low-luminosity AGNs and low-hard state of X-ray binaries.

1.1.4 Slim Disk

A slim disk occurs when $\dot{M}_{\rm acc} > L_{\rm Edd}/c^2$. As mentioned in the previous subsection, an RIAF can be identified as the optically thin regime of an advection-dominated accretion flow, while optically thick and advection-dominated accretion flow described by the slim disk model (Abramowicz et al. [1988]) for which, Equation (5) holds. Under this model, the advective cooling is also larger than the radiative cooling, but for reasons that differ from those under the RIAF model. In a slim disk, a very large number of photons are generated because of the disk's high density (high emissivity). However, the disk is extremely optically thick, which prevents a large fraction of the photons from escaping from the disk surface. As the radiative diffusion time is longer than the accretion time, the photons are swallowed, along with the matter, by the black hole with the matter; thus, most of the dissipated energy is eventually swallowed as radiation energy by the black hole.

Because $Q_{\rm vis} \sim Q_{\rm adv} \gg Q_{\rm rad}$, the slim disk energy conversion efficiency is very small. However, the slim disk luminosity is the highest among the three accretion modes; based on the model solution, the disk luminosity exceeds the Eddington luminosity. As the radiation energy is enhanced in the disk, the radiation pressure dominates the gas pressure, and the slim disk becomes geometrically thick owing to

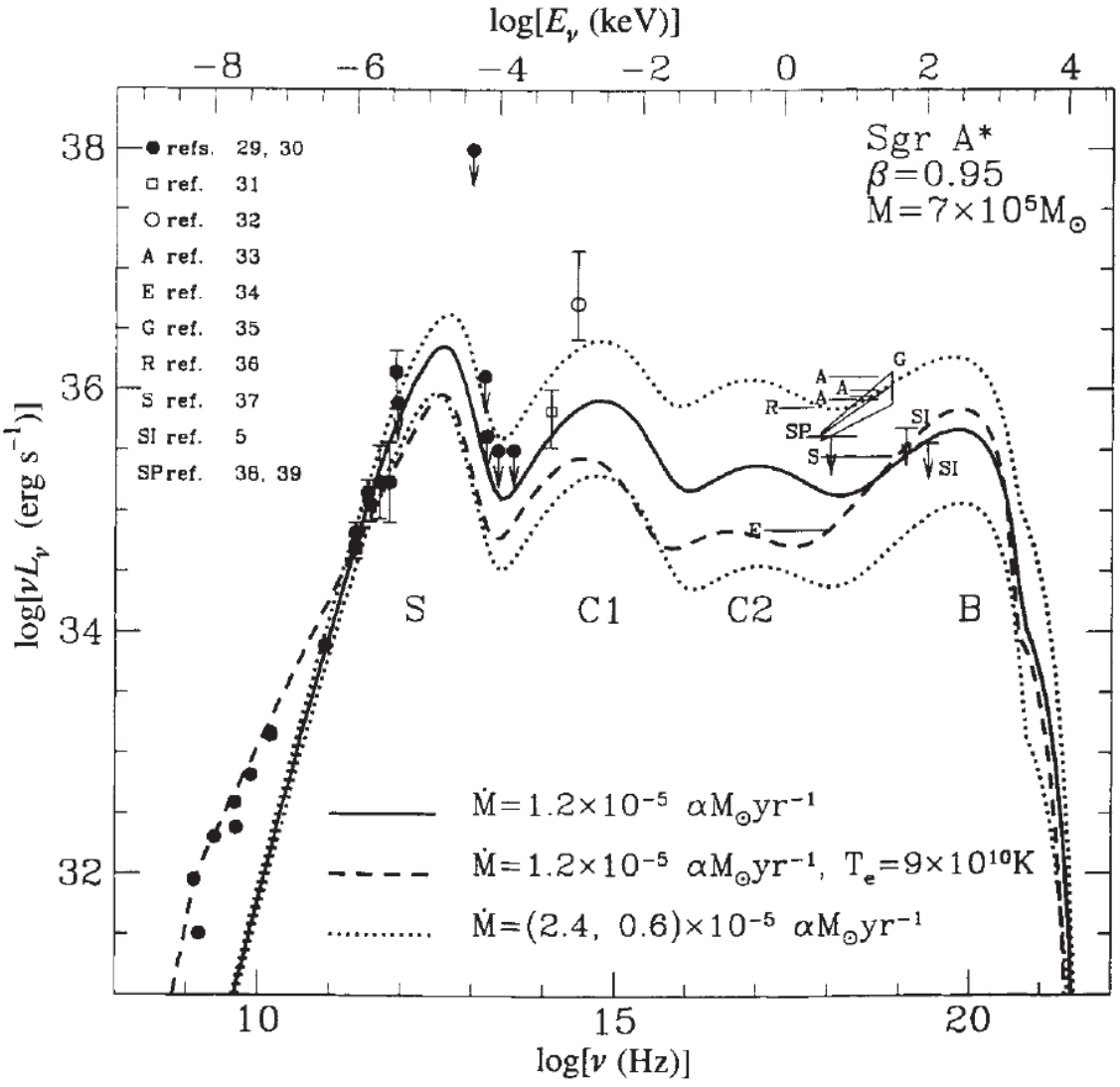

Figure 2: The spectrum of the RIAF of a black hole assumed to be 7×10^5 $M_\odot$ (Narayan et al. [1995]). The solid, upper-dotted, and lower-dotted curves show the spectra for mass accretion rate of $1.2 \times 10^{-5} \alpha M_\odot \mathrm{yr}^{-1}$, $0.6 \times 10^{-5} \alpha$ $M_\odot \mathrm{yr}^{-1}$, and $2.4 \times 10^{-5} \alpha$ $M_\odot \mathrm{yr}^{-1}$, respectively. The dashed line represents an isothermal model in which the electrons are assumed to have a constant temperature of 9×10^9 K outside of 3,000 r_S. The symbols and horizontal lines indicate various measurements of the spectrum of Sgr A*. Arrows indicate upper limits, and the sloping 'box' gives the range of fluxes and spectral slopes according to Pavlinsky et al. [1992]. Here, the measured fluxes are converted to luminosities assuming a distance of 8.5 kpc to the Galactic Center. This figure shows that the RIAF model can explain the observations of the Sgr A$*$.

the strong radiation pressure. The slim disk emission is expected to be that of a multi-color disk blackbody. However, as the effective temperature depends on the distance as

$$T_{\rm eff} \propto r^{-1/2}, \tag{6}$$

the emergent spectrum differs from that of the standard disk.

Slim disks potentially exist in ultraluminous X-ray sources (ULXs). ULXs are very luminous compact objects with X-ray luminosities exceeding the Eddington luminosity of a stellar mass black hole (a detailed explanation of ULXs is given in section 4.1.1). Watarai et al. [2001] concluded that the spectra of ULXs can be explained using the slim disk model. This is demonstrated in Figure 3, in which the $L_{\rm X}$-$T_{\rm in}$ diagram (where $L_{\rm X}$ is the X-ray luminosity and $T_{\rm in}$ is the temperature at the innermost radius) shows the slim disk solution deviating from the track of the standard disk model. They found that the ULX IC 342 S1 follows the slim disk branch, i.e., that a slim disk has formed in IC 342 S1. The slim disk model can also be applied to narrow-line Seyfert galaxy 1s (NLS1s). As the black hole mass in some NLS1s is thought to be relatively small, their Eddington ratios, $L_{\rm d}/L_{\rm Edd}$, might be large compared to those in other AGNs. In addition, the temperatures of the thermal components in their spectra are reported to be higher than in other AGNs, a feature that is also consistent with the slim disk model. Slim disks might also have appeared in the early universe. Supermassive black holes have been detected in the high-z universe at $z > 7$ (Mortlock et al. [2011]; Bañados et al. [2017]). Because the timescale in which black holes grow via the accretion is comparable to or slightly longer than the cosmic age, it is difficult to explain the existence of these supermassive black holes via sub-critical accretion, and supercritical accretion (slim disks) is a possible solution.

1.1.5 Simulation

The classical models introduced in subsection 1.1 have contributed significantly to the understanding of black hole accretion flow. However, some problems have been noted. For example, because the models are established by assuming steady-state flow, time variation cannot be resolved. Furthermore, the models are essentially one-dimensional models, i.e., their structures are obtained by solving one-dimensional equations in the radial direction, and therefore multi-dimensional effects are cannot be treated. Thus, the turbulent motion believed to occur within the accretion disk

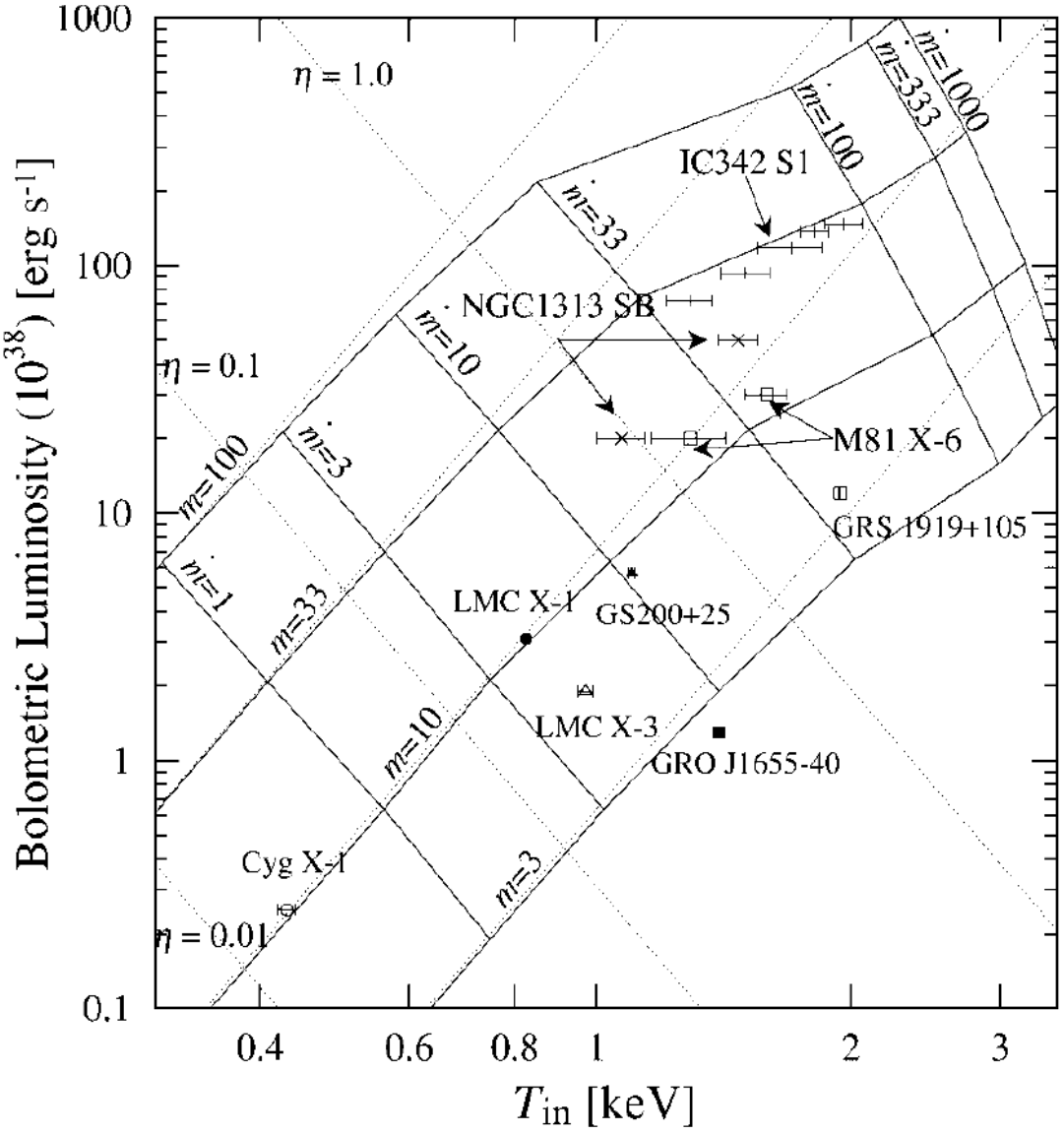

Figure 3: X-ray $L_{\rm X}$-$T_{\rm in}$ diagram of black hole objects, where $L_{\rm X}$ is the X-ray luminosity and $T_{\rm in}$ is the innermost disk temperature (Watarai et al. [2001]). Solid and dotted meshes indicate the results of the slim and standard disk models, where m is the black hole mass normalized by the solar mass and $\dot{m}$ is the accretion rate normalized by the critical rate, $L_{\rm Edd}/c^2$. The inclination angle is assumed to be $i = 0$ (face–on). Symbols indicate *ASCA* data of ULXs and black hole binaries taken from Mizuno et al. [2001], and Makishima et al. [2000]. A ULX IC 342 S1 is clearly seen to move along the slim disk branch of $33M_\odot$.

cannot be treated. In addition, the mass accretion rate is assumed to be constant in the radial direction, which implies either that the gas does not blow away from the disk or that the mass pulled out of the disk via gas ejection, is negligibly small. However, it has been suggested that powerful outflow is generated by radiation and magnetic pressure and the magnetic centrifugal force. To resolve these problems, multi-dimensional, time-dependent simulations are necessary.

The importance of multi-dimensional magnetohydrodynamic (MHD) simulation was recognized in the 1990s. Balbus & Hawley [1991] showed that the disk viscosity, which induces the transport of angular momentum and dissipation of the energy within the disk, is of magnetic origin. A global three-dimensional MHD simulation was performed for the first time by Matsumoto [1999]. In the 2000s, the structure and dynamics of accretion disks were examined in detail via MHD simulations (Matsumoto 1999; Machida et al. 2000; Hawley & Krolik 2001; Koide et al. 2001; De Villiers et al. 2003; Hawley & Krolik 2006; Fragile & Meier 2009).

Although radiative cooling and radiation pressure were not taken into consideration in these MHD simulations, they were still useful for investigating less luminous accretion flows such as RIAF. By contrast, when the luminosity is not negligibly small, radiative cooling and radiation pressure influence the dynamics of the accretion flow, necessitating the use of radiation hydrodynamics (RHD) simulations, which solve flow dynamics, radiative transport, and gas-radiation interaction, in the investigation of the luminous flows found in standard-type and/or slim-type disks. Multidimensional RHD simulations of accretion disks were performed by Eggum [1987], Kley [1989], Okuda et al. [1997], Fujita & Okuda [1998], Kley & Lin [1999], and Okuda & Fujita [2000].

RHD simulations of supercritical accretion were pioneered by Eggum [1998], in which it was assumed that the gas and radiation were in thermal equilibrium everywhere. Although this unrealistic assumption was relaxed in the simulations by Okuda [2002], the steady structure of the supercritical flows was not clarified. Ohsuga et al. [2005] revealed for the first time the quasi-steady structure of supercritical accretion flow and outflow using long-time RHD simulations. According to their results, the mass accretion rate significantly exceeds the critical value, and the disk luminosity becomes equal to or greater than Eddington luminosity. Although a large amount of radiation energy is generated within the disk, some fraction of it is swallowed by the

black hole with the accreting gas. However, most of the radiation moves in the vertical direction and escapes through the less dense region around the rotation axis, and therefore the outward radiation force becomes zero around the equatorial plane and cannot prevent the accretion flow deep inside the disk (Ohsuga & Mineshige [2007]). By contrast, the upward radiation force exceeds that of gravity, leading to powerful outflows.

The structures of these supercritical accretion flow and outflows were confirmed by radiation magnetohydrodynamics simulations (RMHD), which solve the hydrodynamics, radiation fields, and magnetic field self-consistently (Ohsuga et al. 2009). As shown in the left panels of Figure 4, powerful outflows are launched from a geometrically thick disk in which the luminosity is a few times higher than the Eddington luminosity. The outflows are accelerated by the radiation force and the disks are supported by the radiation pressure. In contrast to RHD simulations, in which the α model is employed, the disk viscosity in RMHD simulations is induced by solving the magnetic fields. Based on this, RMHD simulation is considered to be the research method that can most realistically investigate accretion flows and outflows. RMHD simulation using a shearing-box approximation was performed by Turner et al. [2003] and Hirose et al. [2006]. These simulations were carried out to investigate the local disk structure and therefore did not examine entire disks or outflows. To investigate the structures of inflows and the outflows, global simulations such as that conducted by Ohsuga et al. [2009] are necessary.

In addition to supercritical accretion, Ohsuga et al. [2009] successfully reproduced standard-type and RIAF-type flow, as shown in the middle and right panels in Figure 4, in which it is seen that outflows are generated even in standard-type and RIAF-type disks. In these cases, matter is blown away by the magnetic pressure-force. Although the standard disk, RIAF, and slim disk models are useful in understanding the basic features of accretion flows, we again stress that multi-dimensional simulations are necessary to reveal realistic inflow-outflow structure.

RMHD simulation of supercritical accretion has also recently been adapted to general relativity (Sadowski et al. [2014]; Mckinney et al. [2014]; Fragile et al. [2014]; Jiang et al. [2014]; Takahashi et al. [2016]). Such simulations have also produced a quasi-steady supercritical accretion disk formations and outflows accelerated by radiative pressure in the manner of Ohsuga et al. [2009].

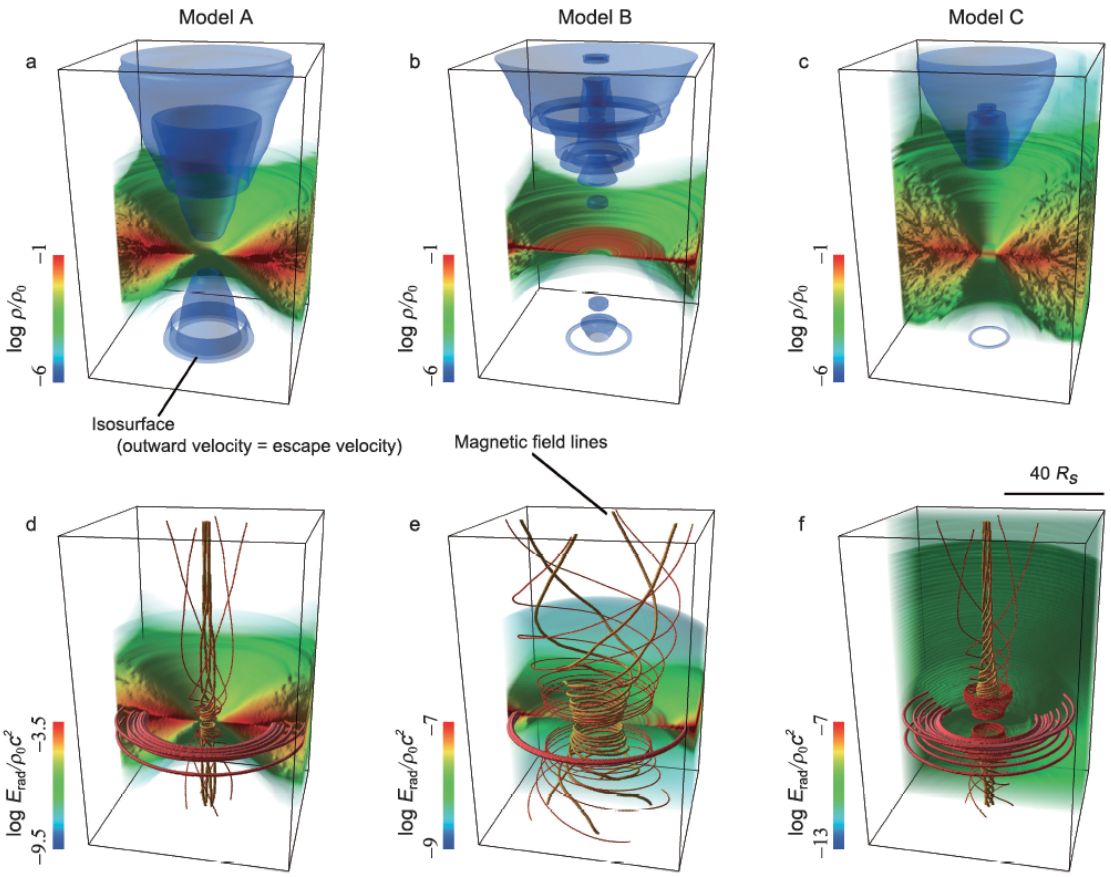

Figure 4: Perspective views of inflow and outflow around a black hole obtained using 2-D RMHD simulations (Ohsuga et al. [2009]). Upper panels: Normalized density distributions (color) and shape of the outflow (blue surface). Lower panels: Normalized radiation energy density (color) and magnetic field lines (lines). Left, middle, and right panels correspond to the 2-D version of the slim disk, standard disk, and the RIAF, respectively. In the left panels, the outflow is launched by a strong radiation force, as the disk luminosity exceeds the Eddington luminosity. By contrast, the outflows in the middle and right panels are generated by magnetic pressure.

1.2 Clumpy Outflow Model

One of the more prominent features of supercritical accretion is the emergence of powerful outflow driven by the force of radiation-pressure (see, e.g., Shakura & Snuyaev [1973]; Takeuchi et al. [2009]). Some simulation studies of outflow were carried out in the 2000s but were restricted to relatively small simulation boxes primarily because of the limitations imposed by computer performance at the time. Takeuchi et al. [2013] (hereafter referred to as T13) were the first to simulate an extended outflow structure from supercritical flow using large box RMHD simulation. They found that the outflow has a clumpy substructure and, hereafter, such outflow with inhomogeneous structure is referred to as a clumpy outflow. In this section, we summarized the 2-D nature of the clumpy outflow simulated by T13 and its physical formation mechanisms as proposed by Takeuchi et al. [2014] (hereafter referred to as T14) based on their super-Eddington atmosphere simulation.

1.2.1 Clumpy Outflow Simulated by T13

As mentioned above, T13 initially performed RMHD simulations of supercritical inflow and outflow by significantly expanding a simulation box while maintaining a high spatial resolutions within a computational domain of 514 $r_{\rm S} \times 514$ $r_{\rm S}$, where $r_{\rm S} = 2GM_{\rm BH}/c^2$ is the Schwarzschild radius. They used the cylindrical coordinates (R, θ, z), where R is the radial distance from the rotational (z-) axis, θ is the azimuthal angle, and z is the vertical coordinate. In their results, clumpy outflow emerged above a photosphere located far from the central black hole (note that the precise location of the photosphere can depend on the accretion rate). Significantly, as the clumpy structure never appeared below the photosphere, the previous RHD (or RMHD) simulations with limited simulation boxes all missed the clumpy outflow structure. T13 simulated accretion flow and associated outflow around a 10 $M_\odot$ black hole, starting from an initially magnetized torus at around 40 $r_{\rm S}$ with no mass input assumed. As a result of the magnetic processes, which generate as disk viscosity, inflow occurred from the initial torus. After a computational time exceeding about ~ 5 s, the accretion flow settled down into a quasi-steady state. The mass accretion rate was $\dot{M}_{\rm acc} \sim 100 L_{\rm Edd}/c^2$, the mass outflow rate was $\dot{M}_{\rm out} \sim 10 L_{\rm Edd}/c^2$, and the photon luminosity was $\sim L_{\rm Edd}$. In other words, the mass accretion rate significantly exceeded the critical accretion rate, resulting in a supercritical simulated accretion

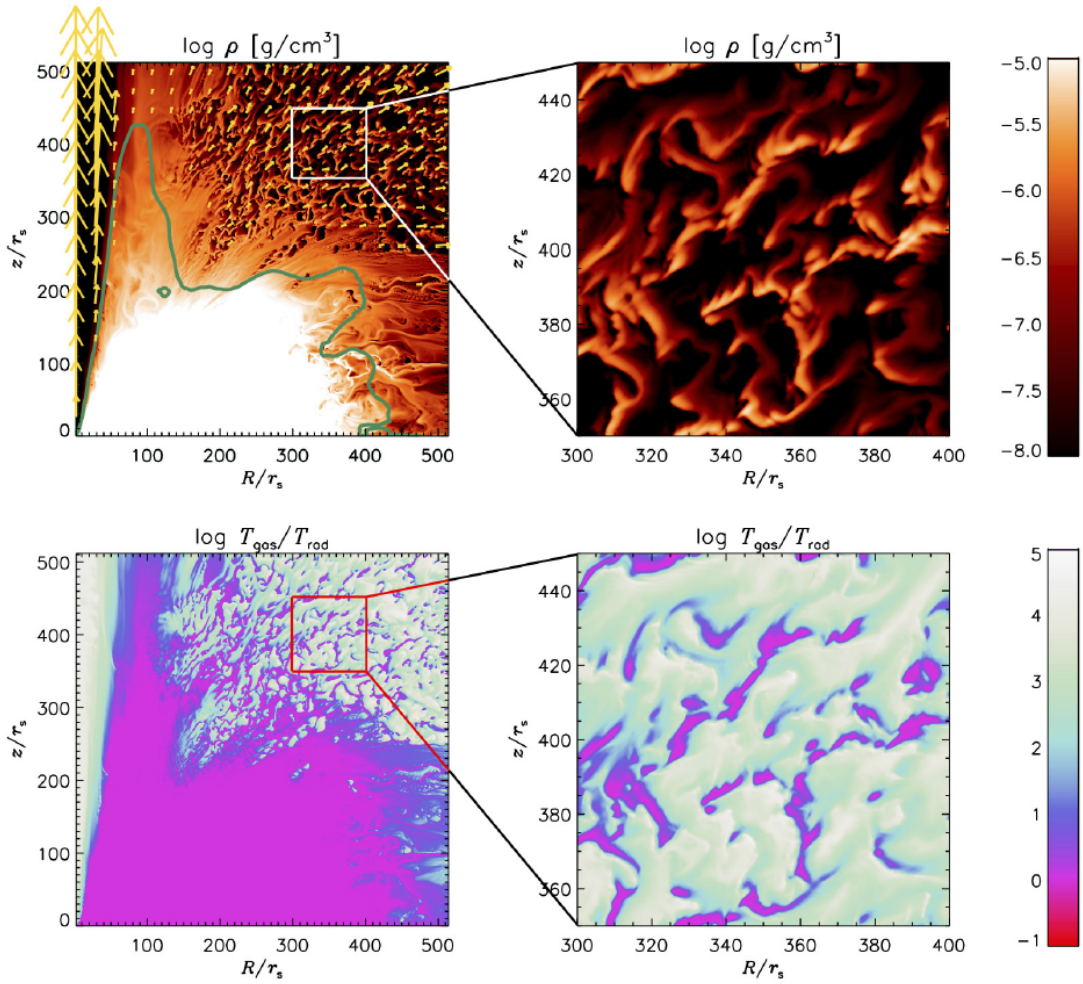

Figure 5: Two-dimensional structure of a supercritical accretion flow and outflow around a $M_{\rm BH} = 10\ M_\odot$ black hole simulated by T13. Matter density color overlaid with the flow velocity vector (upper panels) and the ratio of the gas temperature to the radiation temperature (color) are shown. Arrows representing the velocity vectors (upper-left panel) are displayed only in the region where their values exceed the escape velocity. Green lines in the upper-left panel indicate the surface at which the upward radiation force equals to the downward gravitational force of the central black hole. The left two panels show the structure over the entire computational domain, while the right two panels provide magnified views of the left panels at $300\ r_{\rm S} \leq R \leq 400\ r_{\rm S}$ and $350\ r_{\rm S} \leq z \leq 450\ r_{\rm S}$, respectively. The elapsed time is 9 s, which is equivalent to 30 times the Keplerian time scale at $R = 40\ r_{\rm S}$.

flow.

Figure 5 shows the two-dimensional distributions of the matter density (upper panels) and the ratio of gas temperature to radiation temperature (lower panels) in the supercritical accretion flow and outflow around a $M_{\rm BH} = 10\ M_\odot$ black hole simulated by T13. Here, the radiation temperature is defined as $T_{\rm rad} = (cE_0/4\sigma)^{1/4}$, where E_0 is the comoving frame radiation energy density. The elapsed time is 9 s, corresponding to $\sim 30\ t_{\rm K}$ ($t_{\rm K} \equiv 2\pi/\Omega_{\rm K}$, where $\Omega_{\rm K} \equiv \sqrt{GM/r^3}$ is the Keplerian rotational angular velocity) at a distance of $R = 40\ r_{\rm S}$. In the upper-left panel, the yellow arrow shows a velocity field in which the speed exceeds the escape velocity ($v_{\rm esc} = (2GM_{\rm BH}/r)^{1/2}$), while the green line shows the surface at which $\chi F_0/c = \rho_0 \|\nabla\psi_{\rm PN}\|$. Here, χ is the total opacity per unit volume, F_0 is the radiative flux, ρ_0 is the matter density, and $\psi_{\rm PN}$ is the pseudo-Newtonian potential.

It is clear from the figure that the outflow has a clumpy structure. The typical gas clump density is $\sim 10^{-6}$ g cm^{-3}, while the outflow speed is $\sim 10\%$ of the speed of light, and the outflow direction is $10^\circ - 50^\circ$ from the rotational (z-) axis (upper panel). It has been confirmed that radiative equilibrium is established within the clumps. Using the auto-correlation function (ACF), the typical clump size has been estimated to be $\ell_{\rm c} \sim 10\ r_{\rm S}$ and, based on the typical density of $\rho_{\rm c} \sim 10^{-6}$ g cm^{-3}, the optical depth of each clump is typically of order unity;

$$\tau_{\rm c} = \kappa_{\rm es}\rho_{\rm c}\ell_{\rm c} \sim 1. \tag{7}$$

Note that the electron scattering opacity dominates the absorption opacities in the high temperature outflow region ($\kappa_{\rm es} \sim \chi/\rho_0$). Furthermore, cross-correlation (CFF) analysis of the clumpy outflow region reveals an inverse correlation between the density and the radiation force, from which we speculate that the direction of radiative flux is involved in the formation of the structure of clumps.

To summarize, clumpy outflow has the following characteristics (see T13):
(a) Clumpy structures appear in regions in which the upward radiation force is stronger than the downward gravitational force;
(b) The optical depth of a clump is approximately unity;
(c) The radiation force is anticorrelated with the matter.

T13 further discussed the possible physical mechanisms behind clumpy outflow formation. Fact (a) suggests that clumpy outflow is Rayleigh-Taylor (RT) unstable.

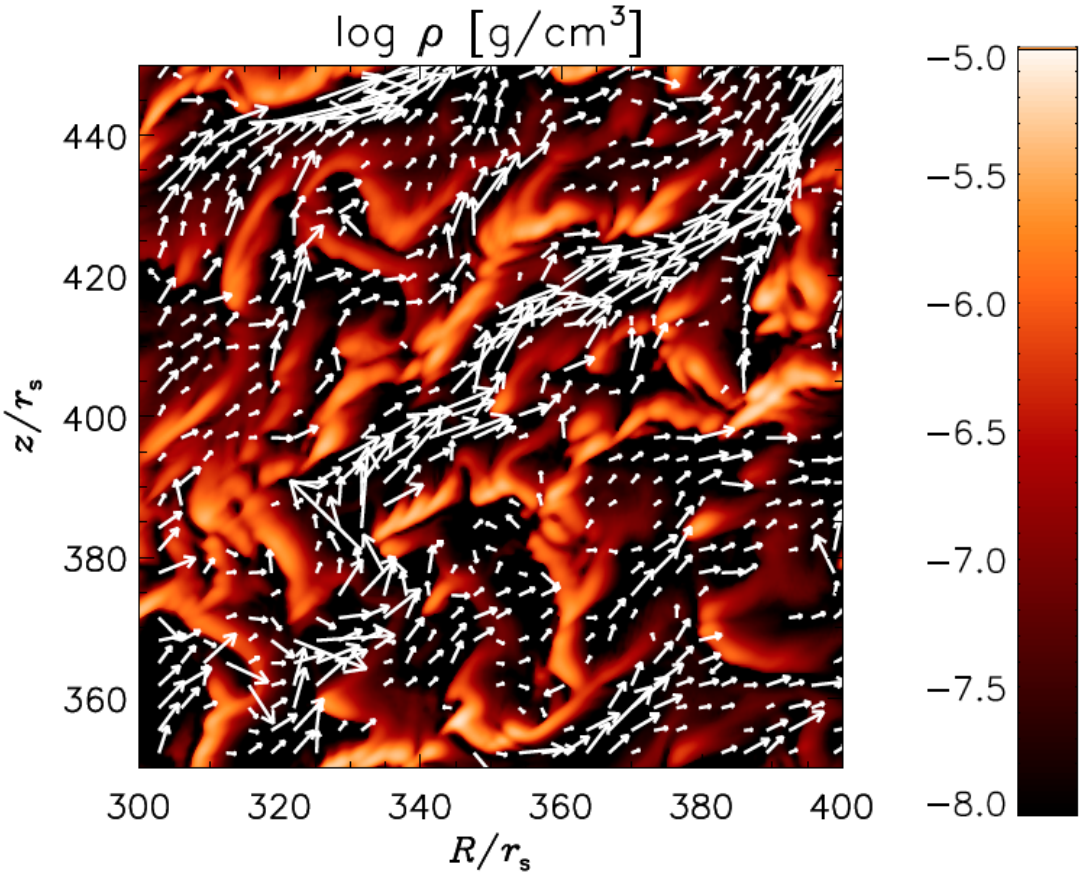

Figure 6: Matter density distribution (color) is overlaid with arrows indicating radiation force vectors per unit mass in part of the clumpy outflow region (the internal square box in the right panels of Figure 5). A arrows representing the radiative flux vectors are displayed only in the region in which their absolute values exceed 5×10^9 dyn g^{-1} confirming that longer arrows representing stronger radiation force are found predominately in the low-density regions indicated by the dark colors. The radiative flux appears to avoid dense clumpy regions, instead selectively passing through low-density channels between clumps.

However, what is encountered in this case is not the typical RT instability appearing when a heavy layer lies above a light layer in a gravity-stratified atmosphere; instead, it is radiation-related RT instability that occurs in a radiation-pressure accelerated, stratified atmosphere.

On the other hand, facts (b) and (c) suggest that the radiation RT instability is not the sole cause of the clump formation. Instead, they only imply that radiation processes are somehow involved with the clumpy formation. T13 thus argued that some sort of radiation-hydrodynamic instabilities (such as those discussed by Shaviv [2001]) are very likely to cooperate in this process and tested this idea by performing simpler RHD simulations of a super-Eddington atmosphere (see next section).

1.2.2 Super-Eddington Atmosphere Simulated by T14

Although T13 revealed the formation of clumpy outflow via global RMHD simulations, their formation mechanism was not very clear at the time. To better understand the physical mechanism behind clump formation, T14 performed a two-dimensional RHD simulation with a much simpler configuration and examined the stability of a plane-parallel, super-Eddington atmosphere with no magnetic fields. The results are shown in Figure 7. In the initial state (top panel) the upward continuum radiation force balances the sum of the downward gravitational and gas-pressure forces in the initial state. At later times (middle and bottom panels), however, upward and downward gas motions are driven by the onset of the RHD instability. The middle panel shows the growth of density perturbations with small length scales. A density pattern of up-flow ("spike") and down-flow ("bubble") structures, which is reminiscent of RT instability, is clear there. It is known that small-scale perturbations have the fastest growth rate under radiation RT instability, as is the case for pure hydrodynamic RT instability (Jacquet & Krumholz [2011]).This means that mushroom-shaped clumps can never be produced by pure RT instability, instead, radiation RT instability is responsible for the formation of one optical depth (~ 1) mushroom-shaped clumps in a super-Eddington atmosphere. To strengthen this idea, they confirmed an inverse correlation gas density and radiation pressure (Figure 7).

1.2.3 Other Features

We next investigate the role of magnetic fields in clump formation and the dependence of the black hole mass on the features of clumpy outflow. To determine if the

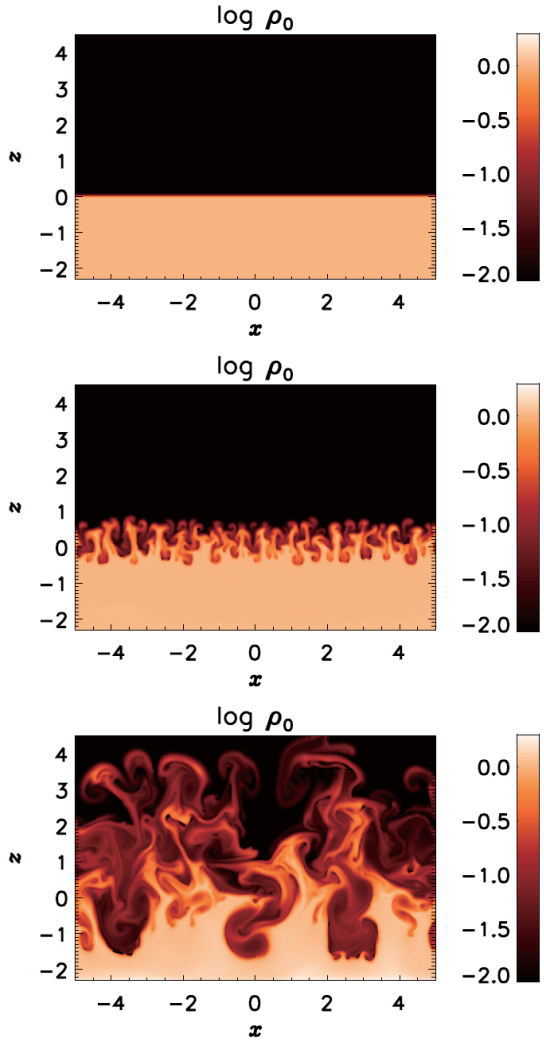

Figure 7: Time evolutionary sequence of RHD instability shown in Eddington atmosphere and parallel plane. The coloring indicates the matter density at elapsed times of $t = 0$ (top), $t = 0.90$ (middle), and $t = 1.95$ (bottom) in units of sound-crossing time over photon mean free path. Although heavy layer lies below the light layer, RT (Rayleigh-Taylor) instability occurs as the upward radiation-pressure force is larger than the downward gravitational force, this radiation RT instability is thought to be the origin of the clumpy outflow.

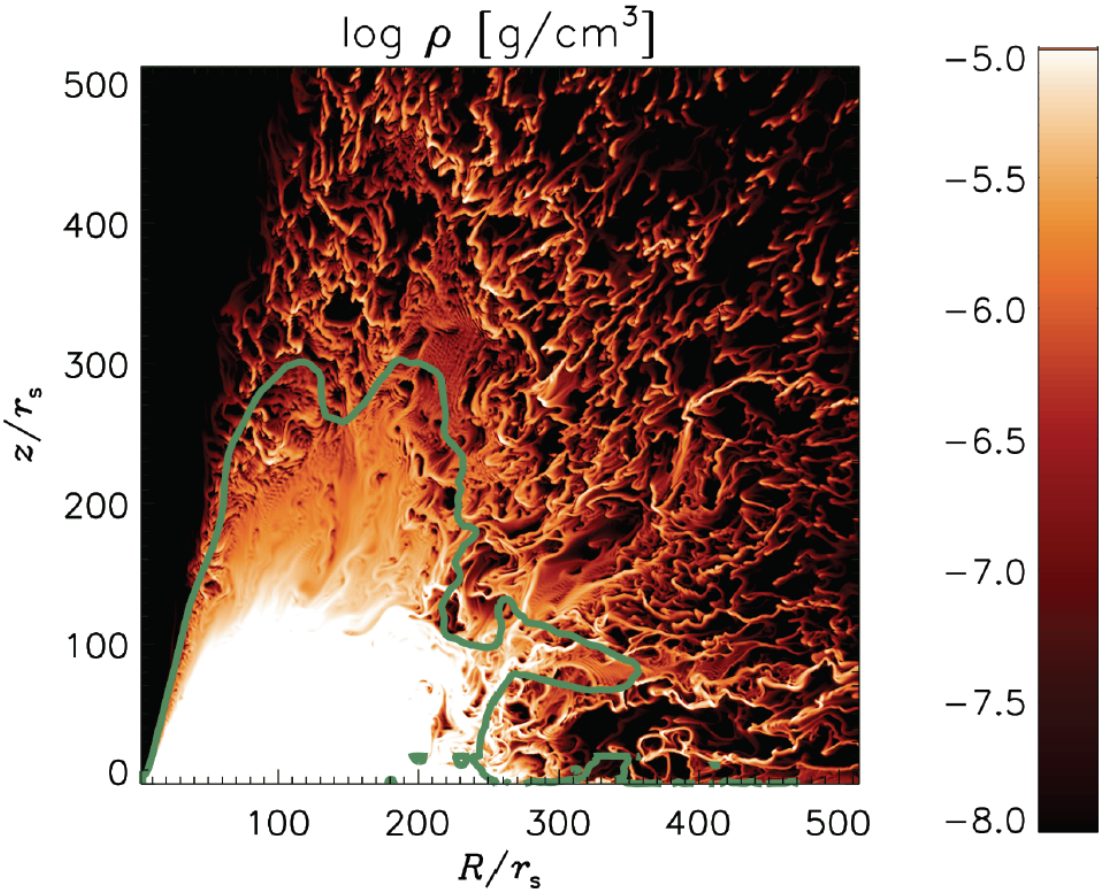

Figure 8: Two-dimensional distribution of a supercritical accretion flow and the associated outflow produced by radiation-MHD simulation with no magnetic fields. Green lines represent the surface at which the upward radiation force equals to the downward gravitational force of the central black hole. This process produces a clumpy structure similar to that in the magnetized case shown in Figure 5.

presence of a magnetic field is essential in clumpy outflow formation, T13 carried out a *nonmagnetic* RHD simulation and, as in the magnetized model, they found clumpy outflow features (Figure 8). The typical clump size was $\ell_{\rm c}$ 10 $r_{\rm S}$, which was the same as that obtained under the magnetized model. They also confirmed an inverse correlation between density and radiation. Thus, they found that a magnetic field is not essential for the formation of clumpy outflow, which suggests that magnetic photon bubble instability is not a key cause of clumpy formation. Clumpy outflows should form at even much higher black hole masses, e.g., 10^8 $M_\odot$. T13 did in fact simulate supercritical flow around a supermassive black hole and found similar clumps within the outflow (Figure 9) with a typical size of $\sim$ 10 $r_{\rm S}$, matched $\tau_{\rm c} = \kappa_{\rm es}\rho_{\rm c}\ell_{\rm c} \sim 1$. In other words, there is no mass dependence in the formation of clumpy outflow.

1.3 The Purpose of This Thesis

In the pioneering work by T13 clumpy outflow was discovered using 2-D axisymmetric RMHD simulations. We should point out, however, that they in fact produced outflow filled with "ring"-shaped clumps (rather than gas blobs), which are not very realistic. Their results are thus of limited use in application to real objects with 3-D structures. The 3-D shape of each of clumps was, for example, unknown. It is also difficult to use their results to determine the volume-filling factor of the clumps. Clarifying the 3-D nature of clumps has thus become an urgent issue and has prompted us to perform 3-D radiation hydrodynamics simulations. However, attempting to do so raises serious problems with regard to currently available computer resources, and computers are generally not powerful enough to perform full 3-D versions of the type of 2-D axisymmetric simulations carried out by T13. Therefore, it is necessary to apply a number of techniques to reduce computation time. To do this, we performed 3-D simulations of the outflow region only under the assumption that the underlying accretion flow is steady and identical to that produced by the 2-D simulations. We also decided not to solve magnetic fields, as they were shown by T13 to be nonessential to clump formation. By making these simplifications we could for the first time succeed in the global 3-D simulation of clumpy outflow.

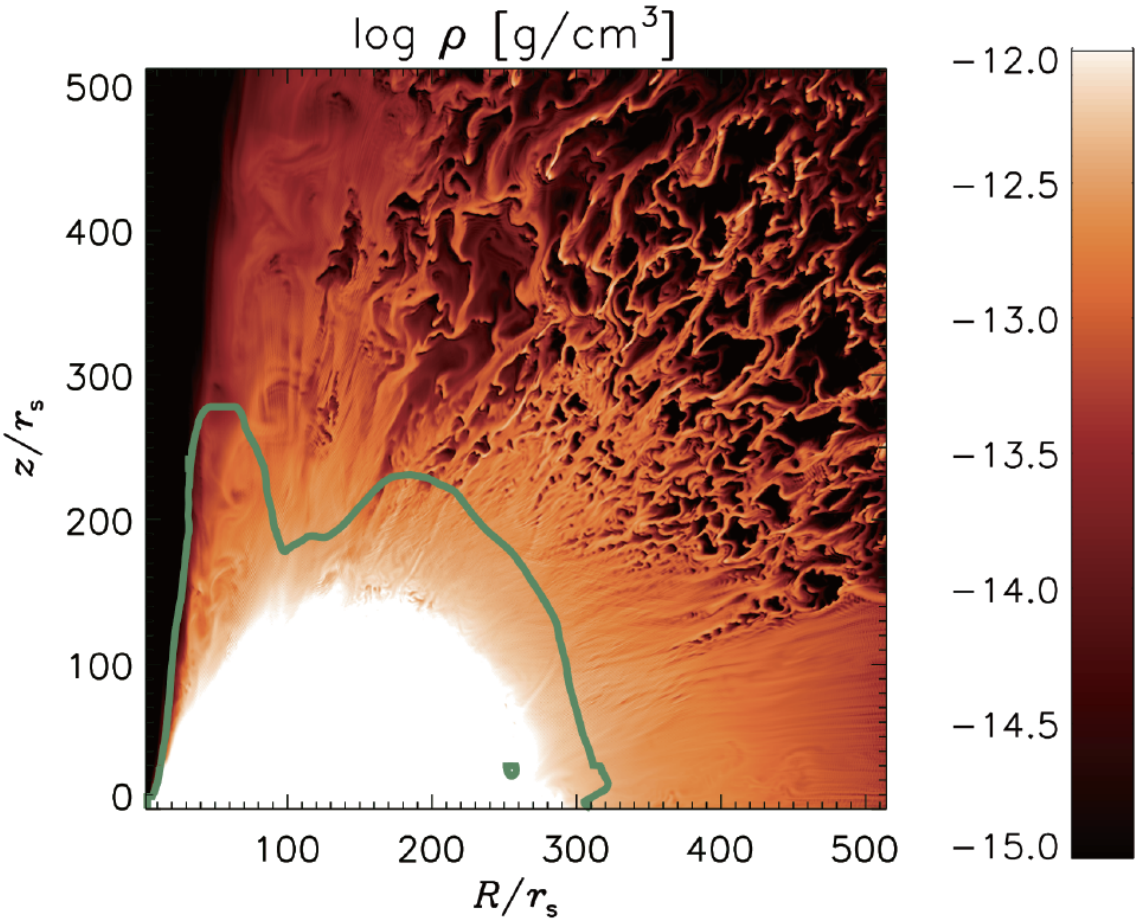

Figure 9: Two–dimensional distribution of a supercritical accretion flow and the associated outflow around a black hole with $M = 10^8\ M_\odot$ at an elapsed time of $t = 7 \times 10^7$ s. Green lines represent the surface at which the upward radiation force equals to the downward gravity force of the central black hole. A clumpy structure similar to that in the lower black hole mass case is formed, indicating that the nature of clumpy outflow does not depend on the black hole mass.

Chapter 2 Our Model, Basic Equations, and Methods of Calculation

In this chapter, we describe our model, basic equations, and the numerical calculation methods used in this study.

2.1 Our Model

Our model is, in principle, the same as that calculated by T13 but with some modifications. Such modification is inevitable, as 3-D simulations are expensive, making it impossible to calculate exactly the same model in 3-D geometry at a sufficient spatial resolution within a reasonable computational time. To reduce numerical cost while retaining a sufficient level of quality of simulation, we restrict the computational domain of 3-D simulation to the outflow region, assuming that the underlying accretion flow region is quasi-steady and identical to that obtained by 2-D simulations.

We therefore first ran 2-D simulations in the manner of T13 prior to starting our 3-D simulations. The computational domain extended from the vicinity of the black hole ($\sim 2\ r_{\rm S}$) to the outflow region at $10^3\ r_{\rm S}$. The simulations began with an initial torus in which the density peak was located at $40\ r_{\rm S}$. Within a few second of starting of the 2-D simulation, we confirmed the formation of a quasi-steady accretion flow, in which the mass accretion rate onto the black hole ($\dot{M}_{\rm acc}$) was $\simeq 10^2 L_{\rm Edd}/c^2$ and the photon luminosity was $\sim L_{\rm Edd}$. We then began 3-D simulations from the 2-D data but with azimuthal perturbations added (their explicit forms will be given later) and solved the 3-D radiation-hydrodynamics of the outflow emerging from the underlying accretion flow. The computational domain was $60 \leq R/r_{\rm S} \leq 10^3$, $0 \leq \theta \leq 90^\circ$, and $80 \leq z/r_{\rm S} < 10^3$ in cylindrical coordinates.

2.2 Basic Equations

In the cylindrical coordinates (R, θ, z), we solved the full set of RHD equations that take the terms up to the order (v/c); that is

$$\frac{\partial \rho}{\partial t} + \boldsymbol{\nabla} \cdot (\rho \boldsymbol{v}) = 0, \tag{8}$$

is the continuity equation.

$$\frac{\partial}{\partial t}(\rho \boldsymbol{v}) + \boldsymbol{\nabla} \cdot (\rho \boldsymbol{v}\boldsymbol{v} + p_{\rm gas}\boldsymbol{I}) = -\rho \boldsymbol{\nabla} \psi_{\rm PN} - \boldsymbol{S_1}, \tag{9}$$

is the momentum equation of gas.

$$\frac{\partial E_{\rm gas}}{\partial t} + \boldsymbol{\nabla} \cdot (E_{\rm gas} + p_{\rm gas})\boldsymbol{v} = -\rho \boldsymbol{v} \cdot \boldsymbol{\nabla} \psi_{\rm PN} - cS_0, \tag{10}$$

is the energy conservation equation of gas.

$$\frac{1}{c^2}\frac{\partial \boldsymbol{F_{\rm rad}}}{\partial t} + \boldsymbol{\nabla} \cdot \mathbf{P}_{\rm rad} = \boldsymbol{S_1}, \tag{11}$$

is the momentum equation of radiation, and

$$\frac{\partial E_{\rm rad}}{\partial t} + \boldsymbol{\nabla} \cdot \boldsymbol{F}_{\rm rad} = cS_0, \tag{12}$$

represents the energy equation of radiation. The source terms in the momentum and energy equations are explicitly written as

$$\begin{aligned} \boldsymbol{S}_1 &= \rho\kappa_{\rm ff}\frac{\boldsymbol{v}}{c}\left(\frac{4\pi B}{c} - E_{\rm rad}\right) \\ &- \rho(\kappa_{\rm ff} + \kappa_{\rm es})\frac{1}{c}[\boldsymbol{F_{\rm rad}} - (\boldsymbol{v}E_{\rm rad} + \boldsymbol{v} \cdot \mathbf{P}_{\rm rad})]. \end{aligned} \tag{13}$$

and

$$\begin{aligned} S_0 &= \rho\kappa_{\rm ff}\left(\frac{4\pi B}{c} - E_{\rm rad}\right) \\ &+ \rho\left(\kappa_{\rm ff} - \kappa_{\rm es}\right)\frac{\boldsymbol{v}}{c^2} \cdot [\boldsymbol{F_{\rm rad}} - (\boldsymbol{v}E_{\rm rad} + \boldsymbol{v} \cdot \mathbf{P}_{\rm rad})], \end{aligned} \tag{14}$$

respectively. Here, ρ is the matter density, $\boldsymbol{v}$ is the flow velocity, $E_{\rm gas} \equiv e_{\rm gas} + \rho\boldsymbol{v}^2/2$ is the total energy of the gas where $e_{\rm gas}$ is the internal energy density of the gas, $p_{\rm gas}$ is the gas pressure, $B \equiv \sigma T_{\rm gas}^4/\pi$ is the blackbody intensity, $T_{\rm gas}$ is the temperature of the gas, $\boldsymbol{I}$ is the unit matrix, $E_{\rm rad}$ is the radiation energy density, $\boldsymbol{F}_{\rm rad}$ is the radiative flux, and $\mathbf{P}_{\rm rad}$ is the radiation pressure tensor. For simplicity, we adopted

the gray (frequency-integrated) approximation for the radiation terms. We did not consider magnetic fields, as they have were shown by T13 to be unimportant to clump formation. Because extremely strong gravity is expected in the vicinity of a black hole, in principle general relativistic (GR) treatments is required in solving the black hole accretion problem. However, the clumpy outflow that we focused on appears in a region far from the black hole, and therefore GR effects were not essential to our purpose, and we therefore incorporated these effects by adopting the pseudo-Newtonian potential.

We considered the electron scattering opacity, and the Rosseland mean free–free absorption opacity, $\kappa_{\rm ff}$, for solar metallicity:

$$\kappa_{\rm es} = \sigma_{\rm T} m_{\rm p}^{-1}, \tag{15}$$

and

$$\kappa_{\rm ff} = 1.7 \times 10^{-25} m_{\rm p}^{-2} \rho T_{\rm gas}^{-7/2} \ {\rm cm^2 g^{-1}}, \tag{16}$$

where $m_{\rm p}$ is the proton mass and $\sigma_{\rm T}$ is Thomson scattering cross section. Equations (8)–(14) could be closed by using an ideal gas equation of state,

$$p_{\rm gas} = (\gamma - 1) e_{\rm gas} = \frac{\rho k_{\rm B} T_{\rm gas}}{\mu m_{\rm p}}, \tag{17}$$

and adopting the M1-closure, which gives the radiation pressure tensor as a function of the radiation energy density and the radiative flux (Levermore 1984). Here, $\gamma = 5/3$ is the specific-heat ratio, $k_{\rm B}$ is the Boltzmann constant, and $\mu = 0.5$ is the mean molecular weight. We assumed a black hole mass of 10 $M_\odot$. We will discuss $M_{\rm BH}$-dependencies later.

2.2.1 Initial Setting

As is mentioned in Section 2.1, creating an initial condition was a two-step process: we first performed 2-D simulation identical to that in T13 except for the size of the computational box to produce the initial condition for the 3-D simulation; we then created the initial 3-D state by adding perturbations in the azimuthal direction (see below) to the calculated 2-D data at an elapsed time of 5 s. To clarify the initial state, we show a cross-sectional view of the initial density distribution on the R-z plane in Figure 10. We confirmed that the 3-D results do not appreciably alter, even if we adopt the 2-D data at a different time (8 s, for instance) as the initial data

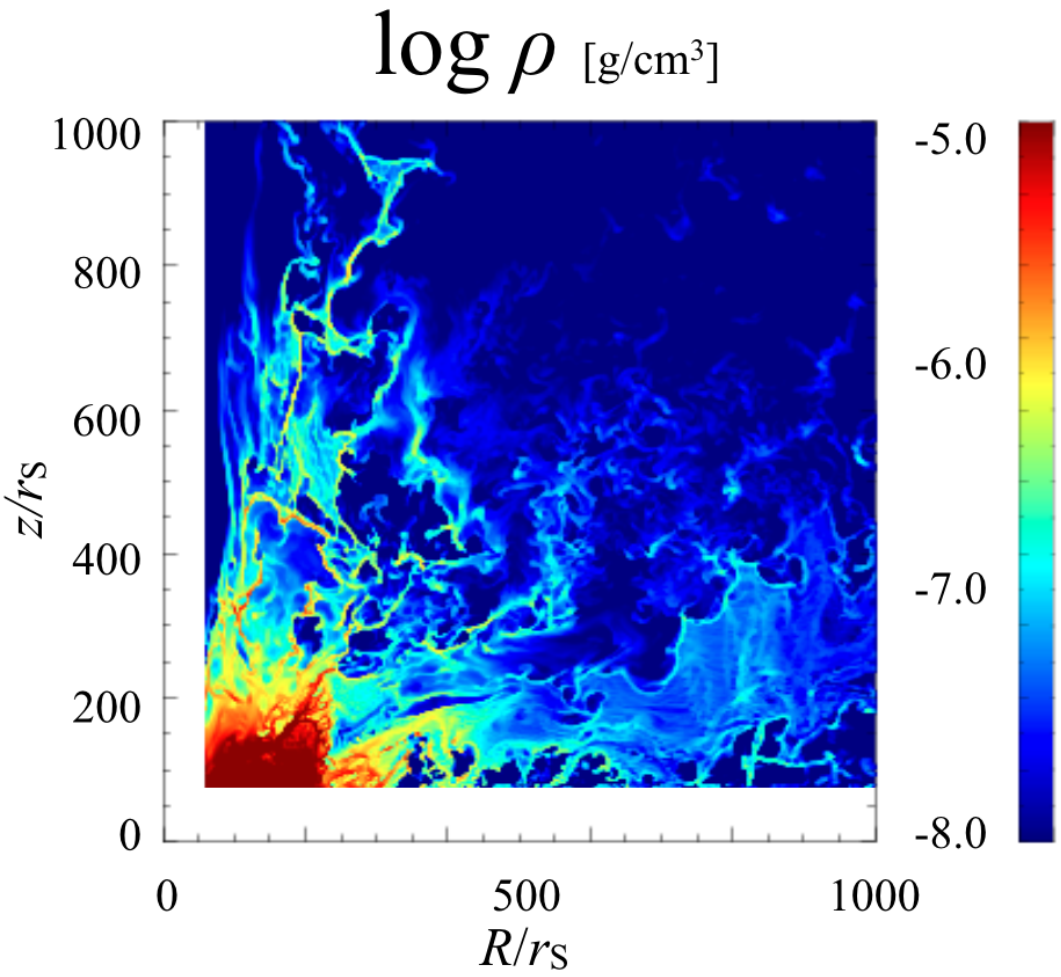

Figure 10: Density distribution used as the initial condition of the 3-D simulations in this study(see text).

for 3-D simulation. Because the original 2-D data obtained above were axisymmetric ($\partial/\partial\theta = 0$), we provided a small perturbation as follows;

$$q(R, \theta, z) = q_0(R, z) \times [1 + 0.10 \sin(4\theta)], \tag{18}$$

where q_0 are the physical quantities of the original 2-D data and q are the initial values which used in the 3-D simulations. We confirm that our results do not appreciably change, even if we employ random numbers between -1 and 1 instead of $\sin(4\theta)$ at each grid point. In our simulations, we assumed the same type of perturbations in all physical variables.

2.2.2 Boundary Conditions

As mentioned earlier, we restricted the computational domain of 3-D simulation to the outflow region (see Section 2.1 and Figure 11). At the inner boundary at $R = 60\ r_{\rm S}$ or the lower boundary at $z = 80\ r_{\rm S}$, we retained the same values for physical quantities such as matter density, temperature, velocity vectors, radiation energy density, and radiative flux at all later times in the 3-D simulation, i.e., we employed fixed boundary conditions at the inner and lower boundaries. This equates to the specification of a steady disk with $\dot{M}_{\rm acc} \sim 10^2 L_{\rm Edd}/c^2$ just inside and below the simulation box throughout the 3-D simulation. We adopted free boundary conditions at the outer and upper boundaries ($R = 10^3\ r_{\rm S}$ and $z = 10^3\ r_{\rm S}$). If the R-component (z-component) of the velocity was negative, it was automatically set to zero at the outer (upper) boundary; thus, matter could exit freely but not enter through the boundaries. The periodic boundary condition was used in θ-direction making the mass, momentum, energy, and radiation at the boundary at $\theta = 0^\circ$ the same as at the boundary at $\theta = 90^\circ$. The respective grid spacings were $\Delta R = \Delta z = 4.0\ r_{\rm S}$ and $\Delta\theta = 0.9^\circ$. Here we note that the numerical resolution somewhat affected the clump size (as will be discussed later). Our total simulation time was 12 s, which was much longer than the wind crossing time of $10^3\ r_{\rm S}/v_r \sim 1.0$ s for a black hole of mass 10 $M_\odot$ and a radial wind velocity of $v_r \sim 0.1c$. From this, we conclude that we ultimately achieved a quasi-steady structure of clumpy outflow.

For comparison purposes, we also performed 2-D axisymmetric simulations using the same computational domain and grid spacing as in the 3-D simulations ($60 \leq R/r_{\rm S} \leq 10^3$, $80 \leq z/r_{\rm S} < 10^3$, and $\Delta R = \Delta z = 4.0\ r_{\rm S}$) with the physical quantities of the original 2-D data, q_0, employed as the initial values. As in the case with the

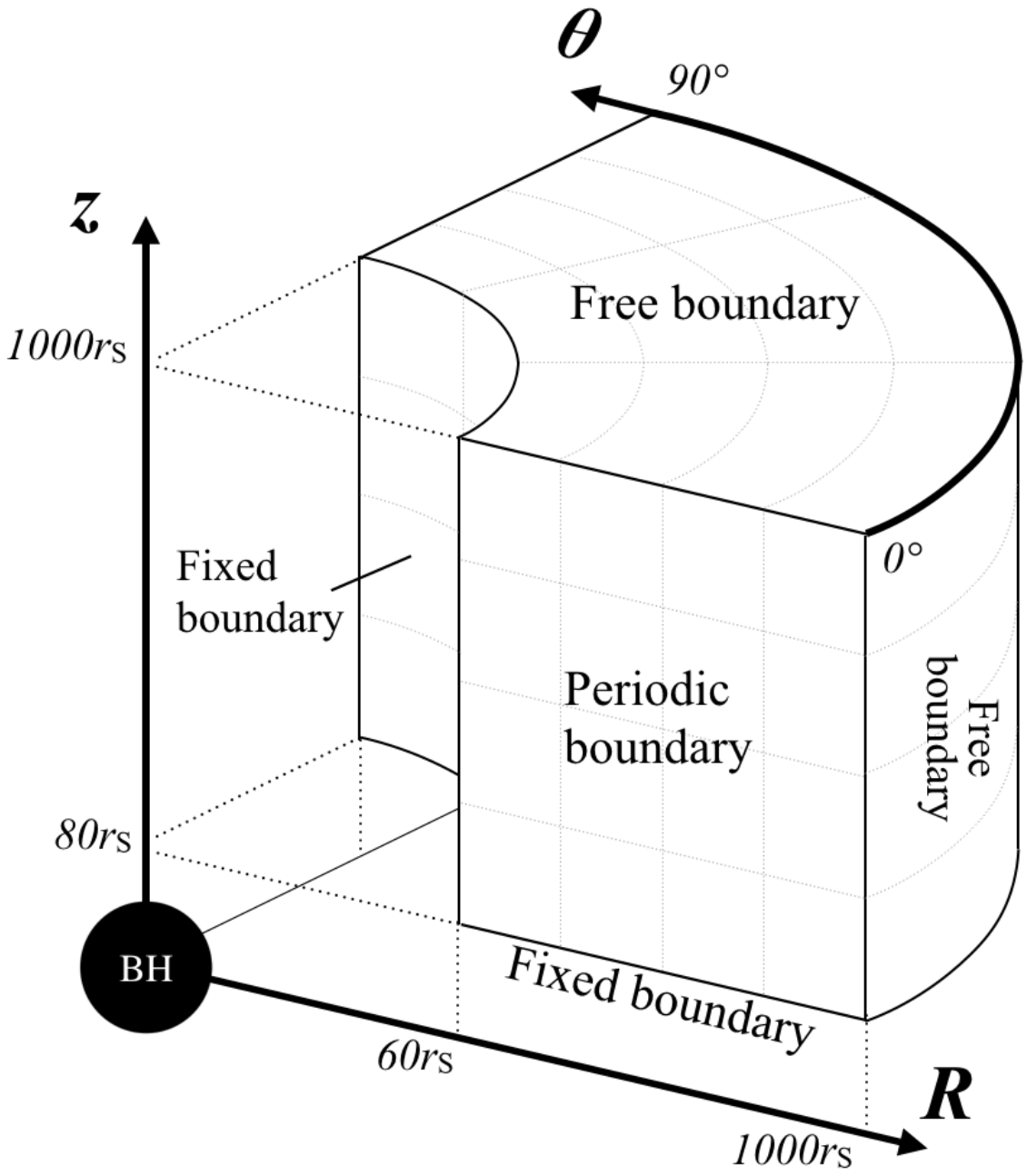

Figure 11: Geometry of calculation box and the adopted boundary conditions. We solved the outflow region above and outside the fixed boundaries.

3-D simulations, we used free boundary conditions at the outer and upper boundaries and fixed boundary conditions at the inner and lower boundaries.

2.2.3 Numerical Method

Our numerical code is an extension of CANS+ (Matsumoto et al. [2016]), a high-resolution MHD simulation code package developed by Chiba Univ. (The magnetic fields were set to zero in our simulations). The hydrodynamic terms were solved using CANS+, while the method for solving radiation terms was essentially identical to that described in Takahashi & Ohsuga [2013]. Here, we note that, although CANS+ is able to solve fully special relativistic equations, we restricted the RHD equations to $\mathcal{O}(v/c)$ in our simulations.

Chapter 3 Properties of Clumpy Outflow

3.1 Overall Structure

An overall 3-D structure of inflow and outflow gas is shown in Figure 12, which presents a bird's eye view of the matter density distribution for the regions with density higher than 5×10^{-7} g cm^{-3}. In the figure, the black hole is located in the central lower region surrounded by the blue accretion disk region. The outflow is launched from the disk by the strong radiation force, with outflowing matter blown away while being slowly rotated. This outflow fragments into many clumps, and we see multiple sheet-like structures in the outflow region (above $z \sim 400\ r_{\rm S}$). Closer inspection of each sheet reveals that its shape is neither an ellipsoid nor a thin, spaghetti- or linguini-like string but more like a flattened string or a torn sheet (like fettuccine or lasagna). This feature is not anticipated in 2-D simulations and is revealed for the first time by our 3-D simulation. Figure 13 shows a set of 2-D cross-sectional views of the spatial distribution of matter density (left panels), temperature ratio (middle), and velocity fields (right) of the 2-D and 3-D simulation results. From the top to bottom panels we plot the structure on the R-z plane calculated by the 2-D axisymmetric simulations, the structure on the R-z plane (or constant θ plane) plotted by the 3-D simulation, and the structure on the X-Y plane (constant z plane), respectively. Here, we define the Cartesian coordinate system $(X, Y) \equiv (R\cos\theta, R\sin\theta)$ for a fixed height, z.

It is interesting to see if there are qualitative differences between the 2-D and 3-D results: it is obvious that the 2-D simulations miss the non-axisymmetric structure, but what is captured in the cases seen in the R-z plane?

We first focus on the matter density contours (left panels of Figure 13). Here, we recognize clumpy density structures above a certain height ($z >$ several hundreds of $r_{\rm S}$) not only in the R-z plane but also in the X-Y and $Rd\theta$-z planes, although we don't plot the $Rd\theta$-z plane is not plotted in the Figure 13.

It should be noted that the 2-D and 3-D simulations produce density contours on

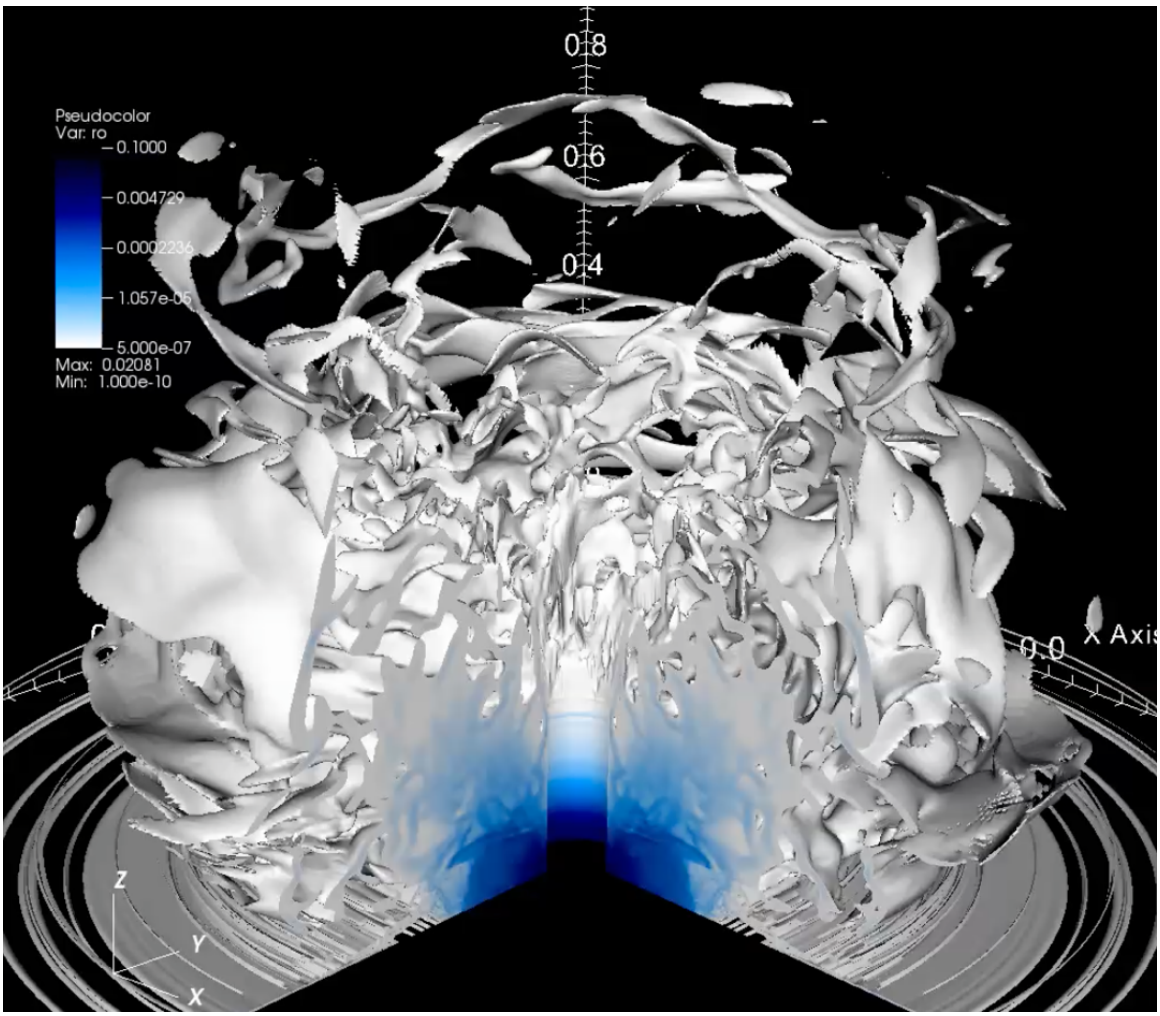

Figure 12: Bird's eye view of the 3-D matter density structure of a supercritical accretion flow and associated outflow around a black hole with $M = 10\ M_{\odot}$ at an elapsed time of $t = 2.5$ s. Here, we display only the regions where matter density is higher than 5×10^{-7} g cm^{-3}. The coloration (silver – blue) represents the matter density (see the upper-left corner for the color scale); denser regions (indicated by the blue coloration) are found within the inner inflow region, while less dense regions (indicated by the silver coloration) are primarily outflow regions.

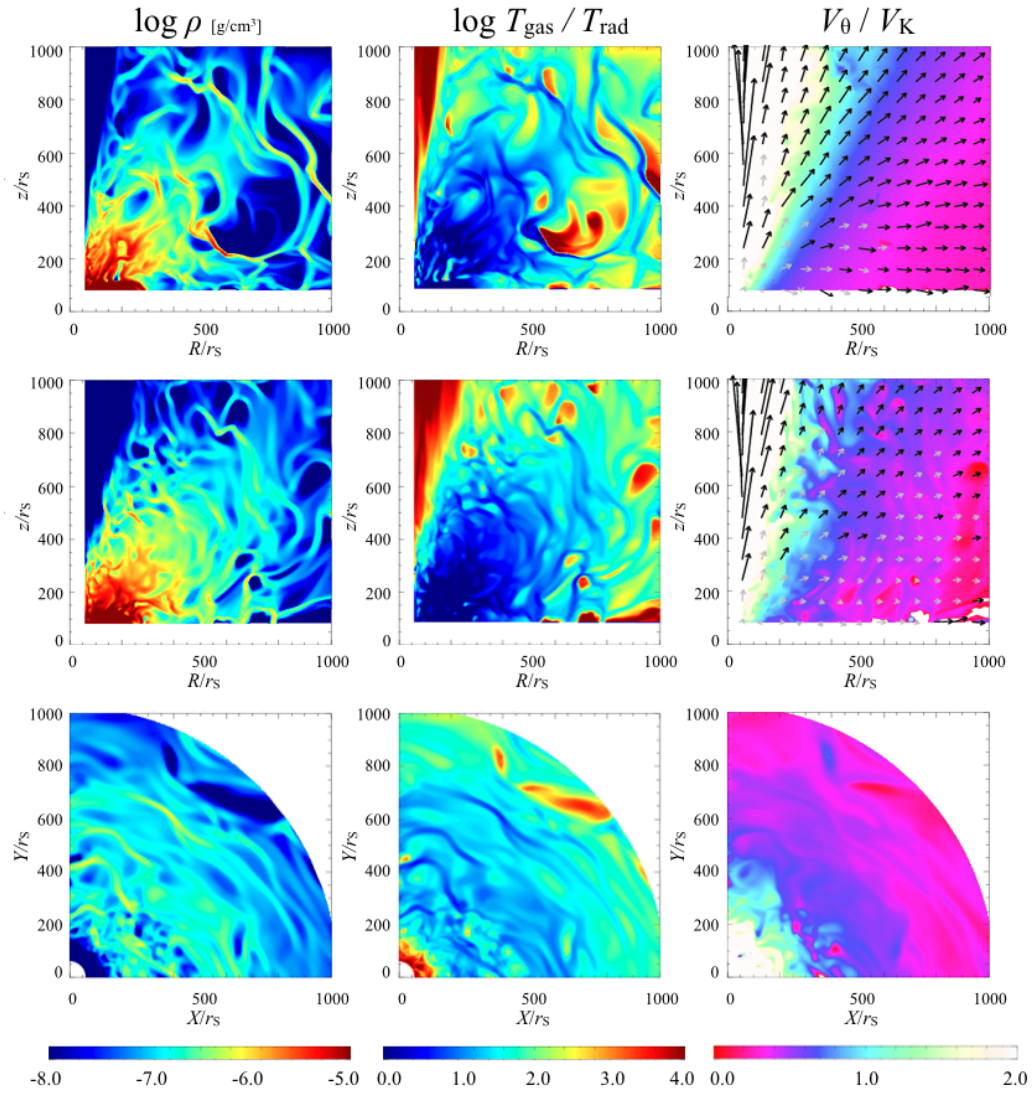

Figure 13: Summary of 3-D simulation results sliced in two-dimensional planes in comparison to 2-D results. From the top to bottom panels, we plot cross-sectional views of the flow structure in the R-z plane calculated by the 2-D simulation (upper panels), views on the R-z plane at $\theta = 45°.0$ calculated by the 3-D simulations (middle panels), and views on the X-Y (or $R\cos\theta$-$R\sin\theta$) plane at $z = 600\ r_S$ calculated by the 3-D simulations, respectively. In each panel row, we plot the matter density (left panels), the temperature ratio, T_{gas}/T_{rad} (middle panels), and the toroidal velocity fields V_θ overlaid with the poloidal velocity vectors (right panels). The toroidal velocity in the right panels is normalized by the Keplerian orbital velocity, V_K (see text for definition). Color scales are indicated below the bottom panels. The simulation parameters and elapsed time are the same as those in Figure 12. Note clumpy structures seen in all the matter density plots.

the R-z planes that are remarkably similar, which justifies the 2-D simulation results. However, the widths of the individual clumps appear somewhat thinner in the 3-D calculations; this point will be quantified later based on auto-correlation function (ACF) analysis (see subsection 3.2.). Furthermore, the clumpy structure tends to be weakened at the time-averaged density contours. Figure 14 shows the density distribution in the R-z plane time-averaged over $0 - 10$ s. It is seen that the time-averaged density tends to decrease with the distance from the black hole, a trend also seen in Figure 13. However, the clumpy structure does not appear in Figure 14, indicating that the clumpy structure is not fixed but fluctuates significantly. We will show in the next subsection (again based on the ACF analysis) that the clumpy feature are also smoothed in forming the azimuthal average.

It is interesting to examine the correlation of matter- and radiation-related quantities from inspection of the left and middle panels of Figure 13. On the surface, they appear similar except for their coloration. This was previously pointed out by T13 who claimed anti-correlation between the matter density and the ratio of gas temperature, $T_{\rm gas}$, to the radiation temperature, $T_{\rm rad}$. To be more precise, we notice that clumpy structures (with higher densities above $\sim 500\ r_{\rm S}$) appear in the region in which the temperature ratio is smaller; e.g., the yellow clump (dense region) extending from $(R, z) = (600\ r_{\rm S}, 850\ r_{\rm S})$ to $(750\ r_{\rm S}, 550\ r_{\rm S})$ in the middle left panels correspond to the blue region (where $T_{\rm gas} \sim T_{\rm rad}$) in the middle panel of the middle row. This is consistent with the 2-D results reported by T13. A similar type of anti-correlation is found in the X-Y plane (see bottom left and middle panels). Here, Figure 15 shows the gas temperature and radiation temperature of 3D simulation. The radiation temperature is highest in the region of accretion disk, and it decreases as going to the outside. On the other hand, the gas temperature is low ($\sim 10^6$ K) in the region of accretion disk, and it roughly increases with distance from the BH. In particular, it is high temperature ($\geq 10^9$ K) in the low density region around the z-axis and outflow region. Since the opacity of the bremsstrahlung depends on the square of the density, it is considered that the cooling efficiency of the gas is lowered. In fact, as can be seen from Figure 13, the temperature of gas and radiation are separated in high temperature and low density region ($T_{\rm gas} > T_{\rm rad}$). Since the temperature of the gas is 10^6 K or more even at the low temperature part, it is considered that the hydrogen is in a completely ionized state (for ionization state of metal element,

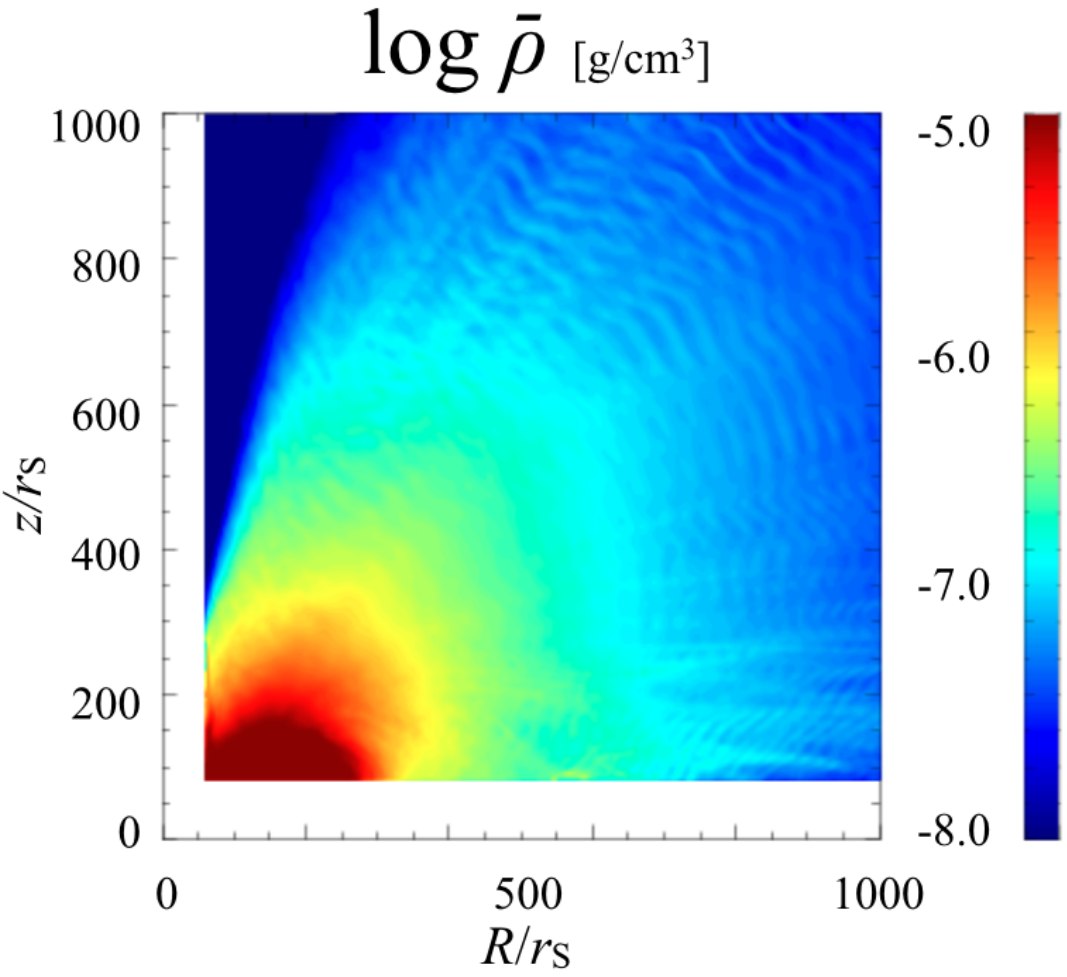

Figure 14: Time-averaged density distributions of 3-D simulation results in the R-z plane at $\theta = 45°.0$ during the time span $t = 0 - 10$ s in increments of 0.1 s. The simulation parameters are the same as those in Figure 13.

see section 4.2 for estimation of ionization parameter).

Next, we compare the velocity fields of the 2-D and 3-D models. The right panels of Figure 13 plot the azimuthal velocity (V_θ) normalized by the Keplerian orbital velocity, $V_{\rm K}$ defined as the azimuthal velocity needed for matter to rotate on a circular orbit around the z-axis at a fixed z:

$$V_{\rm K} \equiv \sqrt{\frac{GM_{\rm BH}R^2}{r^3}}. \tag{19}$$

where $r \equiv \sqrt{R^2+z^2}$. The black arrows represent the region in which the gas velocity exceeds the escape velocity.

A smoother V_θ distribution is seen in the 2-D simulations than in the 3-D simulations. This is particularly true in the interface between the inflow regions (with blue coloration), which is nearly straight in the 2-D results (right panel) but not straight in 3-D results. The effect in the 3-D results is caused by significant turbulent motion rising in the interface, which produces significant velocity fluctuations. In the region around the z-axis, a jet is launched with super-Keplerian rotation velocity, i.e., the jet material trends outward but does not produce a full expanding motion. This indicates that the jet material is confined by an external-pressure asserted by the matter outflow. It is interesting to note that, in the bottom right panel, the toroidal velocity is primarily sub-Keplerian at large $R(> 400\ r_{\rm S})$. The rotating in this region, however, is moving outward not because of the centrifugal force but because of the outward radiation-pressure force. We understand this to indicate that the material is being blown away while retaining its angular momentum, as the radiation force in the θ-direction is too small to change the angular momentum. This is clearly seen in Figure 16, in which we plot the angular momentum, RV_θ, normalized by $r_{\rm S}c$. In this figure, along the direction $\varphi \equiv \tan R/z^{-1} = 45°.0$ (which is the inclination angle) there is red (or orange) coloration from the disk region ($r \leq 300\ r_{\rm S}$) to the outflow region($r \geq 300\ r_{\rm S}$). This indicates that the outflow blown away from the disk retains its angular momentum and, therefore, that the rotational speed normalized by the Keplerian velocity decreases with the distance from the launching point (see right panels in Figure 13). It is also important to note that significant sub-Keplerian rotation corresponds to slow rotational speed, which in turn leads to long variation timescales as a result of the obscuring of the central photon flux by moving clumps. Thus, simple timescale calculations based on the assumption of Keplerian rotation

could be grossly underestimating, as will be discussed in subsection 4.1.2.

3.2 Auto-Correlation Analysis

To examine the statistical properties of the clumps, it is useful to calculate the auto-correlation functions (ACFs, see T13). The ACF of the density, as a function of the radial interval (δR), is given as

$$C(\delta R) \equiv \frac{\sum_{k=0}^{N_R-L_k-1} (\rho_{k+L_k} - \bar{\rho}_R)(\rho_k - \bar{\rho_R})}{\sum_{k=0}^{N_R-1} (\rho_k - \bar{\rho}_R)^2}, \tag{20}$$

where $\bar{\rho}_R$ is the density averaged in the R-direction,

$$\bar{\rho}_R \equiv \frac{1}{N_R} \sum_{k=0}^{N_R-1} \rho_k. \tag{21}$$

where $N_R(= 235)$ is the total number of radial grid points, the subscript k represents the radial grid number, and L_k is an integer specifying δR as $\delta R = L_k \times \Delta R$, where we take the constant radial grid spacing; $\Delta R = 4.0\ r_{\rm S}$. In the same manner, the ACF of the density, as a function of the azimuthal interval ($\delta\theta$), is calculated by

$$C(\delta\theta) \equiv \frac{\sum_{l=0}^{N_\theta-L_l-1} (\rho_{l+L_l} - \bar{\rho}_\theta)(\rho_l - \bar{\rho}_\theta)}{\sum_{l=0}^{N_\theta-1} (\rho_l - \bar{\rho}_\theta)^2}, \tag{22}$$

where $\bar{\rho}_\theta$ is the density averaged in the θ-direction,

$$\bar{\rho}_\theta \equiv \frac{1}{N_\theta} \sum_{l=0}^{N_\theta-1} \rho_l. \tag{23}$$

where $N_\theta(= 100)$ is the total number of azimuthal grid points, the subscript l represents the azimuthal grid number, and L_l is an integer specifying $\delta\theta$ as $\delta\theta = L_l \times \Delta\theta$, where we take the constant radial grid spacing; $\Delta\theta = 0^\circ.9$. In the upper panels of Figures 3.2 and 17, we represent the ACFs of the density on the X-Y plane as functions of $\delta R/r_{\rm S}$ at various angles θ (Figure 3.2) and as functions of θ at various distances R (Figure 17). In both panels, we fix $z = 600\ r_{\rm S}$. The density structure on the plane $z = 600\ r_{\rm S}$ is shown in Figure 13. We find from the upper panel of Figure

3.2 that clumps are separated from each other by distance of $\sim 50 - 150\ r_{\rm S}$ in the R-direction, as the interval between the primary ($\delta R/r_{\rm S} = 0$) and secondary peaks corresponds to the separation between neighboring clumps. The panel also indicates that the distance from the first to the second peak varies with θ; that is, the clump intervals vary by θ. In addition, we see from the upper panel of Figure 17 that the clump intervals in the θ-direction differ ($\sim 15 - 30^\circ$) according by R, from which we conclude that there is no coherence in clump distribution. Such irregularities in the clump interval can be more clearly understood from inspection of the lower panels in Figures 3.2 and 17. In the lower panel of Figure 3.2, we plot the ACFs of the density as a function of $\delta R/r_{\rm S}$ at $\theta = 45^\circ$ (red line) and the azimuthally averaged ACFs (black line) obtained by the 3-D simulations, while the blue-dotted line indicates the ACFs obtained from the 2-D simulations. We also show the ACFs of the density as a function of $\delta\theta$ at $R = 740\ r_{\rm S}$ (red) and of the density function averaged in the R-direction (black). Here, we fix the height of crosscut to $z = 600\ r_{\rm S}$. However, the azimuthally averaged ACF (black line) is much smoother, indicating that, as mentioned above, the separation between neighboring clumps is quite complicated (see also Figure 5). From these ACF profiles, we can extract a typical clump size and interval between neighboring clumps in the following manner. First, the width of the primary peak (at $\delta R = 0$) can be used to represent the typical clump size. As we find similar slopes for each ACF near $\delta R \sim 0$ in the upper panel of Figure 3.2, we conclude that the clump width is $\ell^r_{\rm cl}/2 \sim 15\ r_{\rm S}$ regardless of the azimuthal angle.

Second, the interval between the primary and secondary peaks at $\delta R \simeq 60\ r_{\rm S}$ represents the separation between neighboring clumps. We see significant variations in the ACF shapes around the secondary peaks, indicating different clump intervals at different θ. This is supported by the lack of clarity in the black line representing the secondary peak of the bottom panel of Figure 3.2 when averaging the ACF by the azimuthal angle θ. In other words, there is no coherence in clump distribution by azimuthal angle. This feature can also be seen from close inspection of the lower left panel of Figure 13, in which we see a number of clumps in the radial direction that are not equidistant. The bottom panel of Figure 17 plots the ACFs as a function of $\delta\theta$ at a fixed $R = 740\ r_{\rm S}$ (red line) and the azimuthally averaged ACFs (black line) obtained by the 3-D simulations. The typical clump size in the azimuthal direction is 3° (corresponding to $\sim 40\ r_{\rm S}$ at $R = 740\ r_{\rm S}$), while the typical interval of clump in

the azimuthal direction is 25° (corresponding to $\sim 320\ r_{\rm S}$ at $R = 740\ r_{\rm S}$).

To compare the ACFs of the 2-D and 3-D results more quantitatively, the bottom panels of Figure 17 plot the ACFs based on the 2-D simulations (blue dotted line). As expected from of the comparison the density contours shown in Figure 13, we see that the clump width is thinner in the 3-D simulations than in the 2-D simulation.

We have estimated the typical clump size in the R and θ directions from the ACFs for an arbitrarily chosen $z = 600\ r_{\rm S}$; next, we examine how this changes if we change z. The upper panels of Figure 18 show the color contours of ACFs in the R direction at various z positions. The width of the brown region in the δR direction at fixed z shows the typical size of high density regions. The upper three panels represent ACFs at different θ(from left to right $\theta = 22°.5, 45°.0$, and $67°.5$). In all the three upper panels, the clump sizes are very large in the range $z \leq 400\ r_{\rm S}$ and the secondary peaks do not appear; this region is recognized as the disk. Hereafter, we focus on $z \geq 400\ r_{\rm S}$, which is considered to be the outflow region. Based in an estimate of the clump size at each height z within the outflow area ($z \geq 400\ r_{\rm S}$), we roughly estimate the height z in Figure 3.2 as $\ell^r_{\rm cl}/2 \sim 15\ r_{\rm S}$, i.e., the clump size in the R direction is nearly independent of the height. However, as already discussed, the distance between clumps varies depending on the height, while there is no significant difference in terms of θ. The bottom panels of Figure 18 show color contours of ACFs in the θ direction at various heights z. The width in the $\delta\theta$ direction of the brown region near $\delta\theta = 0^{circ}$ represents the typical clump size in the azimuthal direction at that height, z. The three lower panels in the figure show ACFs at different R (from left to right, $R = 300, 500$, and $700\ r_{\rm S}$). These panels show that the clump size is roughly 3°, and the distance between the clumps varies depending on the position (R,z). Figure 19 shows the ACFs in the R direction set as a function of z derived from the results of the two-dimensional simulation. This figure is roughly the same as that in the upper panels of Figure 18; even using the two-dimensional simulation results, the clump size in the outflow region is approximately $\ell^r_{\rm cl}/2 \sim 25\ r_{\rm S}$ constant irrespective of the position, although the distance between the clumps is variable.

We see that ACF analysis is of limited use, as it can be easily gathered from a quick look at the lower-left panel of Figure 13 that all of clumps are stretched out approximately (but not precisely) along the azimuth direction with lengths much greater than $\sim 30\ r_{\rm S}$ of on the order of $\sim$ several hundreds of $r_{\rm S}$. The much shorter

correlation length in the ACF analysis in the azimuth direction is the fact that each clump does not have a straight shape but shows wavy structure. This fact will be essential in discussing the obscuring of the central light by floating clumps.

3.3 Influence of Perturbation

Our above results were obtained using 3-D simulations with small perturbations in the azimuthal direction, as expressed in Equation (18). Here we show that these results are not sensitive to initial perturbation. To establish this, We performed simulations at various perturbations given by

$$q(R, \theta, z) = q_0(R, z) \times [1 + p_{\rm pertu} A_{\rm shape}]. \tag{24}$$

where $p_{\rm pertu}(= 0.1 \text{ or } 0.5)$ is the amplitude of perturbation, and $A_{\rm shape}$ is set to $\sin(4\theta)$ or to random numbers between -1 and 1. Our four models are summarized in Table 1. P1 is the basic model discussed in the preceding subsections. In Figure 20, we plot

Table 1: parameters of perturbation

Model	$p_{\rm pertu}$	$A_{\rm shape}$
P1	0.1	$\sin(4\theta)$
P2	0.1	Random numbers
P3	0.5	$\sin(4\theta)$
P4	0.5	Random numbers

cross-sectional views of the flow structure in the X-Y plane at $z = 700\, r_{\rm S}$. Comparing P1 (upper-left) and P2 (lower-left), we find that the density contours are very similar. A string-like structure composed of dense matter ($> 10^{-7}\mathrm{g\,cm^{-3}}$) appears and there is a peak density of around ($10^{-6}\mathrm{g\,cm^{-3}}$) in each panel. In addition, the clump (string) thicknesses are nearly the same. We conclude from this that the clumpy structure does not depend on the shape of the perturbation.

Clumpy structures are generated even if a larger amplitude perturbation, $p_{\rm pertu} = 0.5$ is applied. The string-like structures are seen in the right-hand panels of figure, which correspond to the higher perturbation level, although the average density appears to be slightly larger (smaller) for P3 (P4) model than for the P1 model. This difference in terms of the average density might be eliminated if we performed

long-term calculations; such simulations will be left for future work. As the clumpy structure appears in all models, we can conclude that our results are not sensitive to initial perturbation.

Here, we stress that the small wavelength perturbations do not have a significant on the final structure of the clumpy wind. Although this can be roughly ascertained from a comparison between the P1 and P2 results, we tested this further analytically as follows. We prepared a computational domain that was restricted in the azimuthal directions to $\theta = 9^\circ.0$ ($\Delta\theta = 0^\circ.375$) with a very high resolution in the θ-direction to enable treatment of perturbations with small wavelength. The box size in the R- and z-directions and the boundary conditions were the same as in the previous simulations. We added azimuthal perturbations using a sin function with an amplitude of 10 % and wavelengths (4θ) corresponding to 9° and $4^\circ.5$. In Figure 21, we show the density distributions on the horizontal plane at $z = 700\ r_{\rm S}$ are shown for $4\theta = 9^\circ.0$ (left panel) and $4^\circ.5$ (right panel). Here the elapsed time is 5 s at which the flow is in the quasi-steady state. We find no significant differences between the two panels. Importantly, the high-density elongated structures with apparent angle-widths of $> 9^\circ.0$ appear in the region $R \geq 500\ r_{\rm S}$ in both panels; this suggests that initial small-wavelength perturbations do not affect the ultimate clumpy structure obtained as the global mode grows. Simulations at a larger angular range, as are carried out in the present work are required to reveal the clumpy structure.

3.4 Formation Mechanism of Clumpy Structure

The occurrence of clumpy gas cloud structures is not unique to black hole objects but is known to occur in a wide variety of astrophysical objects. The best-known case thermal instability (Field 1965) leading to the production of two-phased media in interstellar space, solar atmospheres, and other regions. Radiation-induced (Shaviv 2001) and photon-bubble instability (Arons 1992) are also discussed in the context of luminous objects.

In discussing the formation mechanism of clumpy outflow, it is instructive to refer to the discussion of the T13 2-D RHD simulations, in which following key features are summarized:

(i) the clumpy structure appears in the upwardly accelerating layer as a result of the radiation force;

(ii) the optical depth of the clump size is around unity;
(iii) a clear anti-correlation is found between the gas density and the absolute value of radiation force; and
(iv) the cloud temperature varies in a complex manner.

With the exception of (iv), our 3-D simulation confirms most of these features. For example, item (i) is obvious from the model setting. We also confirm item (ii) within our numerical resolution (see Appendix B for details); that is, from the typical (radial) clump size of $\ell_{\rm cl}^r \sim 30\ r_{\rm S} \sim 10^8$cm and the typical density of $\rho_{\rm cl} \sim 10^{-7}$ g cm^{-3} (the top left and middle left panels of Figure 13), we find a scattering optical depth of a few $\tau_{\rm es} = \kappa_{\rm es}\rho_{\rm cl}\ell_{\rm cl}^r$. It is very important to note that this value does not depend on the black hole mass, which allows us to discuss for the outflow from supermassive black holes; this is a natural consequence of the following scaling relations (see T13). Our inability to confirm item (iv) is probable a result of our limited numerical resolution. We therefore tentatively conclude that radiation Rayleigh-Taylor instability coupled with some degree of radiation hydrodynamic instability could be a key cause of clump formation; more detailed discussion is left as future work.

Another interesting issue concerns the origin of the torn-sheet clump structures. We conjecture that this asymmetry in the 3-D structure could be understood in terms of the anisotropic radiation field in the sense that a radiation flux that is super-Eddington only in the radial direction would result in a torn-sheet structure. Further extensive study is needed to confirm if this conjecture is justified.

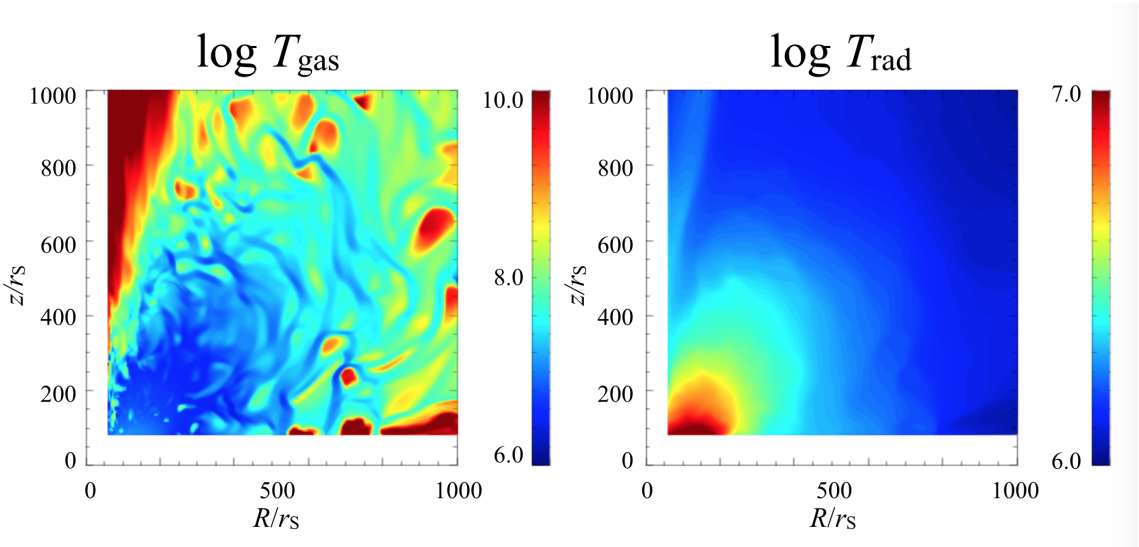

Figure 15: Gas temperature (left panel) and radiation temperature (right panel) of simulation results in the R-z plane at $\theta = 45°.0$. The simulation parameters are the same as those in Figure 13.

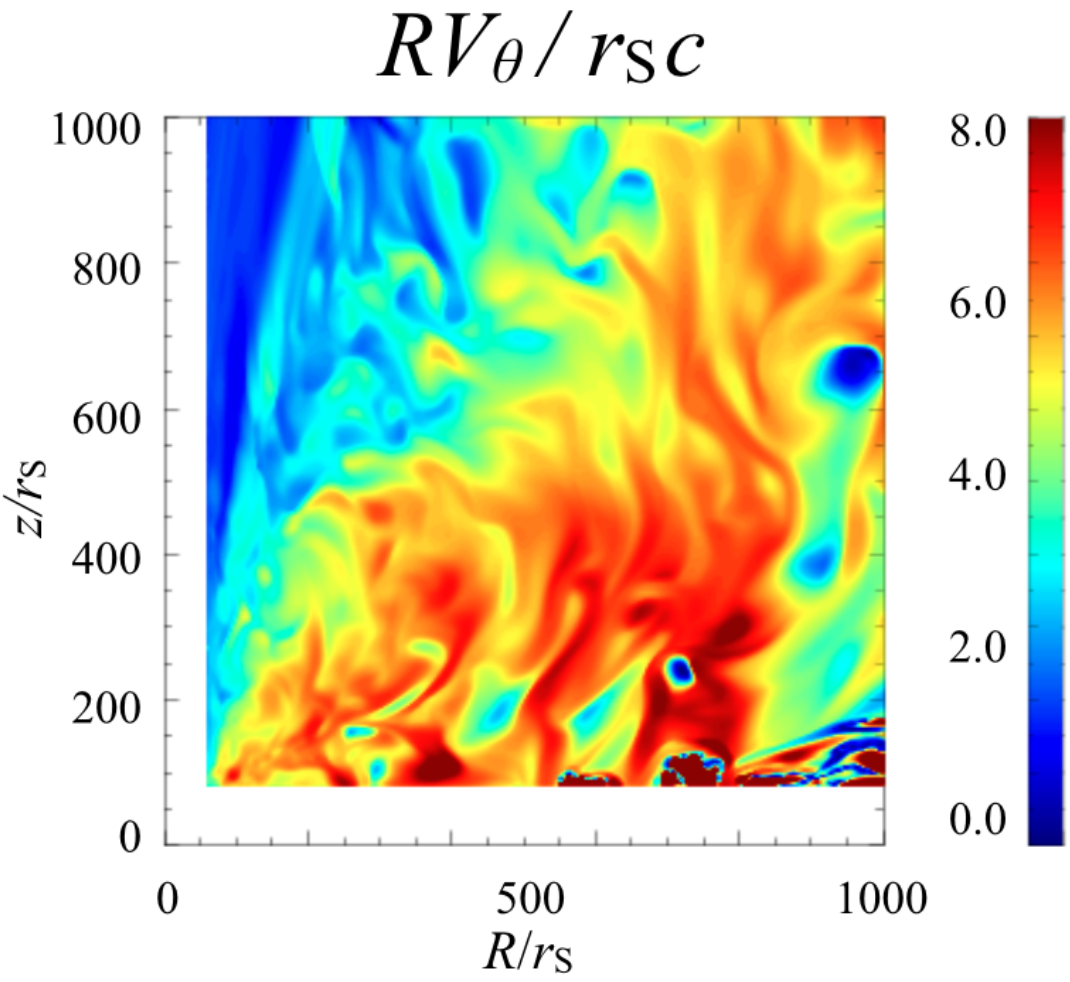

Figure 16: Verification of angular momentum preservation based on the RV_θ of the R-z plane at $\theta = 45°.0$ in the 3-D simulation results is shown. Here, R and V_θ are normalized by r_S and the speed of light c, respectively. The simulation parameters are the same as those in Figure 13.

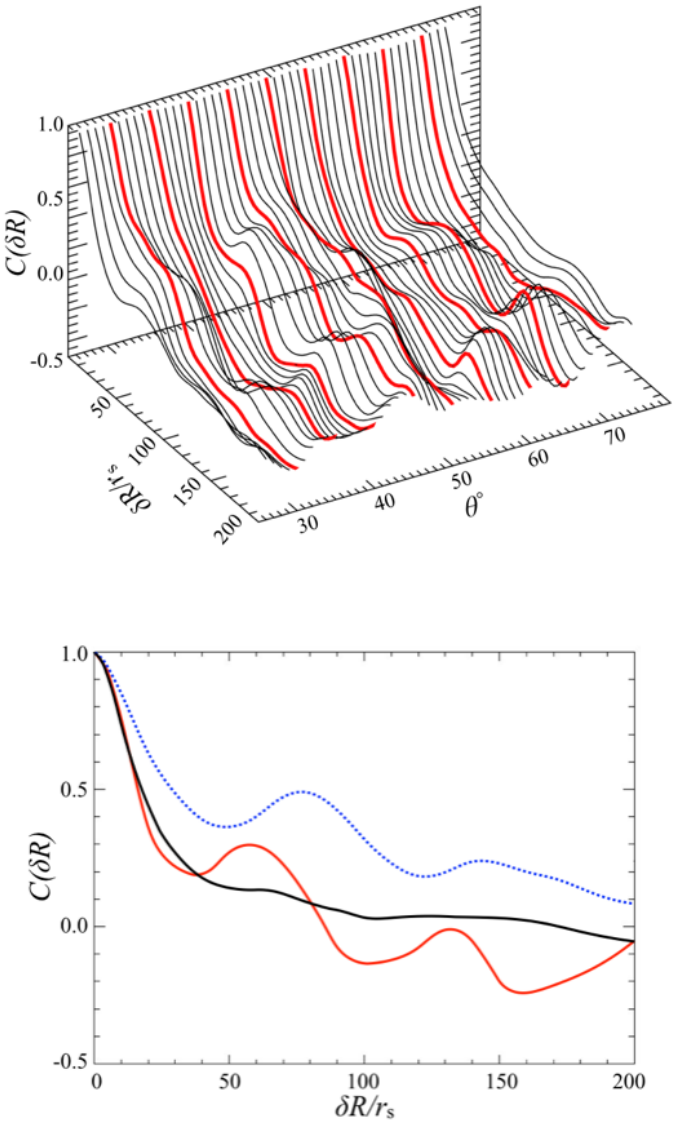

caption(Upper panel) Auto-correlation functions (ACFs) of the matter density distribution displayed in the lower left panel of Figure 13 as functions of δR at various azimuthal angles, θ. We indicate several lines in red for visual clarity. (Bottom panel) ACF as a function of δR at fixed $(\theta, z) = (45°.0, 600\ r_{\rm S})$ (red line), azimuthally averaged ACF (black line) obtained from the 3-D simulations, and the ACF as a function of δR at fixed $z = 600\ r_{\rm S}$ (blue dot line) obtained from the 2-D simulations.

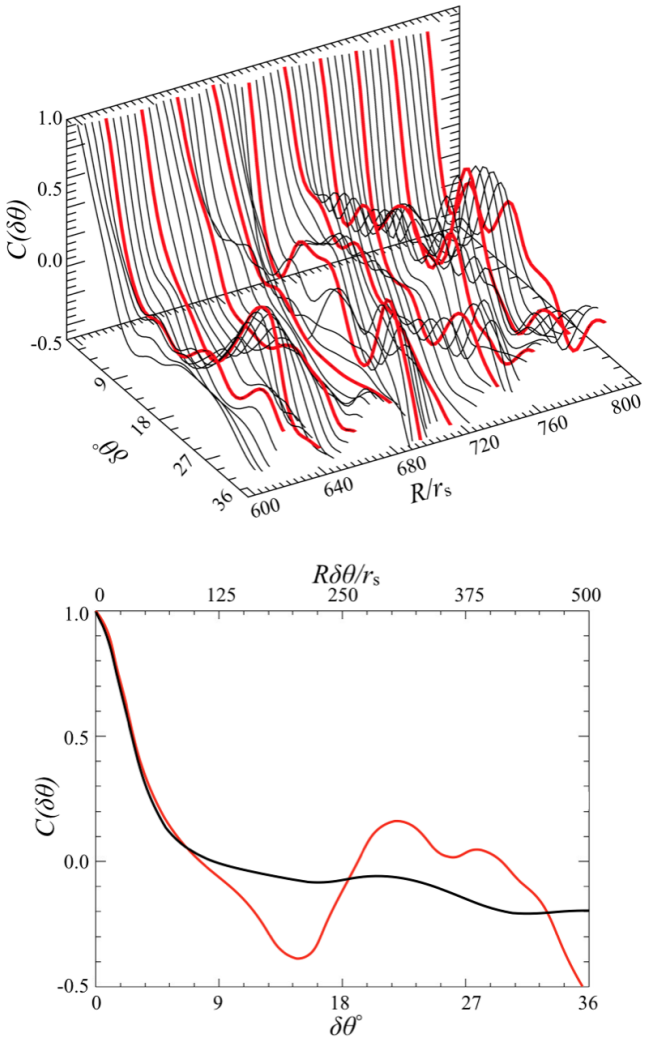

Figure 17: Auto-correlation functions (ACFs) of the matter density distribution displayed in the lower left panel of Figure 13 as functions of $\delta\theta$ at various horizontal directions, R. Some lines are indicated in red for visual clarity. In the bottom panels, the red line represents the ACF as a function of $\delta\theta$ at fixed $(R, z) = (740\ r_{\rm S}, 600\ r_{\rm S})$, while the black line represents the horizontally averaged ACF (black line) obtained from the 3-D simulations.

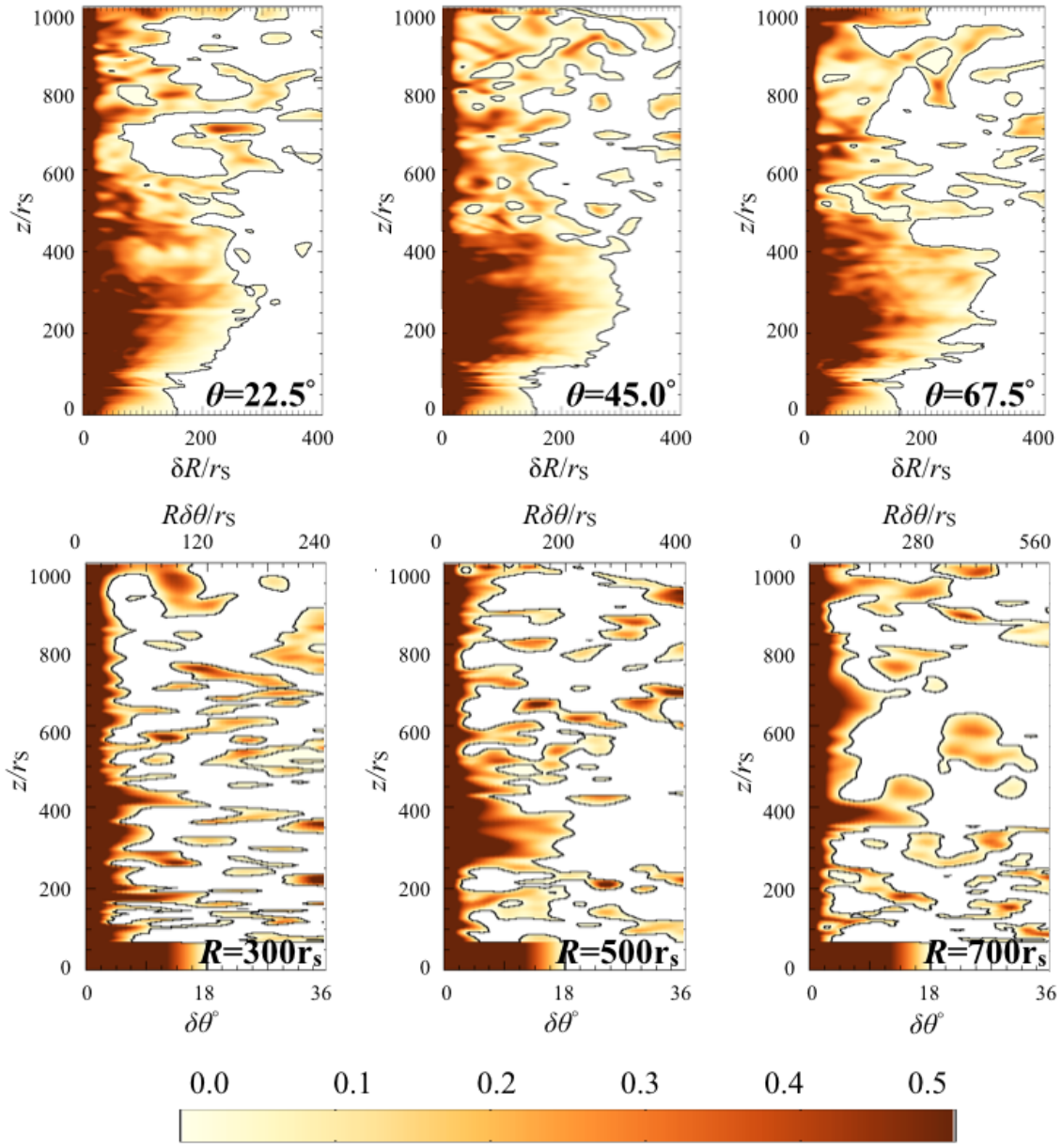

Figure 18: (Upper panels) Color contours showing ACFs in the R direction as a functions of z for three values of θ ($C(\delta R; z, \theta)$). Note that regions with white coloration indicate a negative ACF value. (Lower panels) ACFs in the azimuth direction as a functions of z for three values of R ($C(\delta\theta; R, z)$).

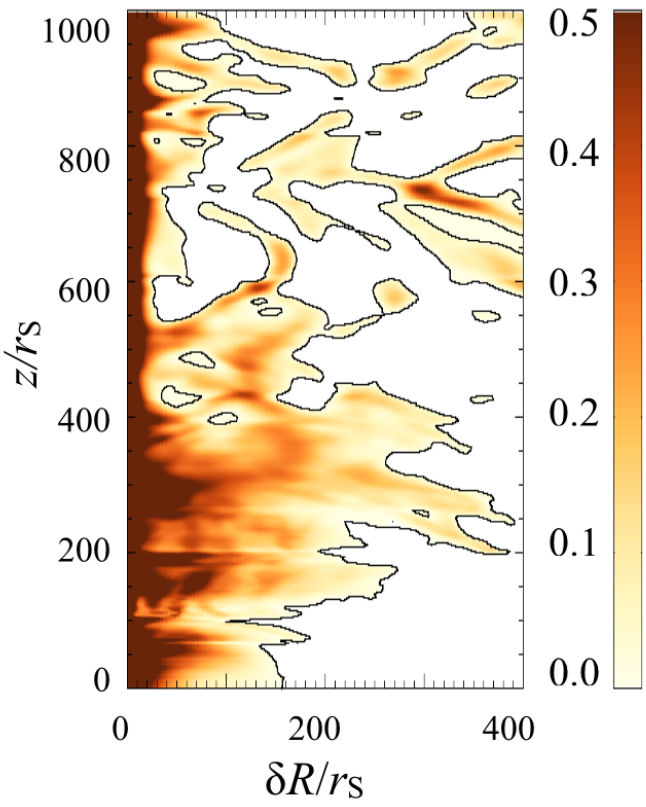

Figure 19: Color contours showing ACFs as functions of R and z for three representative values of ρ using 2-D simulation data. The horizontal and vertical axes are $\delta R/r_{\rm S}$ and $z/r_{\rm S}$, respectively.

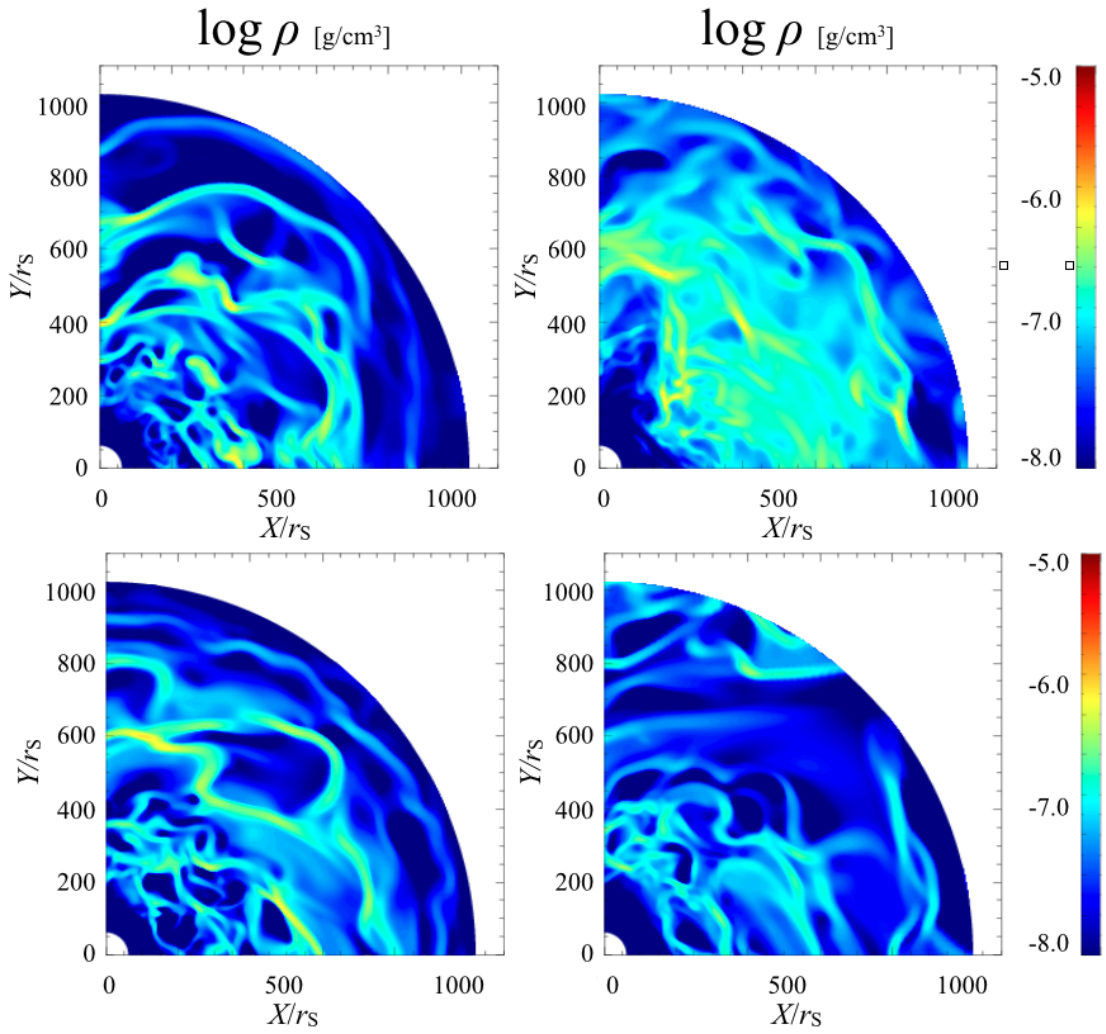

Figure 20: Comparison of results in the θ direction between models with different forms of initial perturbation. We plot cross-sectional views of the flow structure in the X-Y (or $R\cos\theta$-$R\sin\theta$) plane at $z = 700\ r_{\rm S}$ from 3-D simulations. The upper left and right panels, respectively, show color contours of the matter density of the model under perturbation by sinusoidal functions with amplitudes of 10% (P1) and 50% (P3). The lower left and right panels, respectively, show color contours of the matter density of the model under perturbations by random numbers of amplitudes of up to 10% (P2) and 50% (P4). The simulation parameters and elapsed time are the same as those in Figure 12.

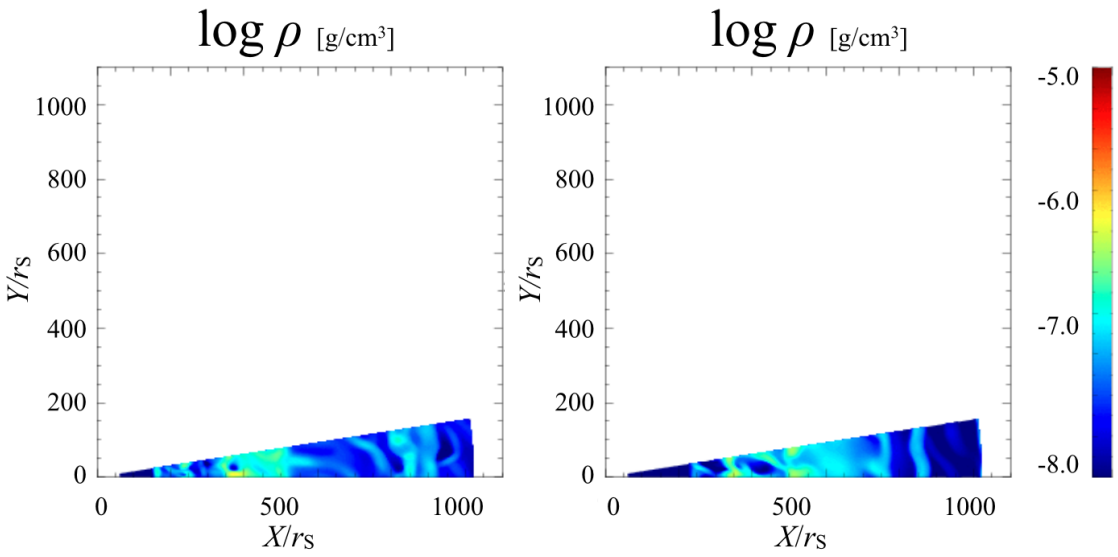

Figure 21: Comparison of density distributions of different models under different initial perturbations. The left and right panels show the resulting density structures in the horizontal plane at $z = 700\ r_{\rm S}$ for $4\theta = 9°.0$ (left panel) and $4°.5$, respectively.

Chapter 4 Observational Implications

In the previous chapters we demonstrated that the powerful outflow is a key signature of supercritical accretion and that this outflow has an intrinsically clumpy structure above the photosphere. In this chapter we discuss the observational implications. There are several classes of objects, in which clumpy outflow may be occurring. Good examples of these are ultra-luminous X-ray sources (ULXs), in which the clumpy outflow structure have been suggested by recent X-ray observations. Other candidates include the high-velocity, powerful outflow (the so-called ultra-fast outflow, UFO), which was discovered in the X-ray line absorption features of active galactic nuclei (AGNs). Based on the observations of emission lines in the optical band, the broad emission line regions (BLRs) in AGNs are thought to comprise numerous gas clouds. In this chapter, we argue that our model might account for these observational facts.

4.1 Comparison with Observations of ULXs

4.1.1 Overview of ULXs

ULXs are extremely luminous compact objects found in the off-nuclear regions of galaxies. Typically, point sources whose X-ray luminosity exceed 1×10^{39} ergs^{-1} are called ULXs, although several other thresholds are sometimes used. Thus, the luminosity of ULXs is higher than the Eddington luminosity of stellar mass black holes or neutron stars. Although ULXs exhibit these high luminosities, they are not located within galactic nuclei. Since the first detection of a ULX by the Einstein observatory (Long et al. [1981]; Fabbiano [1989]), the number of ULXs has dramatically increased. Recently, Swartz et al. [2011] identified 107 ULX candidates in nearby galaxies within 14.5 Mpc, while Walton et al. [2011] cataloged 470 ULX candidates in 238 nearby galaxies. Despite vigorous observation, the central objects of ULXs are poorly understood. There are two primary theoretical mechanisms for explaining the high luminosities of ULXs: intermediate-mass black holes (IMBHs) and supercritical accretion. The former hypothesis assumes the presence of IMBHs surrounded by sub-critical accretion disks (Colbert & Mushotzky [1999]; Makishima

et al. [2009]), as the Eddington luminosities are much larger than 10^{39} ergs^{-1} (note $L_{\rm E} \propto M_{\rm BH}$). In the latter hypothesis, however, high luminosities can be achieved, even if the central objects are stellar-mass black holes, as long as mass accretion occurs at a supercritical rate (e.g., King et al. [2001]; Watarai et al. [2001]). The discovery of pulsed emissions from ULXs was striking in this context (Bachetti et al. [2014]; Israel et al. [2017]), as pulsed emission points to the presence of a magnetized neutron star, thereby proving that supercritical accretion is actually taking place. One of the outstanding features of supercritical flows is the presence of powerful outflows accelerated by strong radiation forces, which is a very reasonable consequence in view of the notion of the Eddington limit; i.e., no supercritical spherical accretion is feasible owing to the strong radiation-pressure force, which inhibits accretion motion toward a central gravitational source. Numerical simulation of supercritical accretors was initiated by Eggum et al. [1988] and Okuda & Fujita [2000], but only recently has simulation of long-term evolution until the quasi-steady state become feasible. Such simulation studies were pioneered by Ohsuga et al. [2005], following which rather extensive simulations have been carried out by many groups (e.g., Sądowski et al. [2014]; McKinney et al. [2014]; Fragile et al. [2014]; Jiang et al. [2014]; Takahashi et al. [2016]), who have confirmed the ejection of radiative outflows. Outflow signatures are obtained by X-ray observations, and it is known that ULXs exhibit three different spectral states: a 'broadened disk state', a 'hard ultraluminous state' and a 'soft ultraluminous state' (Figure 22). Gladstone et al. [2009] proposed that the hard spectral component is caused by the Comptonization around the inner regions of the accretion disk, while the soft component originates from the photosphere at the bottom of radiatively driven winds. Such winds are suggestive of the outflow from a supercritical accretion disk (Poutanen et al. [2007]), as such disks induce outflow via the strong radiation pressure force. Indeed, the supercritical flow model can successfully reproduce the ULX spectra, which cannot be fit using simple thermal emission (e.g., Gladstone et al. [2009]). A similar idea was proposed from the theoretical point of view by Kawashima et al. [2009], who asserted that Comptonization occurs under powerful outflow (wind). Numerical simulations have revealed that hard X-rays are produced by Compton up-scattering in radiatively driven outflow from a supercritical disk (e.g., Kawashima et al. [2012]; Narayan et al. [2017]; Kitaki et al. [2017]).

Based on a detailed analysis of spectra, Middleton et al. [2014] argued that the

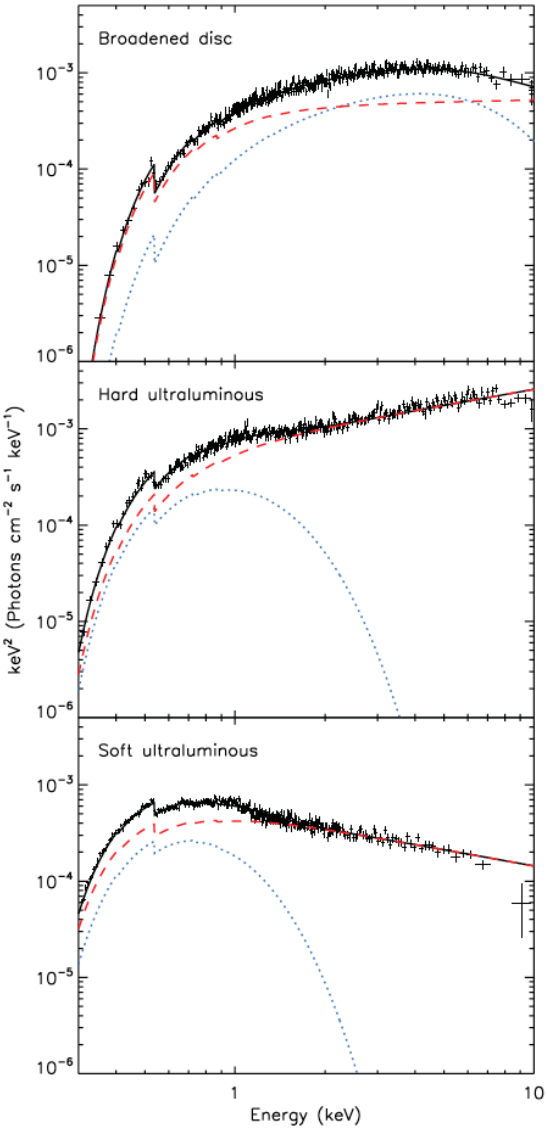

Figure 22: Three representative spectral states of ULXs: broadened disk (NGC 1313 X-2), hard ultraluminous (Ho IX X-1), and soft ultraluminous (NGC 5408 X-1) from top to bottom, respectively (Sutton et al. [2013]). Observational data are indicated by black crosses. The blue dotted lines indicate the absorbed multi-color disk blackbody spectrum, while the red dashed lines indicate the power-law spectrum.

low-energy line-like spectral residuals, which can be explained as resulting from the absorption of the partly ionized medium, indicate the emergence of outflows at speed of $\sim 0.2c$. More direct evidence for the existence of strong outflows is provided by the discovery of the blue-shifted X-ray absorption features in some ULXs. Pinto, Middleton & Fabian [2016] investigated the absorption line features of NGC 1313 X–1, and reported winds ejected toward the observer at a velocity of $0.2c$. The presence of mildly relativistic outflow ($\sim 0.2c$) is suggested by the detection of a strongly ionized Fe K absorption feature in NGC 1313 X-1 (Walton et al. [2016]).

4.1.2 Time Variation

An outflow with a clumpy structure will cause spectral variability as a result of floating gas clouds preferentially absorbing soft X-rays rather than hard X-rays. Alternatively, hard X-ray show larger variability if they are produced via Compton up-scattering by hot gas in gas clouds. Middleton et al. [2011] reported an X-ray spectral variability in the NGC 5408 X–1 ULX with variation timescale of several seconds and variation amplitudes that were larger in the hard X-ray bands. Based on observations such as these, they suggested that the outflow has a clumpy structure, as illustrated in the schematic in Figure 23. In this model, the outflow is launched from the supercritical accretion disk and fragments into many clumps (orange). Because the clumps pass across the observer's line of sight toward the central bright region (blue and green), the observed luminosity is should be temporarily reduced. This picture is very similar to our simulation results (see Figure 13), and here we compare our model results with the observed time variations. In our 3-D simulation, we see clumpy outflow structures above the photosphere at distances greater than

$$R_{\rm cl} \sim 10^3\, r_{\rm S} \sim 10^{9.5} \left(\frac{M_{\rm BH}}{10 M_\odot}\right) {\rm cm}. \tag{25}$$

From our ACF analysis of the 3-D data, we find that the clump length in the azimuthal direction is

$$\ell^\theta_{\rm cl} \sim 10^2\, r_{\rm S} \sim 10^{8.5} \left(\frac{M_{\rm BH}}{10 M_\odot}\right) {\rm cm}. \tag{26}$$

Caution is needed here, as this figure might be grossly underestimated; as we discuss in the final paragraph of subsection 3.2, the actual clumps appear to be much longer up to $\ell^\theta_{\rm cl} \sim 10^3\, r_{\rm S}$. This point requires further investigation, but here we continue to

use the value $10^2\ r_{\rm S}$ as a conservative limit. The clump velocities are on the order of $V_{\rm cl} \approx 0.3 V_{\rm K}$, with the Keplerian velocity numerically

$$V_{\rm K} = \sqrt{\frac{G M_{\rm BH} R_{\rm cl}^2}{r_{\rm cl}^3}} \simeq 10^{8.6} {\rm cm\ s^{-1}}, \tag{27}$$

where we use equation (19) and set $r_{\rm cl} \simeq \sqrt{2} R_{\rm cl}$ under the assumption of a viewing angle of 45 deg. We finally estimate the variation timescale to be

$$t_{\rm var} \sim \frac{\ell_{\rm cl}^{\theta}}{0.3 V_{\rm K}} \sim 2.5 \left(\frac{M_{\rm BH}}{10\ M_{\odot}} \right) \left(\frac{\ell_{\rm cl}^{\theta}}{10^2\ r_{\rm S}} \right) {\rm s}, \tag{28}$$

This allows us to make an important conclusion, namely, the variability timescale of $\sim$ 10 s necessitates a black hole mass on the order of several tends of $M_{\odot}$, although even a 10 $M_{\odot}$ black hole is acceptable, if the clump lengths are several hundreds of $r_{\rm S}$. This estimation might not be extremely accurate, however. We next attempt to estimate the variation timescale using the simulation data. This can be simply done by calculating the time variations of effective optical depth, $\tau_{\rm eff}$, defined as

$$\tau_{\rm eff} = \int_{300 r_{\rm S}}^{1000 r_{\rm S}} \sqrt{3(\kappa_{\rm es} + \kappa_{\rm ff}) \kappa_{\rm ff}} \rho dr. \tag{29}$$

Here, integration occurs from the outer boundary of the simulation box to the surface at $r = 300\ r_{\rm S}$, which corresponds to the photosphere on the time average. In Figure 24, we show the time variation of the effective optical depth (in the upper panel) and its relative variations with respect to the time-averaged one (in the lower panel). Here, we suppose that the variations of the effective optical depth could be a good indicator of flux variability, since absorption of radiation by floating clouds will produce spectral variability, as we discussed before. In making this figure we assume that the observer is at an infinite distance from the center in the directions of $\varphi = 30°$, $45°$, and $60°$ for a fixed $\theta = 45°$, where $\varphi \equiv \tan^{-1}(R/z)$ is the viewing angle. We see in the upper panel that the effective optical depth rapidly increases in the first 3 s but it settles down soon after in the certain values around $\tau_{\rm eff} = 0.1\ \ 1.0$, depending on the viewing angle. The larger the viewing angle is, the larger the averaged optical depth is, and $\tau_{\rm eff} \sim 1$ for $\varphi = 45°$ and $60°$ but ~ 0.1 for $\varphi = 30°$; that is, the density of the outflow is smaller near the rotation axis (see the middle-left panel in Figure 13). In any cases, we see the variation timescales are on the order of several seconds, which would imply that the aperiodic fluctuation of the luminosity will be observed on this

timescale. We also understand from the lower panel that the variation amplitudes would be $\sim 50 - 80$ %, depending on the viewing angle, since $|\Delta\tau_{\rm eff}| \sim 0.2 - 0.3$. Let us also estimate the time variations but using the electron scattering (Thomson) optical depth; namely,

$$\tau_{\rm es} = \int_{300r_{\rm S}}^{1000r_{\rm S}} \kappa_{\rm es}\rho dr. \tag{30}$$

Figure 25 shows the time evolution of $\tau_{\rm es}$ in the upper panel and its relative variations ($\Delta\tau_{\rm es}$) in the lower panel. This figure shows a similar tendency as that of Figure 24; i.e., the optical depth first rapidly grows and then settles down in certain values in 3 s. However, its absolute values differ significantly; the steady-state values are $\tau_{\rm es} \sim 300 - 600$, much larger than $\tau_{\rm eff} \sim 0.1 - 1.0$. This means that the outflows are very optically thick for the electron scattering, and the photons emitted from the photosphere should suffer multiple scattering before reaching a distant observer. It is also likely that those photons should suffer Compton up-scattering. The apparent luminosity might change via the scattering since the travel direction of the photons is altered. If this were the case, we estimate that the luminosity variation timescale would be several seconds, judging from the lower panel of Figure 25 that shows $\Delta\tau_{\rm es}$ fluctuations on several seconds. Although $|\Delta\tau_{\rm es}|$ is much larger than unity, the observed luminosity would not change drastically since the electron scattering does not change the number of photons. A part of photons would deviate from the line of sight, but other photons would turn in the direction towards the observer. If the Compton scattering occurs in the outflow, furthermore, the luminosity as well as the spectrum would change. We need 3-D radiation transfer calculation to make clear the point. The variation timescale, which we estimate here is much longer than that in T13. Their estimation was several days for the supermassive black hole of 10^8 $M_\odot$, or several hundredths of seconds for 10 $M_\odot$ black holes; i.e., two orders of magnitude shorter than our estimation. We find two main sources of discrepancy: (1) the clump length scale is systematically longer than the clump width, as was made clear in the present 3-D simulations, and (2) the rotation velocity is by some factor smaller than the local Keplerian value (Note that T13 estimated the timescale by assuming the Keplerian rotation). To sum up, our resulting timescale obtained by 3-D simulations is consistent with the variation timescale of a ULX estimated by Middleton et al. (2011). That is, the mass of the central objects of the ULX is, at most, on the order of several tens of $M_\odot$. We can safely conclude that the central objects should be

stellar-mass black holes.

4.2 Comparison with Observations of Other Objects

As discussed in the previous subsection, the outflow column density can be evaluated from the optical depth for electron scattering as $N_{\rm H} = \tau_{\rm es}/\sigma_{\rm T}$, and outflow velocity can be estimated to be around $0.1c$. Here, we further calculate two key parameters characterizing outflow clumps the photoionization parameter and the volume-filling factor to discuss the observational properties of clumpy outflow.

We first estimate the photoionization parameter, which is defined as

$$\xi = \frac{L_{\rm x}}{n_{\rm cl} r^2} \tag{31}$$

where $n_{\rm cl}$ is the (average) gas number density of the clumps, which is related to the (average) optical depth for Thomson scattering of the clumps through

$$\tau_{\rm cl} = n_{\rm cl} \sigma_{\rm T} \ell_{\rm cl}, \tag{32}$$

where $\ell_{\rm cl}$ is the average clump size; i.e., $\ell_{\rm cl} \sim \sqrt{\ell_{\rm cl}^r \ell_{\rm cl}^\theta}$. Then, the photoionization parameter can be estimated as

$$\xi \sim 10^3 \tau_{\rm cl}^{-1} \left(\frac{L_{\rm x}}{0.1 L_{\rm Edd}} \right) \left(\frac{\ell_{\rm cl}}{30\ r_{\rm S}} \right) \left(\frac{r}{10^3\ r_{\rm S}} \right)^{-2} {\rm erg\ cm\ s^{-1}}. \tag{33}$$

Equation (33) indicates that clumpy outflows are mildly ionized if $\ell_{\rm cl} \sim 30 r_{\rm S}$ (Kallman & McCray [1982]). It is important to note that the ionization parameter does not explicitly depend on the black hole mass, although the X-ray luminosity, $L_{\rm x}$, depends weakly on it, with $L_{\rm x} \sim L_{\rm bol}$ for Galactic sources (where $M_{\rm BH} \sim 10\ M_\odot$) and $L_{\rm x} \sim 0.1 L_{\rm bol}$ for AGNs (where $M_{\rm BH} \sim 10^8\ M_\odot$). Here, $L_{\rm bol}$ is the bolometric luminosity.

Such mildly ionized outflows are roughly consistent with the observations of X-ray absorption lines in AGNs. Tombesi et al. [2010] detected blue-shifted Fe K absorption lines from several AGNs whose bolometric luminosities have been estimated to be as high as the Eddington luminosity suggesting the existence of outflow with mildly relativistic velocities, called ultrafast outflows (UFOs), in the range $0.04 - 0.15c$. The ionization parameter of UFOs is estimated to be in the range $\xi \sim 10^{3-6}$ erg cm s^{-1} (Tombesi et al. [2011]). From Equation (33), clumpy outflows in AGNs have $\xi \sim 10^{3-6}$ erg cm s^{-1} at the region $r \leq 10^3\ r_{\rm S}$.for the case of the AGNs.

However, the column density is evaluated to be $N_{\rm H} \sim 10^{22} - 10^{24}$ cm^{-2} (Tombesi et al. [2011]), which is much smaller than that in our model. This discrepancy might be resolved for relatively small inclination angles (near face-on view), as the density tends to be small near the rotational axis (see Section 4.1.2). Alternatively, the outflowing matter might be metal-poor, in which case the column density would be underestimated. Although we focus on highly supercritical flows ($\dot{M}_{\rm acc} \sim 100 L_{\rm Edd}/c^2$) in this study, UFOs might be launched from a disk with a relatively small accretion rate. As the outflow rate would be reduced with a decreased accretion rate, outflow with a small column density might appear in the $\dot{M}_{\rm acc} \ll 100 L_{\rm Edd}/c^2$ case. In addition, for cases of near- or sub-critical flow, the radiation force owing to spectral lines not considered in the present simulation would act to accelerate the outflow (Proga et al. [2000]; Proga & Kallman [2004]; Nomura et al. [2016]). Indeed, Nomura & Ohsuga [2017] demonstrated that disk wind from a sub-critical disk closely fits the UFO observations (Gofford et al. [2015]).

We next estimate the volume-filling factor, which is defined as

$$\mathcal{F} = \frac{V_{\rm cl}}{4\pi r_{\rm out}^3/3}, \tag{34}$$

where $V_{\rm cl} (= M_{\rm cl}/n_{\rm cl} m_{\rm p})$ is the volume occupied by the clumps, $M_{\rm cl}$ the total mass of the clumps, and $r_{\rm out}$ is the size of the outflow region. As most of the mass in the outflow is contained in the clump, we find $M_{\rm cl} \sim \dot{M}_{\rm out}(r_{\rm out}/v_{\rm wind})$, where $\dot{M}_{\rm out}$ is the outflow rate and $v_{\rm wind}$ is the radial wind velocity. As $n_{\rm cl}$ is given by Equation (32), we can obtain the filling factor as

$$\mathcal{F} \sim 4.5 \times 10^{-3} \tau_{\rm cl}^{-1} \left(\frac{\dot{M}_{\rm out}}{10 L_{\rm Edd}/c^2} \right) \left(\frac{v_{\rm wind}}{0.1c} \right)^{-1} \left(\frac{\ell_{\rm cl}}{30\ r_{\rm S}} \right) \left(\frac{r_{\rm out}}{10^3\ r_{\rm S}} \right)^{-2}. \tag{35}$$

This is consistent with the filling factor estimated by T13, as our outflow rate, wind velocity, and clump size are similar to those in that model. The volume filling factor is independent of the black hole mass because $\dot{M}_{\rm out} \propto M_{\rm BH}$, $\ell_{\rm cl} (\propto n_{\rm cl}^{-1}) \propto M_{\rm BH}$, and $r_{\rm out} \propto M_{\rm BH}$. Thus, our results are applicable to AGNs, even though we employed 10 $M_\odot$ black hole in the simulation. If we assume $r_{\rm out} \sim 10^5\ r_{\rm S}$, the filling factor becomes approximately 4.5×10^{-7}, which is roughly consistent with the observations of the BLR clouds of AGNs at around $r \sim 1$ pc ($\sim 10^5\ r_{\rm S}$ for $M_{\rm BH} \sim 10^8\ M_\odot$; Peterson [1997]).

However, a problems remains in that the outflow velocity is too high to reproduce the broad emission lines observed in AGNs. The velocity of the clouds in the BLRs is believed to be a few or several thousand $\mathrm{km\,s^{-1}}$ (Peterson et al. [2004]; Collin et al. [2006]), which is significantly smaller than that of our clumpy outflows, $0.1c$. Thus, the clumpy outflow needs to be decelerated to resolve this discrepancy. As the outflow velocity is much higher than the escape velocity, the gravity of the black hole does not work effectively. One of the more likely mechanisms would be interaction between the clumpy wind and interstellar matter, which would slow the outflow via collision with the low-speed medium. Further quantitative analysis of this will left as future work.

4.2.1 Narrow-Line Seyfert 1 Galaxies

The clumpy outflow model can also be applied to Narrow-Line Seyfert 1 galaxies (NLS1s). Done & Jin [2015] and Jin et al. [2016] studied three NLS1s 1H 0707-495, PG 1244+026, and RX J0439.6-5311 in detail and estimated their black hole masses to be approximately $10^{6-7}\,M_{\odot}$. These NLS1s exhibit luminosities and spectral energy distributions (SEDs) characteristic of the optical/UV band. Optical/UV emission of this type is believed to originate from the regions distant from the central black holes, in which standard disks are formed; thus, the mass accretion rate can be estimated by comparing the optical/UV SED inferred from the standard disk model with the observed optical/UV SED. The resulting mass accretion rate significantly exceeds the critical accretion rate, making these NLS1s candidate objects for supercritical accretion flow.

When its mass accretion rate exceeds the critical accretion rate, supercritical accretion flow (slim disk) appears near a black hole, although a standard disk will still form on the outside of the supercritical flow region. In supercritical accretion flow, the radiation efficiency is reduced as a result of the advection of radiation energy and the emergence of radiatively-driven outflow. Therefore, the disk luminosity is reduced relative to a case in which the entire disk is a standard disk. This is consistent with the observations by Done & Jin [2015]. Figure. 26 shows the SEDs of NLS1 a) 1H0707-495 and b) PG 1244+026 (Figure. 2 of Done & Jin [2015]). In these figures, the squares indicate observational data in the Optical/UV region, while cross marks indicate data from X-ray observations. The SEDs calculated using the standard disk model around

black holes with masses of 2×10^6 $M_\odot$ and 10^7 $M_\odot$ are indicated as solid and dashed lines, respectively. The spin parameters of the black holes are assumed to be 0.998 (red), 0.9 (blue), 0 (green). In both panels, it is seen that the SED of the standard disk model significantly exceeds the observational value in the X-ray region; in other words, the radiation efficiency near the black hole is lower than that of the standard disk. This is the evidence that a supercritical accretion disk has formed around the black hole. Figure. 27 shows the SEDs of the three NLS1s discussed in this paper (Figure. 10 of Jin et al. [2017]). Although RX J0439.6-5311 (red) is slightly brighter than PG 1244+026 (blue), it is seen that the SEDs of these two objects are very similar. Although 1H 0707-495 does not conflict with the other two objects in the optical/UV region, its X-ray luminosity occasionally decreases significantly. Indeed, inspection of the black crosses reveals that the SED of the brightest state roughly agrees with that of PG 1244+026, while the SED of the other two states are much darker than those of RX J0439.6-5311 and PG 1244+026 (see also Figure 26).

This X-ray extinction can be explained by clumpy outflow blowing away the radiation force from the supercritical disk around the black hole. When clumps obscure the observer 's line of sight, X-ray extinction occurs. Although clumpy outflow is present in RX J0439.6-5311 and PG 1244+026, no reduction in the X-ray luminosity occurs as a result of the clumpy outflow, as these objects are seen close to face-on.

This clumpy outflow model is supported by Hagino et al. [2016], who calculated SEDs including emission and absorption lines based on the model and closely reproduced the complicated absorption line structure seen in 1H 0707-495. In addition, in RX J0439.6-5311 has blue-shifted components in both the narrow line region (NLR) and BLR. This is consistent with the hypothesis that the gas is accelerated by the strong radiation force (exceeding the gravitational force) from the supercritical accretion disk around the black hole.

As mentioned above, the possibility of clumpy outflow in NLS1s has been previously mooted. However, the 200s time scale of X-ray variability observed at 1H 0707-495 (Done & Jin [2015]) is not consistent with our clumpy outflow model. From Equation 28, as assumed black hole mass of 10^6 $M_\odot$ corresponds in our simulations to a timescale of 2.5×10^5 s, which is 1000 times larger than the observed value. This inconsistency might be resolved through the acceleration of matter by radiation force indicated by spectral lines corresponding to the absorption of UV radiation through

the bound-bound transition of metals (Proga et al. [2000]; [2004], Nomura et al. [2016]; [2017]), which would lead to the formation of disk winds. The opacity of the spectral lines can be much larger than that of the electron scattering and, because the outflow tends to fragment into clouds with optical depths of about one, the size of clumps would be sufficiently smaller in the above case of line-driven wind. Reduction of the clump size to a factor of about 1/1000 might in this manner explain the variation timescale of the observations; however confirmation of this will require a much higher resolution simulation than was used in this study and will be left as future work. This is left as a future work.

4.2.2 Black Hole X-Ray Binaries

Line spectrum fluctuation in the outburst phase of V404 Cyg, a black hole X-ray binaries (close binary system including BH; BHBs), can potentially be explained as resulting from clumpy outflow from a supercritical accretion flow. V404 Cyg is known to be a low-mass X-ray binary ($mass function = 6.26\ M_{\odot}$). Motta et al. [2017] examined the spectrum of the outburst phase of V404 Cyg in detail and, found a most common flux of $\sim 3 \times 10^{-8}\ ergcm^{-2}s^{-1}$. Conversion of this flux to the bolometric X-ray luminosity produces a figure of about 4% of the Eddington luminosity of V404 Cyg. However, the radiation flux can increase up to 1.22×10^{-6} $ergcm^{-2}s^{-1}$ (with the corresponding bolometric luminosity increasing to about twice the Eddington luminosity) and the flux has been shown to exceed the Eddington luminosity over 3% of its observed period.

The observation also revealed that the radiation spectrum violently changes on a time scale of several tens of seconds. According to spectral fitting, the dense of which, the covering fraction is about 0.8 obscure the inner part of the accretion disks. Furthermore, the blue-shifting in the absorption lines indicate an outflow velocity of about 0.1 c or less. These observational properties are roughly in agreement with the clumpy outflow obtained in our simulations. In our simulations, the outflow velocity was about 10% of the speed of light. In addition, as many clumps are blown away at wide angles except in the direction of rotation axis (about 20° or less), the covering fraction is expected to be close to 1.0 for observers not oriented face-on. The observations reported a variation timescale of V404 Cyg of probably less than tens of seconds, which is also consistent with our results of a few seconds for a black hole

with 10 $M_{\odot}$ Calculation of the SEDs and direct comparison with observations will be important future work.

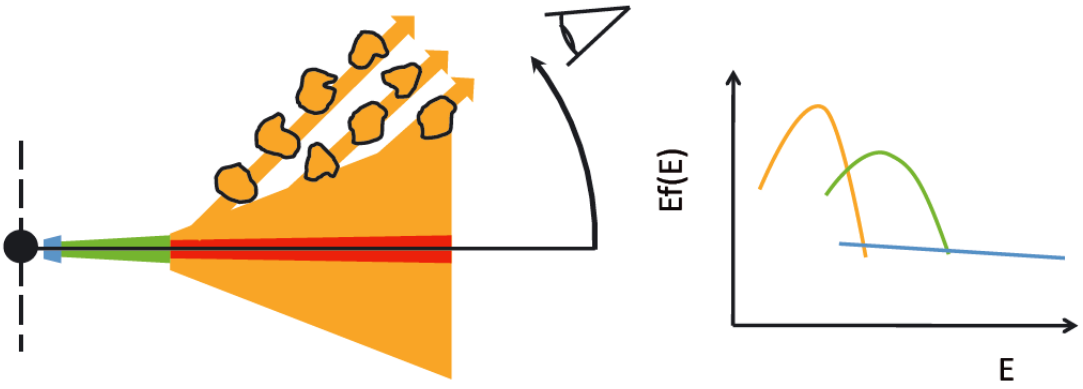

Figure 23: Clumpy outflow model suggested by Middleton et al. [2011]. The blue region produces the power-law component of the spectrum, with optically thick Comptonization occurring in the green region. The radiatively-driven outflow is launched from the disk surface and fragments into many clumps (orange). In this model, ULXs are observed as highly variable objects by edge-on observers as the clumps pass across the observer's line of sight and obscure central regions. By contrast, variability is suppressed for face-on observers.

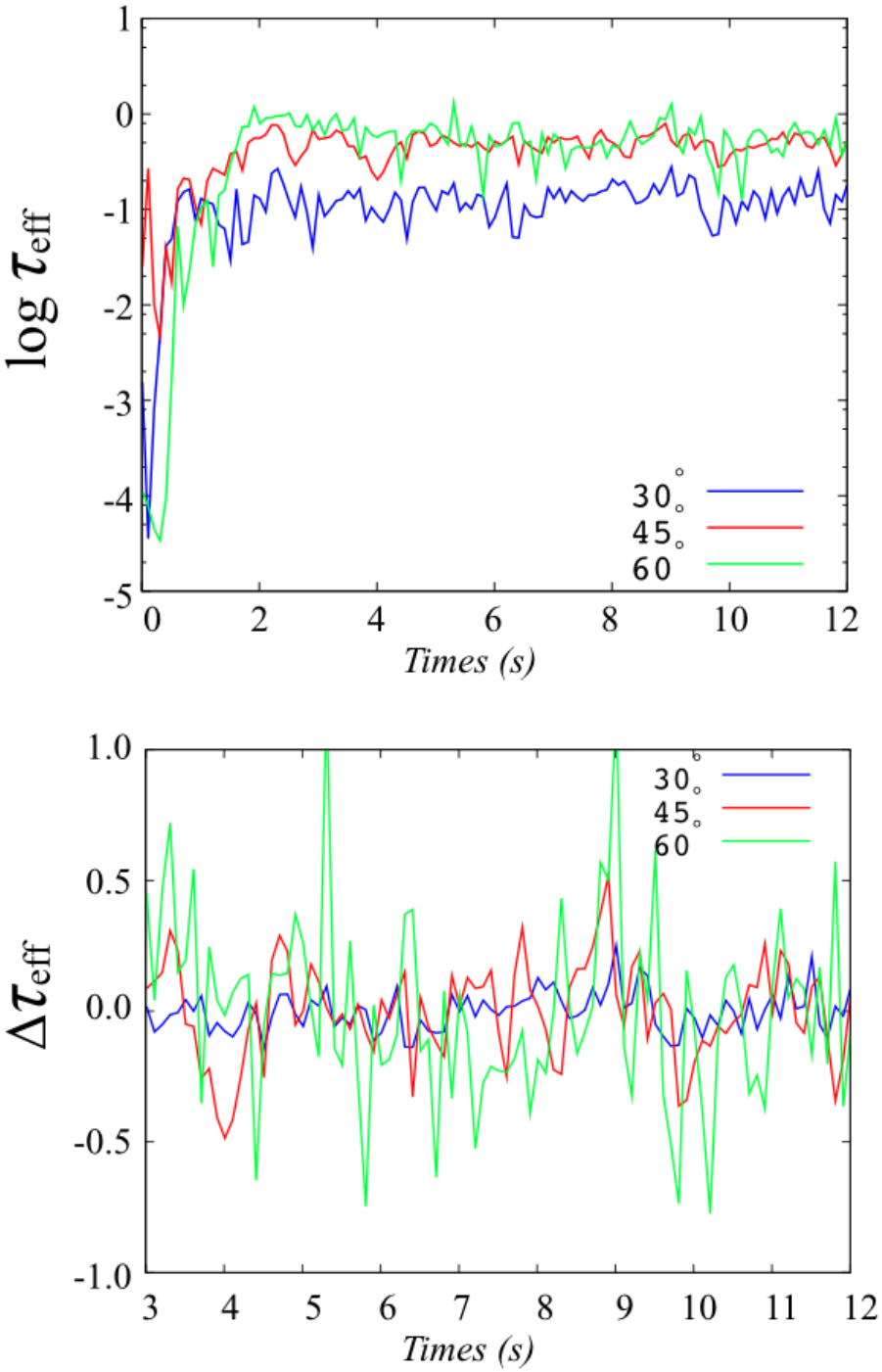

Figure 24: Time variations in effective optical depth at a variety of angles measured by a distant observer ($\varphi = 30°, 45°$, and $60°$ for a fixed $\theta = 45°$).

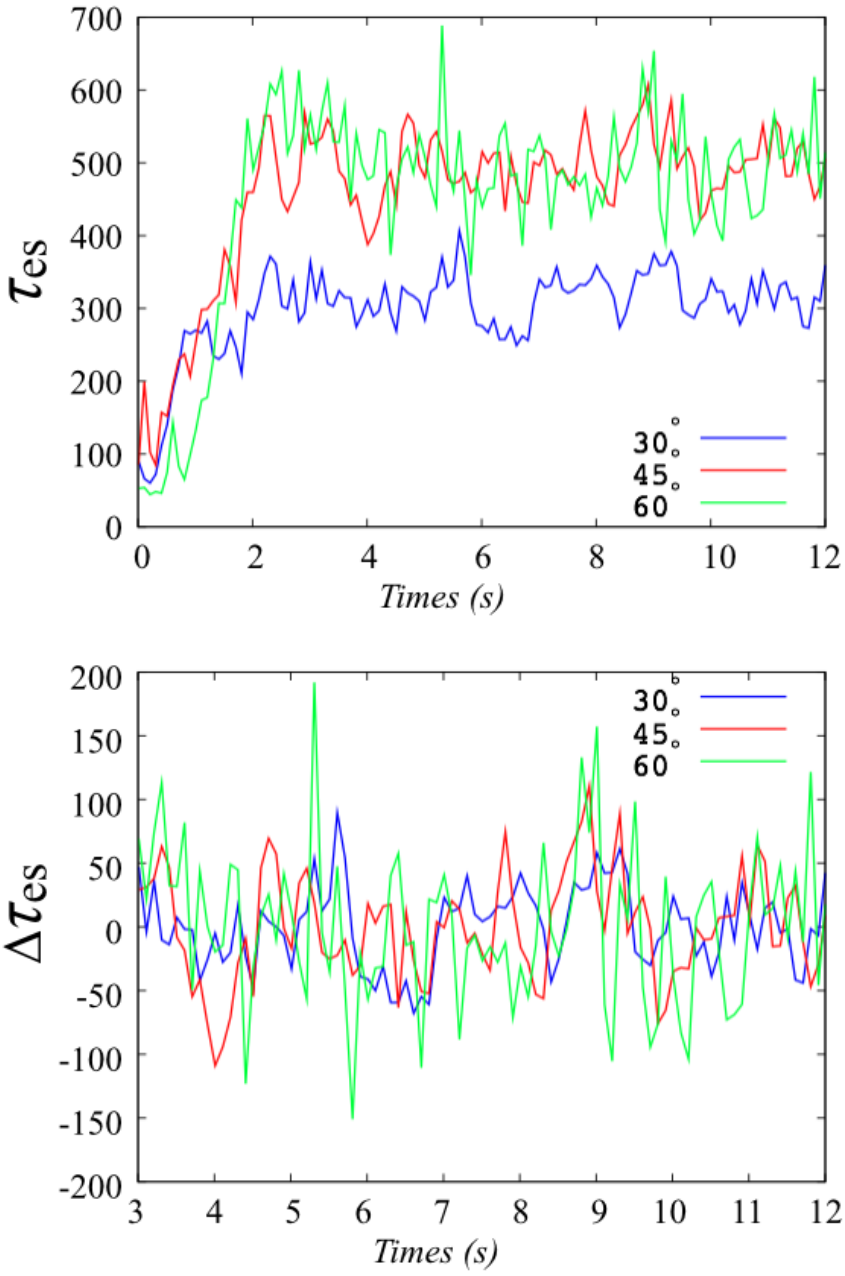

Figure 25: Same as Figure 24 but for the Thomson optical depth.

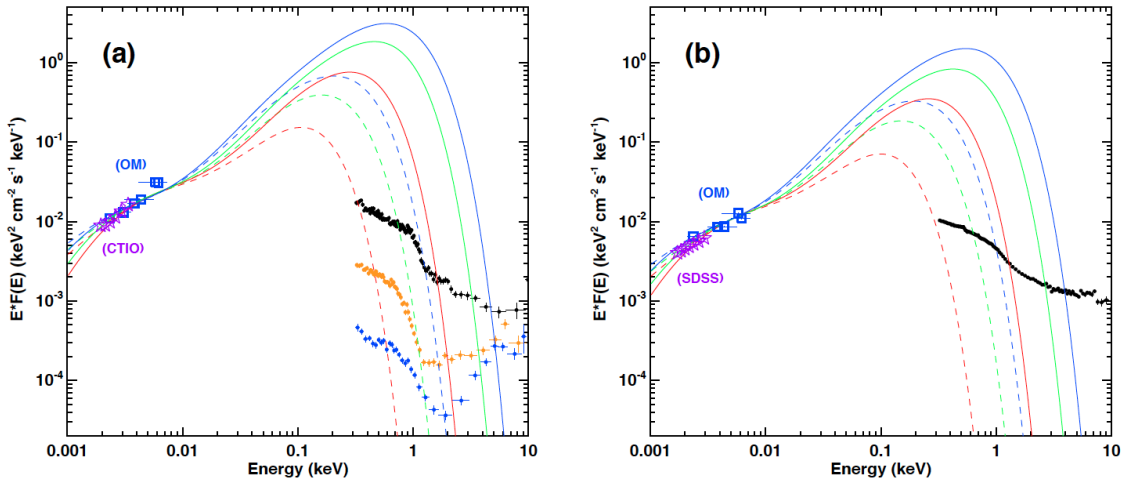

Figure 26: SEDs of NLS1s a) 1H0707-495 and b) PG 1244+026 with continuum fitting of optical continuum (star symbols), with optical/UV (squares) and X-ray (cross marks) observational data. The lines indicate the SED of the standard disk model around black holes of mass $2 \times 10^6\ M_\odot$ (solid) and $10^7\ M_\odot$ (dashed). The spin parameters of the black holes are assumed to be 0.998 (red), 0.9 (blue), and 0 (green).

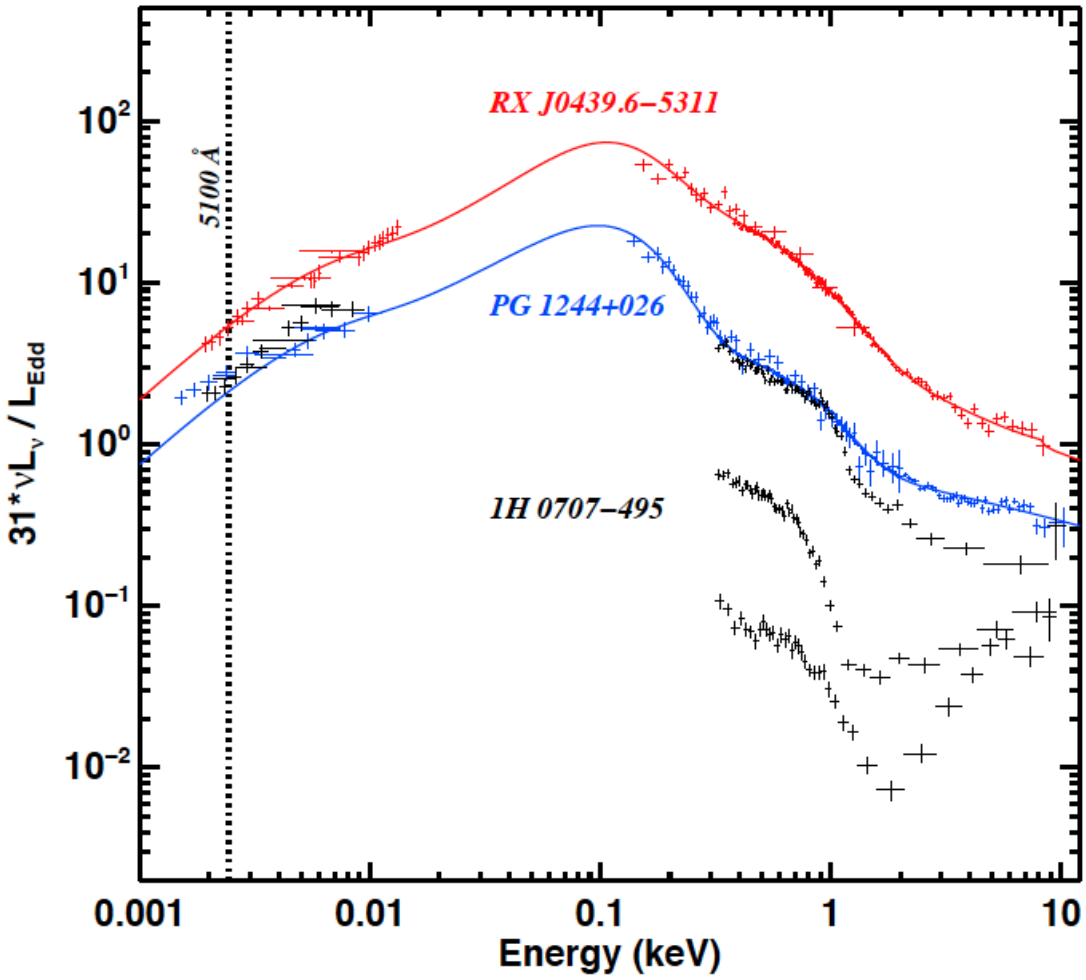

Figure 27: SEDs of RX J0439.6-5311 (red), PG 1244+026 (blue) and 1H 0707-495 (black). Although the SED of 1H 0707-495 roughly agrees with those of the other two objects in the optical/UV region, its X-ray luminosity of occasionally decreases significantly.

Chapter 5 Summary

This thesis reports on the first-ever successful 3-D RHD simulations of outflow from an underlying supercritical accretion flow at an accretion rate of $\sim 10^2 L_{\rm Edd}/c^2$. To focus our study on the clumpy structure of the outflow, we used a large computational box ($\sim 10^3\ r_{\rm S}$), although the regions at $R < 60\ r_{\rm S}$ and/or $z < 80\ r_{\rm S}$ were excluded from the 3-D simulation to reduce the computational cost. We solved the full set of radiation hydrodynamics equations, taking terms up to an order of (v/c). Radiation fields were evaluated by adopting the M1-closure method to ensure the conservation of total energy and momentum of the radiation and fluid. We indicated our 3-D simulations using the axisymmetric 2-D simulation data in a nearly steady state but with azimuthal perturbations added. From this, we discovered the following new features of clumpy outflow:

1. The outflow is accelerated outward by the radiation force and fragments into many clumps that form a pattern similar to that of a torn sheet; i.e., the clumps are more elongated in the azimuthal direction than in the radial direction (see also item 3 below).

2. These clumps rotate around the central black hole with sub-Keplerian velocity at a distance of $\sim 10^3\ r_{\rm S}$ from the center. This occurs in part because the gas is being blown away while retaining its angular momentum and in part because the radiation force in the azimuthal direction is too small to change the angular momentum.

3. From the auto-correlation function analysis, we found a typical clump size of 30 $r_{\rm S}$ or less in the radial direction with additional elongation in the angular direction of up to hundreds of $r_{\rm S}$ (future higher-resolution study will be needed to precisely determine the 3-D shapes of the clumps, as the present simulation suffered from limited numerical resolution). Although the clumpy structure in the R-z plane is similar for the 2-D and 3-D simulations, a prominent 3-D feature

that does not significantly depend on the initial perturbation was revealed for the first time by these simulations.

4. Stochastic time variation in the luminosity is expected to occur when clumps pass across the line of sight of a distant observer. Using the typical clump size and rotational velocity, the variation timescales are estimated to be several seconds for a black hole with a mass ranging from ten to several tens of $M_\odot$. This was confirmed by calculation of the time variations of the effective optical depth above the photosphere, which is located at a few hundreds of $r_{\rm S}$ from the central black hole.

5. The estimated timescale agrees roughly with observations of some ULXs. Our results therefore provide strong support to the hypothesis that ULXs are powered by supercritical accretion onto stellar mass black hole.

6. Although the mass of the black hole in the simulations was set at 10 $M_\odot$, we have good reason to believe that the outflow velocity, photoionization parameter, and volume filling factor are independent of the black hole mass. We accordingly suggest that our clumpy outflow model can partially explain observational features of UFOs and BLRs in AGNs.

We summarize future works. By the present study, the size of typical clumps in the θ and R direction were different. The radiation force may be the cause that the gas cloud has been extended in θ direction. Since the gas cloud is optically thick, the radiation is attenuated at the outer surface of it (the side far from the BH), and the radiation force is hard to work. In contrast, the outward radiation force is relatively strong at the inner surface. As a result, the gas cloud is effectively compressed in the R direction. On the other hand, the gas cloud may be stretched in θ direction also due to the effect of differential rotation. In order to clarify the reason why the clump is lengthened in θ direction, it is necessary to accurately evaluate the radiation fields by solving the radiation transfer rather than the approximation as in our work, and it is also important to increase the resolution of the simulation.

Furthermore, the temperature of the gas in the clump is $\sim 10^{7-8}$ K, so at this temperature heavy elements are not completely ionized via the collision and bound-free absorption may work, so bound-free opacity should be considered in the future.

In Ohsuga et al. [2005], simulations including bound-free opacity were carried out, showing the result that opacity slightly changes the mass accretion rate and disk luminosity. In recent years, it is known that outflow is blown away even by the line force (Proga et al. [2000], Nomura et al. [2016]). In our work, we focused on the radiation force due to electron scattering, but simulation considering both line force and electron scattering will be necessary in future.

Finally, in order to compare with more directly, it is considered that Monte Carlo radiation spectrum calculations (Kawashima et al. [2012], Kitaki et al. [2017]) based on the data of this research are the most important task.

Appendix A Setting of Computational Domain

In order to clarify the outflow properties, large box simulations with good spatial resolution are required. However, the numerical cost of the such 3-D simulations is too expensive to perform. The reasons are as follows. The timestep of the simulation is proportional to the minimum of the grid spacing ($\Delta x_{\rm min}$), $\Delta t \propto \Delta x_{\rm min}$. For the 2-D simulations with cylindrical coordinates, (R, z), $\Delta x_{\rm min}$ becomes the minimum of the mesh size in the R- or z-directions. In the case of T13, we have $\Delta x_{\rm min} = \Delta R$ because of $\Delta R = \Delta z =$ constant. Therefore, the simulation timestep does not depend on the computational domain. Even if the large simulation box is employed with keeping the resolution, the time step does not change although the computation quantity ($Q_{\rm c}$) increases as an increase of the number of grids,

$$Q_{\rm c} \propto \frac{N_R N_z}{\Delta R}, \tag{36}$$

where N_R and N_z are the number of grids in R- and z-directions.

Such situation changes drastically for 3-D simulations. In the 3-D simulations with cylindrical coordinates, (R, θ, z), the grid spacing in θ-direction ($R\Delta\theta$) is of great importance, since $R\Delta\theta$ decreases as approaching the rotation axis ($R = 0$). Indeed, we set $\Delta R(= \Delta z)$ and $\Delta\theta$ to be constant in the present work, the grid spacing in the θ-direction ($R\Delta\theta$) tends to be smaller than ΔR at the inner region. If $R\Delta\theta$ equals to ΔR at a certain radius, $R_{\rm c}$, the grid spacing in the θ-direction becomes equal to $\Delta R(R_{\rm in}/R_{\rm c})$ at the inner boundary ($R = R_{\rm in}$). Thus, the computation quantity ($Q_{\rm c}$) is

$$Q_{\rm c} \propto \frac{N_R N_\theta N_z}{\Delta R}\frac{R_{\rm c}}{R_{\rm in}}, \tag{37}$$

which is $N_\theta R_{\rm c}/R_{\rm in}$ times larger than that for 2-D simulations (see equation (36)).

We have to employ larger $R_{\rm in}$ for reduction of the numerical cost, since we cannot drastically reduce N_θ and $R_{\rm c}$ in order to resolve the clumpy structure in the θ-direction. Thus, in the present study, we exclude the inner region by setting $R_{\rm in} = 60\ r_{\rm S}$. Specifically, we employ the fixed inner boundary at $R = 60\ r_{\rm S}$ where we

keep the same values (2-D simulation data) for the physical quantities at any times later on in the 3-D simulation.

Here we note that the value of 60 $r_{\rm S}$ is an optimum value. If we set $R_{\rm in}$ to be much larger than 60 $r_{\rm S}$, we cannot accurately investigate the clumpy outflow and the outflow motion changes. Figure 28 shows the density distributions (left panels) and poloidal velocities (right panels) of the 2-D simulations for $R_{\rm in} = 60\ r_{\rm S}$ (top) and 80 $r_{\rm S}$ (bottom). Here the radius of the outer boundary is $10^3\ r_{\rm S}$, and the range of the computational box in z-direction is $80\ r_{\rm S} \leq z \leq 10^3\ r_{\rm S}$. In the right panels, we can recognize clumpy structure at $z \geq$ several hundreds of $r_{\rm S}$ in both cases. However, the right panels indicate that the outflow velocity is smaller for $R_{\rm in} = 80\ r_{\rm S}$ than $R_{\rm in} = 60\ r_{\rm S}$. Although the outflow velocity of $\sim 0.1c$ for the case of $R_{\rm in} = 60\ r_{\rm S}$ is consistent with the full domain simulations, the velocity is around $0.05c$ in the case of $R_{\rm in} = 80\ r_{\rm S}$. This means that the radiation force plays an important role for acceleration the clumpy outflow around $60 - 80\ r_{\rm S}$. If we employ even larger $R_{\rm in}(> 80\ r_{\rm S})$, not only the velocity fields but also the density structure deviates from the results of whole domain simulations.

On the other hand, if we set $R_{\rm in}$ to be much smaller than $60 r_{\rm S}$, the numerical cost becomes too expensive. Thus, we employ $R_{\rm in} = 60 r_{\rm S}$ in the present simulations. In addition, in order to reduce the numerical cost even slightly, the regions near the equatorial plane ($\leq 80 r_{\rm S}$) are excluded.

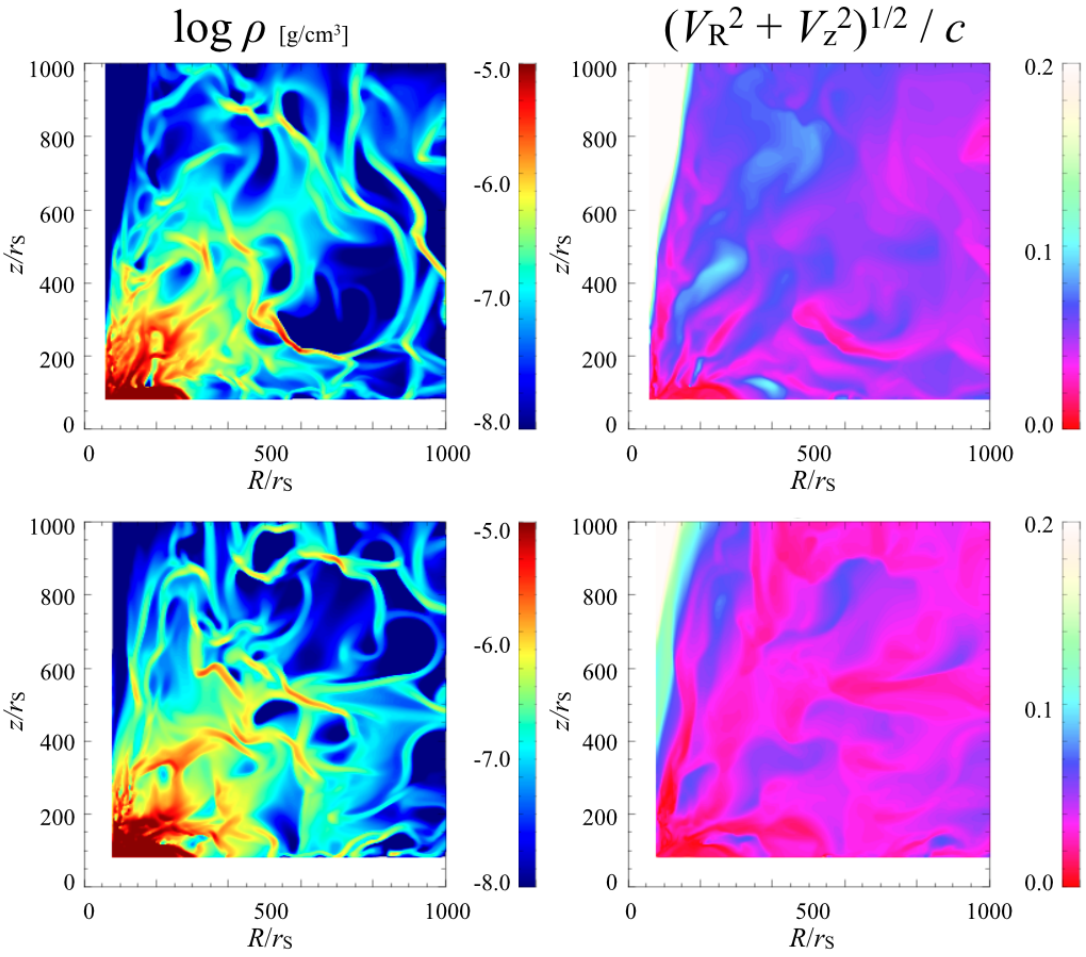

Figure 28: Density distributions (left panels) and poloidal velocities (right panels) of the 2-D simulations with different calculation domain at the elapsed time $t = 5$ s. The computational domain of the upper panels is $60 \leq R/r_{\rm S} \leq 10^3$, $80 \leq z/r_{\rm S} \leq 10^3$, and of the lower panels is $80 \leq R/r_{\rm S} \leq 10^3$, $80 \leq z/r_{\rm S} \leq 10^3$.

Appendix B Resolution Dependence

In the present work, we show that the typical radial and azimuthal clump size are $\ell_{\rm cl}^{r}/2 \sim 15\ r_{\rm S}$ and $\ell_{\rm cl}^{\theta}/2 \sim 10^2\ r_{\rm S}$, respectively. However, the radial clump size is different from the typical clump size obtained by T13, $\sim 10\ r_{\rm S}$. The reason for this may be the difference in resolution of the simulations. Therefore, we perform further three 3-D RHD simulations with different resolution. The resolution of each model is shown in Table 2, where model B is a fiducial model shown in the main text.

2-D cross-sectional views of density (left panels), temperature ratio (middle panels), and velocity fields (right panels) are shown in Figures 29 (model A) and 30 (model C). The upper and lower panels indicate the $R-z$ plane and the $X-Y$ plane (constant z plane), respectively. As with the model B (see Figure 13), we can recognize clumpy density structure on the R-z plane at $z \geq$ several hundreds of $r_{\rm S}$ in the models A and C. However, the width of each clump in the radial direction seems to be thinner as the resolution is higher. As shown the lower left panels of Figures 13, 29, and 30, we can find clumpy density structure in azimuthal direction. The difference in thinness of clumps in azimuthal direction is not clear. The typical clump size in radial and azimuthal directions will be discussed later using ACFs. It is found that the temperature ratio is low in the high-density region and vice versa. Such tendency is found in models A, B, C, and 2-D simulation. We find in the right panels that the outflow velocity exceeds the escape velocity at around $z > 400\ r_{\rm S}$. We can see that $V_\theta/V_{\rm K}$ tends to decrease with an increase of R, since the matter is

Table 2: The resolution and the typical clump size of each model

Model	$\Delta R[r_{\rm S}]$	$\Delta\theta[^\circ]$	$\Delta z[r_{\rm S}]$	$\ell_{\rm cl}^{R}/2\ [r_{\rm S}]$	$\ell_{\rm cl}^{\theta}/2\ [^\circ]$
A	8.0	0.9	8.0	28.0	4.0
B	4.0	0.9	4.0	15.0	3.0
C	2.0	0.9	2.0	10.0	2.5
D	2.0	1.8	2.0	11.0	3.5

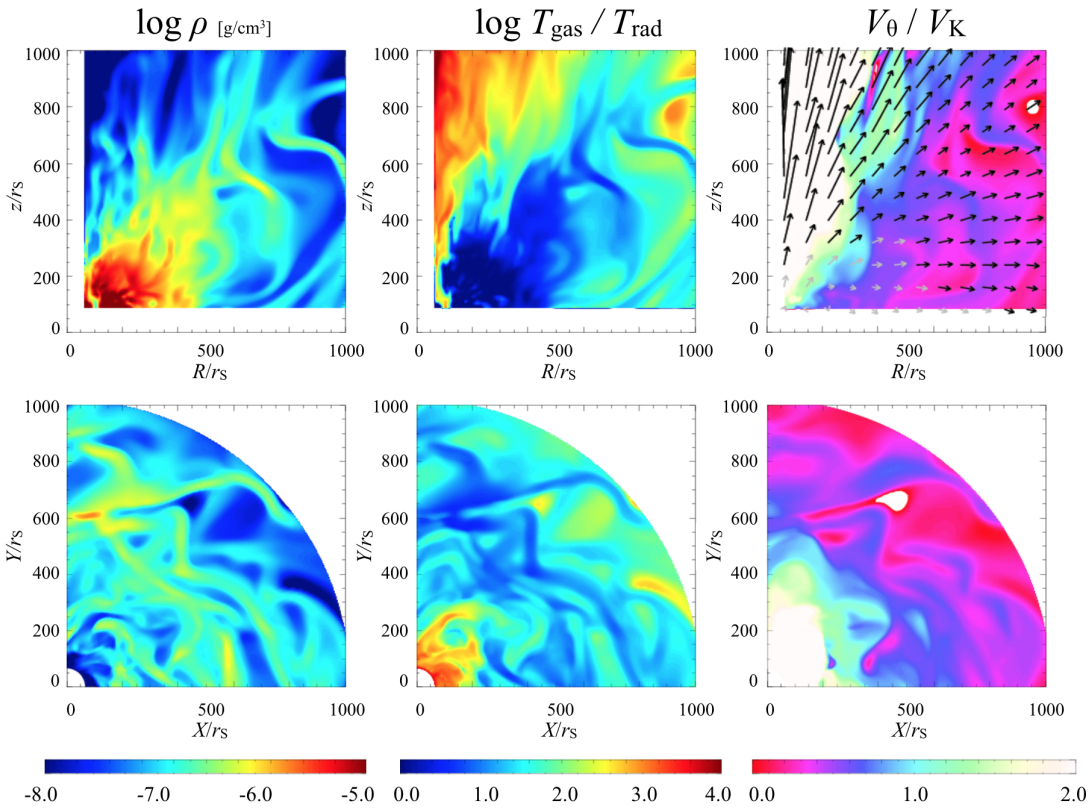

Figure 29: Same as the middle and bottom panels in Figure 13 but for model A.

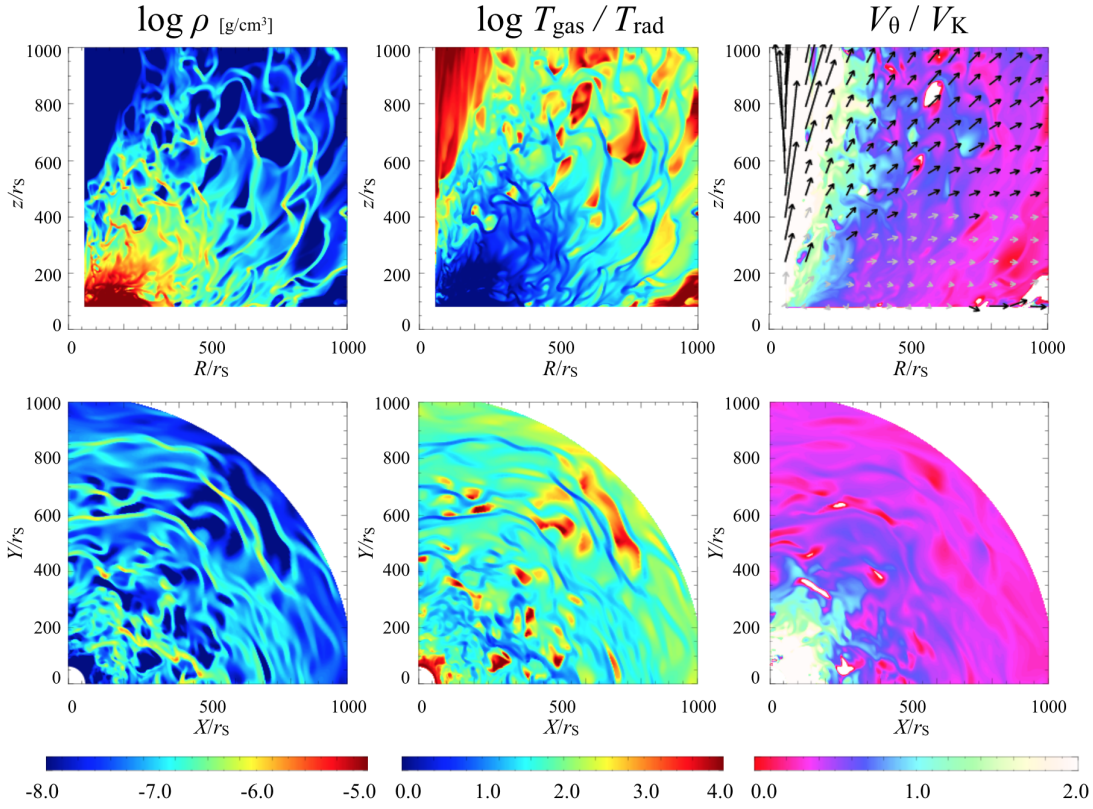

Figure 30: Same as Figure 29 but for model C.

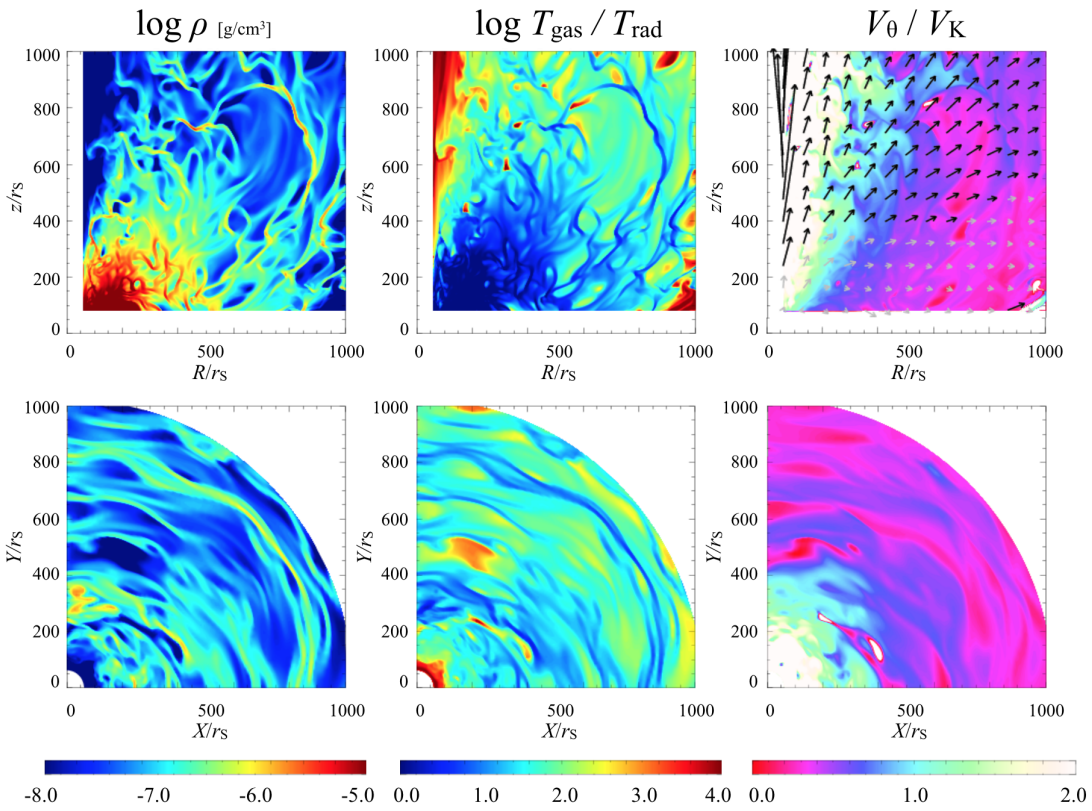

Figure 31: Same as Figure 29 but for model D.

being blown away with keeping its angular momentum. These features are consistent with the results of model B (see Figure 13). Figure 31 indicates the results for model D. Except for the clump size, the temperature ratio and the velocity fields are similar with the other models. That is, the difference according to the resolution mainly appears on the clump size.

In order to investigate the relationship between calculation resolution and the typical clump size, we calculate the ACFs in each model. As shown in the upper panel of Figure 32, the clump size clearly depends on ΔR and Δz. The higher the resolution, the smaller the typical clump size. We find $\ell_{\rm cl}^{r}/2 \sim 28\ r_{\rm S}$ for model A, $\sim 15\ r_{\rm S}$ for model B, and $\sim 10\ r_{\rm S}$ for model C. The lower panel of Figure 32 implies that the clump size in the θ-direction slightly depends on the resolution. We can see that $\ell_{\rm cl}^{\theta}$ decrease as the resolution becomes high (see models A, B, and C). Since the

clump size in the R-direction for model D is almost the same with that for model C (see upper panel), and since $\ell_{\rm cl}^{\theta}$ is larger for model D than model C (see lower panel), we can conclude that the resolution in the azimuthal direction affect only on the clump size in the θ-direction. We summarize the relationship between computational resolution and typical clump size in table 2. Higher resolution simulations are left as future work.

Finally, we investigate the time variations of the effective optical depth ($\tau_{\rm eff}$) as with the section 4.1.2. In Figure 33, we show the time evolution of $\tau_{\rm eff}$ (upper panel) and the relative variations in the effective optical depth from the average value (lower panel). In all three models, we find the effective optical depth rapidly increases at around the first 3 s and becomes quasi-steady after 3 s. The effective optical depth in quasi-steady state is around unity for all models, indicating that the location of the photosphere does not depend so much on the resolution. The lower panel means that the optical depth exhibits the small fluctuations on a timescale of several seconds. Although the timescale does not depend so much on the resolution, the amplitudes of $\Delta\tau_{\rm eff}$ is $\sim 0.2 - 0.3$ in models B and C, but $\sim 0.5 - 1.0$ in model A. Thus, the resolution of $\Delta R = \Delta z = 4.0\ r_{\rm S}$ is at least required to reveal the time variation of the apparent luminosity.

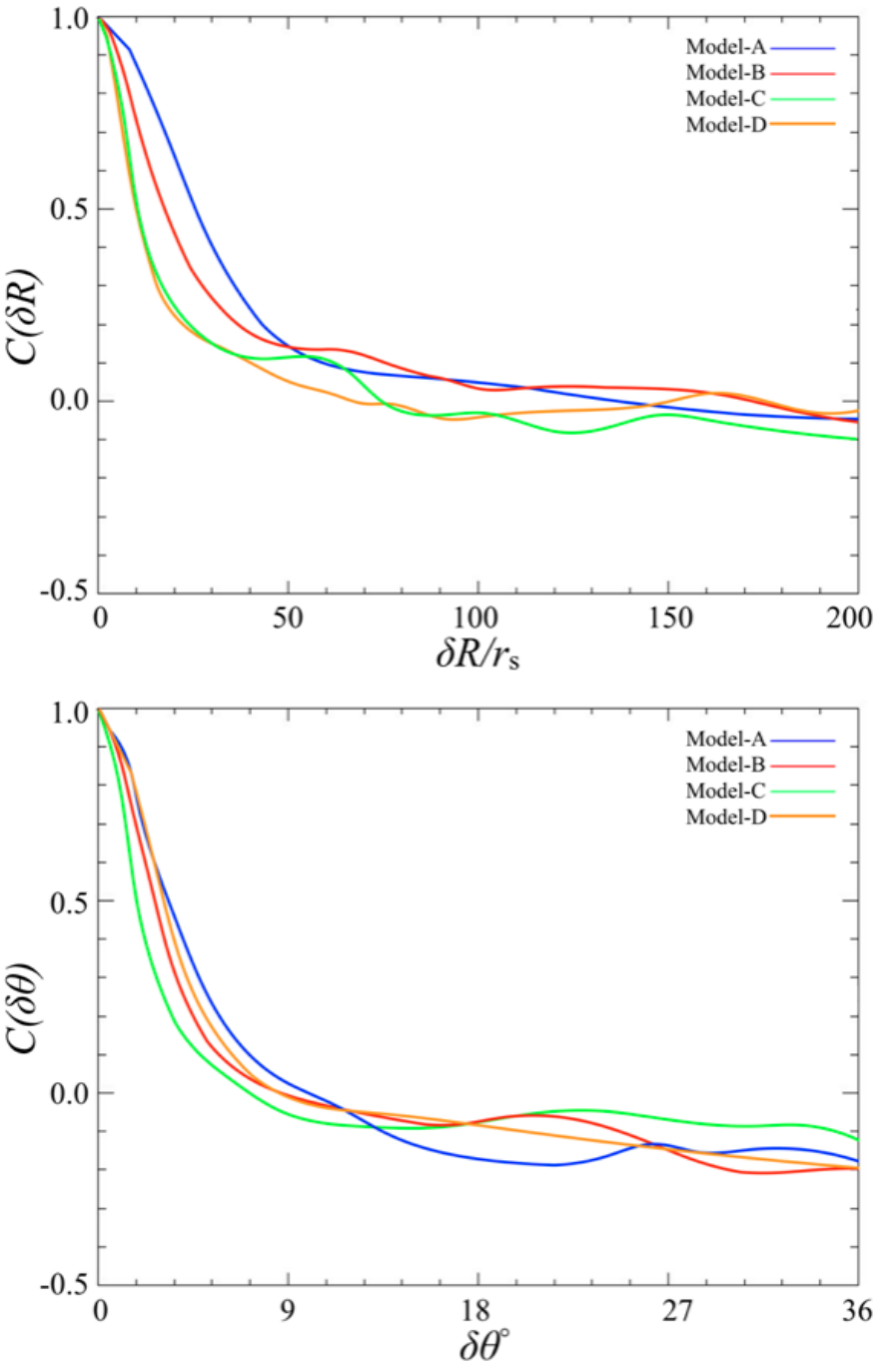

Figure 32: Azimuthally averaged ACF as a function of δR (upper panel) and horizontally averaged ACF as a function of $\delta\theta$ (lower panel) for models A (blue), B (red), C (green), and D (orange).

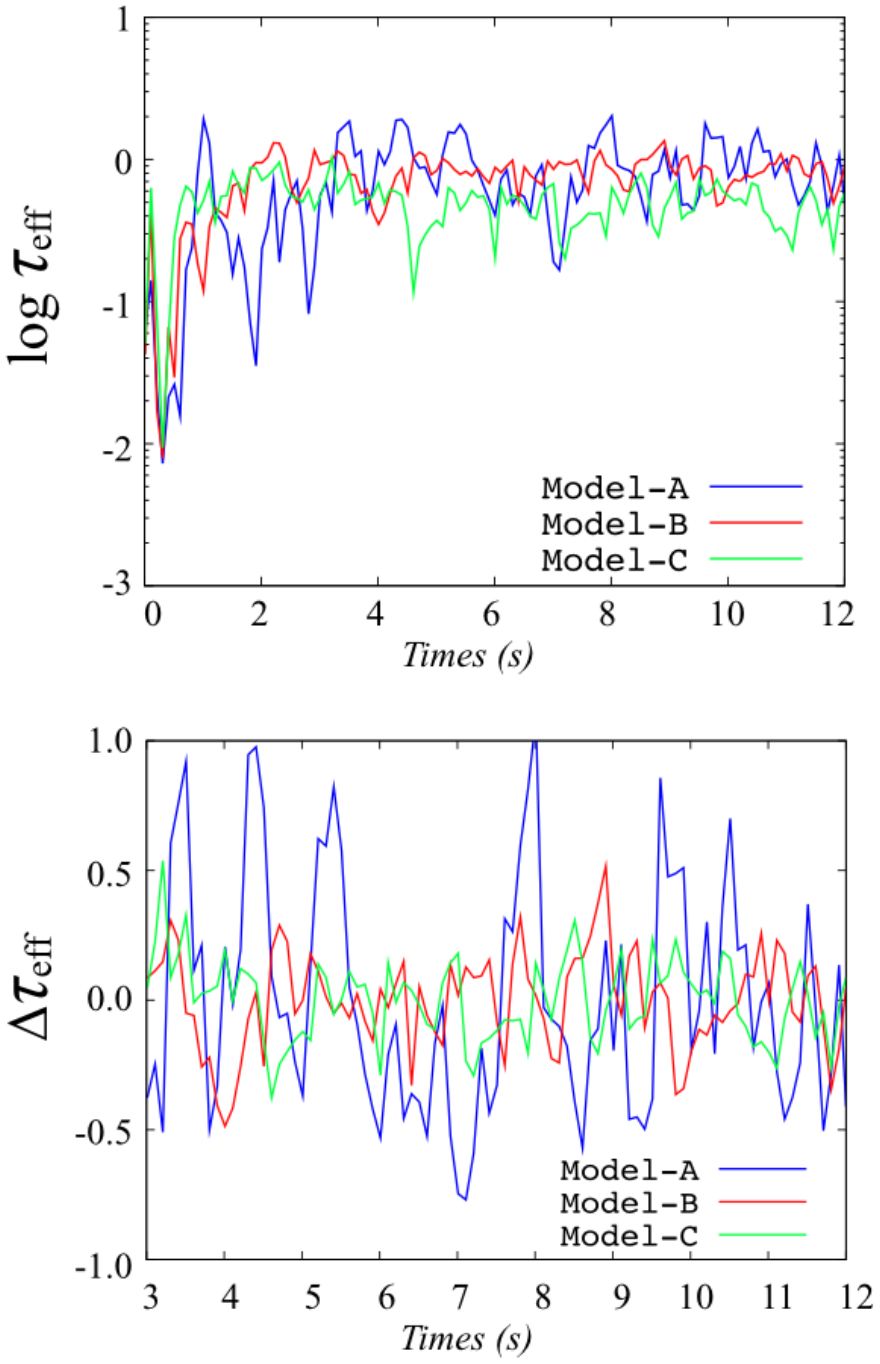

Figure 33: Time variations of the effective optical depth for the line-of-sight of $\varphi = 45°$ and $\theta = 45°$ for models A (blue), B (red), and C (green). Upper panel is the time evolution and lower panel is the relative variations from the average value.

Bibliography

[1] Abramowicz, M. A., Czerny, B., Lasota, J. -P., Szuszkiewicz, E. 1988, ApJ, 332, 646

[2] Abramowicz, M. A. 1995, ApJ, 438, 37

[3] Arons, J. 1992, ApJ, 388, 561

[4] Bachetti, M., Harrison, F. A., Walton, D. J., et al. 2014, Nature, 514, 202

[5] Bañados, E., Venemans, B. P., Mazzucchelli, C., et al. 2017, arXiv:1712.01860

[6] Colbert, E. J. M., Mushotzky, R. F. 1999, ApJ, 519, 89

[7] Collin, S., Kawaguchi, T., Peterson, B. M., Vestergaard, M. 2006, A&A, 456, 75

[8] Eggum, G. E., Coroniti, F. V., & Katz, J. I. 1988, ApJ, 330, 142

[9] Fabbiano, G. 1989, ARA&A, 27, 87

[10] Field, G. B., 1965, ApJ, 142, 531

[11] Fragile, P. C., Olejar, A., Anninos, P. 2014, ApJ, 796, 22

[12] Gladstone, J. C., Roberts, T. P., & Done, C. 2009, MNRAS, 397, 1836

[13] Gofford, J., Reeves, J. N., McLaughlin, D. E. et al. 2015, MNRAS, 451, 4169

[14] Israel G. L., Belfiore, A., Stella, L., et al., 2017, MNRAS, 466, 48

[15] Jacquet, E., Krumholz, M. R. 2011, ApJ, 730, 116

[16] Jiang, Y.-F., Stone, J. M., & Davis, S. W. 2014, ApJ, 796, 106

[17] Kallman, T. R., McCray, R. 1982, ApJ, 50, 263

[18] Kawashima, T., Ohsuga, K., Mineshige, S., Heinzeller, D., Takabe, H., & Matsumoto, R., 2009, PASJ, 61, 769

[19] Kawashima, T., Ohsuga, K., Mineshige, S., Yoshida, T., Heinzeller, D., & Matsumoto, R., 2012, ApJ, 752, 18

[20] King, A. R., Davies, M. B., Ward, M. J., Fabbiano, G. & Elvis, M., 2001, ApJ, 552L, 109

[21] Kitaki, T., Mineshige, S., Ohsuga, K., Kawashima, T. 2017, PASJ (arXiv:1709.01531) Krumholz, M. R., & Thompson, T. A. 2012, ApJ, 760, 155

[22] Long, K. S., D'Odorico, S., Charles, P. A., Dopita, M. A. 1981, ApJ, 246, 61

[23] Makishima, K., Kubota, A.,; Mizuno, T., Ohnishi, T., Tashiro, M., Aruga, Y., Asai, K., Dotani, T., Mitsuda, K., Ueda, Y., Uno, S., Yamaoka, K., Ebisawa, K., Kohmura, Y., & Okada, K. 2000, ApJ, 535, 632

[24] Manmoto, T., Mineshige, S., Kusunose, M. 1997, ApJ, 489, 791

[25] Mortlock, D. J., Warren, S. J., Venemans, B. P., Patel, M., Hewett, P. C., McMahon, R. G., Simpson, C., Theuns, T., Gonzáles-Solares, E. A., Adamson, A., Dye, S., Hambly, N. C., Hirst, P., Irwin, M. J., Kuiper, E., Lawrence, A., & Röttgering, H. J. A. 2011, Nature, 474, 616

[26] Matsumoto, Y., Asahina, Y., Kudoh, Y.,; Kawashima, T., Matsumoto, J., Takahashi, H. R., Minoshima, T.,; Zenitani, S., Miyoshi, T., & Matsumoto, R. 2016 arXiv:1611.01775

[27] McKinney, J. C., Tchekhovskoy, A., Sądowski, A., & Narayan, R. 2014, MNRAS, 441, 3177

[28] Middleton, M. J., Roberts, T. P., Done, C., & Jackson, F. E. 2011, MNRAS, 411, 644

[29] Middleton, M. J., Walton, D. J., Roberts, T. P., Heil, L. 2014, MNRAS, 438, 51

[30] Mizuno, T., Kubota, A., Makishima, K. 2001, ApJ, 554, 1282

[31] Narayan, R., & Yi, I. 1994, ApJ, 428, 13

[32] Narayan, R., Yi, I., Mahadevan, R. 1995, Nature, 374, 623

[33] Narayan, R., Sądowski, A., Soria R., 2017, MNRAS, 469, 2997

[34] Nomura, M., Ohsuga, K., Takahashi, H. R., Wada, K., Yoshida, T. 2016, PASJ, 68, 16

[35] Nomura, M., Ohsuga, K. 2017, MNRAS, 465, 2873

[36] Novikov, I. D., & Thorne, K. S. 1973, Black holes (Les astres occlus), 343-450

[37] Ohsuga, K., Mori, M., Nakamoto, T. & Mineshige, S, 2005, ApJ, 628, 368

[38] Ohsuga, K., Mineshige, S., Mori, M., Kato, Y. 2009, PASJ, 61, 7

[39] Okuda, T., & Fujita, M. 2000, PASJ, 52, L5

[40] Pavlinsky, M. N., Grebenev, S. A., Sunyaev, R. A. 1992, Soviet Astr. Lett., 18, 116

[41] Peterson, B. M. 1997, An Introduction to Active Galactic Nuclei (Cambridge: Cambridge University Press)

[42] Peterson, B. M., Ferrarese, L., Gilbert, K. M. et al. 2004, ApJ, 613, 682

[43] Pinto, C., Middleton, M. J., Fabian, A. C. 2016, Nature, 533, 64.

[44] Poutanen, J., Lipunova, G., Fabrika, S., Butkevich, A. G., Abolmasov, P. 2007, MNRAS, 377, 1187

[45] Proga, D., Stone, J. M., Kallman, T. R. 2000, ApJ, 543, 686

[46] Proga, D., Kallman, T. R. 2004, ApJ, 616, 688

[47] Sądowski, A., Narayan, R., McKinney, J. C. & Tchekhovskoy, A., 2014, MNRAS, 439, 503

[48] Shakura, N. I., & Sunyaev, R. A. 1973 A & A, 24, 337

[49] Shaviv, N. J. 2001, ApJ, 549, 1093

[50] Swartz, D. A., Soria, R., Tennant, A. F., Yukita, M. 2011, ApJ, 741, 49

[51] Takahashi, H. R., & Ohsuga, K. 2013, ApJ, 772, 127

[52] Takahashi, H. R., Ohsuga, K., Kawashima, T., & Sekiguchi, Y. 2016, Apj, 826, 23

[53] Takeuchi, S., Mineshige, S., & Ohsuga, K. 2009, PASJ, 61, 783

[54] Takeuchi, S., Ohsuga, K., Mineshige, S.,2013, PASJ, 65, 88 (T13)

[55] Takeuchi, S., Ohsuga, K., Mineshige, S., 2014, PASJ, 66, 48 (T14)

[56] Tombesi, F., Sambruna, R. M., Reeves, J. N. et al. 2010, ApJ, 719, 700

[57] Tombesi, F., Cappi, M., Reeves, J. N., Palumbo, G. G. C., Braito, V., Dadina, M. 2011, ApJ, 742, 44

[58] Tombesi, F., Cappi, M., Reeves, J. N., & Braito, V. 2012, MNRAS, 422, L1

[59] Walton, D. J., Roberts, T. P., Mateos, S., Heard, V. 2011, MNRAS, 416, 1844

[60] Walton, D. J., Middleton, M. J., Pinto, C. et al. 2016, ApJ, 826, 26

[61] Watarai, K.-y., Mizuno, T., & Mineshige, S. 2001, ApJL, 549, L77